UNIVERSITÀ DEGLI STUDI DI PADOVA

Dipartimento di Fisica e Astronomia "Galileo Galilei"

Corso di Laurea Magistrale in Fisica

Tesi di Laurea

Statistical Mechanics of Braiding

Relatore
Prof. Enzo Orlandini

Laureanda
Giada Forte

Anno Accademico 2017/2018

Contents

Chapter 1

Introduction

With the advance in single-molecule techniques, such as magnetic and optical tweezers, it's nowadays possible to reproduce the behavior of biological macromolecules subject to forces and torques.
These situations are often found in cells during natural events.
For example double stranded DNA can undergo a phase transition, reaching a supercoiled state, and its topology can be changed by type I and II topoisomerases which provoke a nick in one or both strands and transport a filament through the gate [1]. Supercoiled DNA was deeply studied experimentally [2], analytically [3] and by Monte Carlo simulations [4] in the 90's, revealing different elastic responses of the system depending on the force and on the torque injected into it (Fig. 1.1).
Magnetic tweezers also allow investigation of the work of some enzymes involved in particular processes, e.g. DNA replication [1, 5].
During DNA replication polymerases synthesize a new strand copying the base sequence from a template DNA chain. The progression of the replication can be followed by checking changes in the molecule extension: these results suggest that there is a force dependence of the replication rate and that pause sites are part of this process (Fig. 1.2).
More recently magnetic tweezers have been used for studying the formation of braids in DNA filaments [6, 7].
Braids are formed during replication between the newly synthesized molecules: type II topoisomerases have the task to resolve these links allowing the replication to continue [6] .
It's therefore interesting and biologically important to understand the topology of braids and inspect their possible phase transitions: this is the aim of this thesis where all the above cited aspects will be investigated using large scale simulations .
Before describing our approach and present our results, we will briefly summarize what is known experimentally and theoretically on braiding (Chapters 2 , 3).

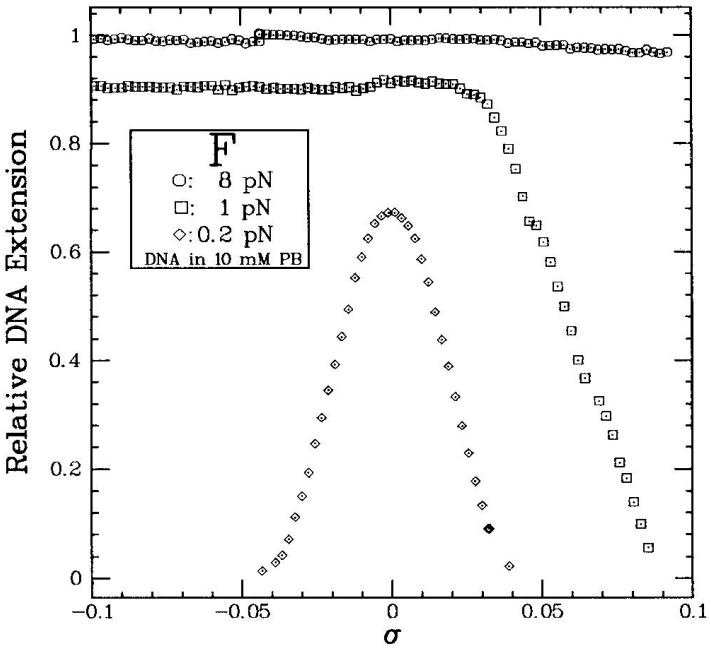

Figure 1.1: Extension versus catenation curves from Strick et al. [2]. One can observe that the system reacts differently to positive and negative supercoling depending on the force acting on it. Relative extension is given by $\frac{x}{L_0}$ where x is the chain extension and L_0 is the DNA contour length; σ is the excess linking number, or supercoiling, defined as $\sigma = \frac{Lk - Lk_0}{Lk_0}$ where Lk_0 is the linking number of a single torsionally relaxed ds-DNA and Lk is the actual link.

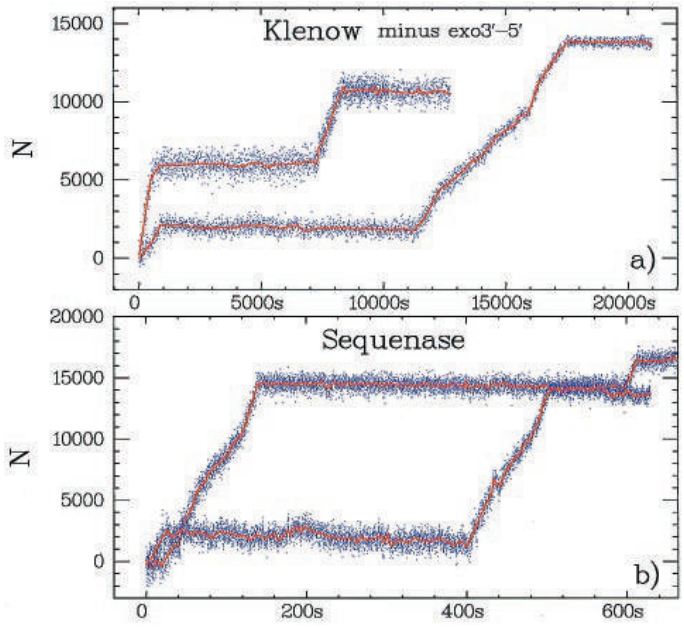

Figure 1.2: Study of the progression of the DNA replication. In each panel two examples are reported.
(a) Time evolution of the number of bases replicated by Klenow polymerase without 3' to 5' exonuclease activity under a tension of 1 pN.
(b) Time evolution of the number of bases replicated by Sequenase polymerase under a tension of 1 pN.
Figure panels (a) and (b) from Maier et al. 2000 [5].

Chapter 2

Magnetic Tweezers: an overview

Optical and magnetic tweezers allow the study of biological systems by manipulating a single molecule.
Optical tweezers were first assembled by Ashikin et al. at *Bell Labs* and in 1986 they described the first experiment in which dielectric particles were hold by a single-beam gradient force trap [8]. A glass Mie particle ($10\mu m$ in diameter) was trapped thanks to a highly focused laser beam and in the following year these tools were applied in the biological field with the aim of manipulating bacteria and viruses [9].
Later, in 1996, Strick et al. designed a new way to study single-molecule that was the basic idea of magnetic tweezers: by using a gradient of magnetic field in order to move paramagnetic beads, they were able to investigate supercoiled DNA [10].
Even if optical tweezers provide a simpler method for handling biological systems, magnetic tweezers have the advantage of allowing a multiple-beads manipulation (improving the statistics of experiments) and they don't require intense irradiation that could damage the sample [11] .
We now give a brief description of the instrumental configuration and of the various parts composing magnetic tweezers.

2.1 Experimental setup

An example of the experimental setup for a magnetic tweezers (MT) is reported in Fig. 2.1. The main features are the following:

- Flow cell: all the experiment is immersed in a glass flow cell which contains the polymer under investigation (DNA in Fig. 2.1) and a paramagnetic bead controlled by an external magnetic field. One end of the molecule is attached to the bottom of the cell, while the other one to the paramagnetic bead. If the polymer is a DNA chain, these anchorings are achieved by using a normal DNA molecule with particular handles previously prepared. Usually attachment to the surface takes place via interactions between digoxigenin labeling DNA and anti-digoxigenin which covers the surface, while attachment to the bead is allowed by interactions between streptavidin (on the bead) and biotin (forming a DNA handle) (see panel *a* of Fig. 2.2). Below the cell there is an inverted microscope which captures bead movements recorded by a computer program that has also the purpose of controlling the magnets.

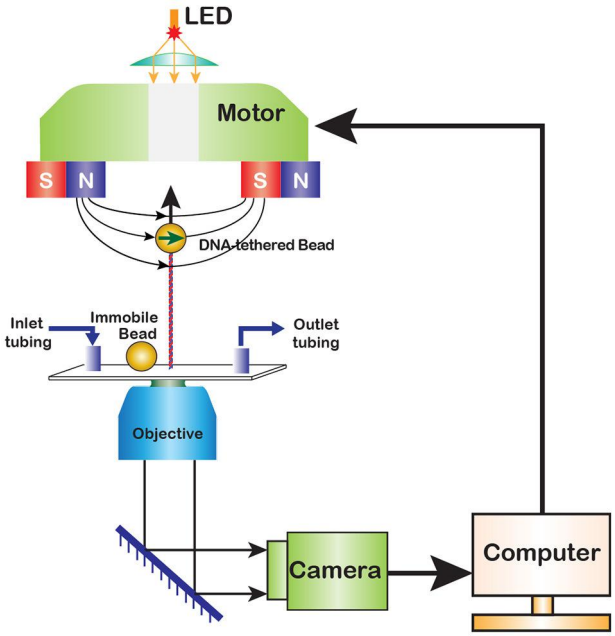

Figure 2.1: A diagram of magnetic tweezers. It's possible to observe the main components, such as magnets that create a gradient of magnetic field, the tethered bead and the objective used for tracing movements of the paramagnetic bead.
Figure from Sarkar and Rybenkov [11].

The flow cell is filled with a buffer whose composition can vary depending on the aim of the experiment: for example, if one's studying charged polymers, the salinity of the buffer plays an important role since it changes the effective charge of the polymer following the Debye-Huckel theory.

- Magnets: magnets are located above the flow cell and they move the paramagnetic bead. Variations of the intensity of the magnetic field generate a force having the same direction as the field gradient. Using a single magnet (see Fig. 2.2 c) it's possible to move vertically the paramagnetic bead pulling the molecule attached to it; instead, if one wants to introduce torque on the system, it's necessary to include a second magnet creating a configuration like the one shown in Fig. 2.2 b.
  By employing NdFeB magnets and 2.8μm bead, magnetic tweezers generate forces up to 20 pN when the distance between the magnets and the bead is of about 1 mm. Using a bigger bead or reducing the distance between the magnets and the bead, one can reach higher forces.

- Analysis of bead movements: thanks to computer analysis, movements of the paramagnetic bead can be followed. This is achieved through images of the bead collected by the inverted microscope: since the diameter of the bead is comparable to the wavelength of the incident light these images are subject to diffraction and the size of diffraction rings changes with displacements of the bead respect to the focal plane.

The vertical position of the bead is obtained through a comparison with diffraction images gathered prior to the experiment: in order to collect these reference images one has to hold the paramagnetic bead (using a strong force) and to move the objective. To avoid drift errors, a reference bead is placed on the bottom of the flow cell, stuck to the surface.

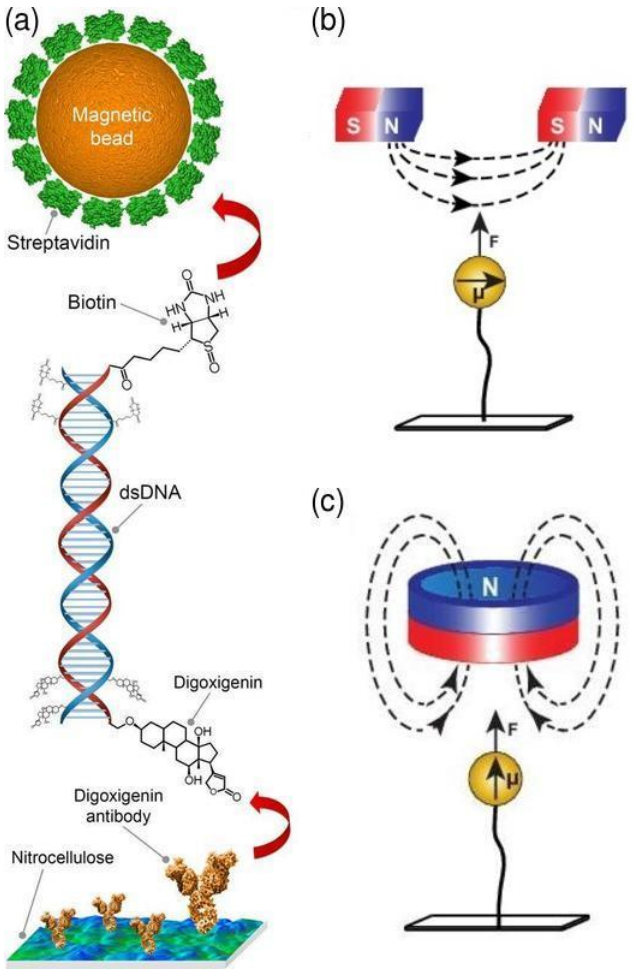

Figure 2.2: Experimental features of magnetic tweezers. **(a)** A representation of covalent bonds that allow attachments between the molecule and the bottom of the flow cell and between the molecule and the paramagnetic bead. **(b)** Horizontal arrangement of magnets used to exert torque on polymers. **(c)** Vertical arrangement of magnets useful to pull polymers without torquing them. Panel (a) from Janissen et al. [12]; panels (b) and (c) from Sarkar and Rybenkov [11] .

2.2 Applications of magnetic tweezers

Magnetic tweezers offer a practical tool allowing to inject torque on biological chains and therefore they are widely used with the purpose of studying torsional and elastic properties of polymers.
We now introduce two main types of experiments conducted with magnetic tweezers.

2.2.1 Supercoiled DNA

As mentioned in Chapter 1, supercoiled DNA was thoroughly examined in last years observing different behaviors depending on the sign of the torque exerted by magnets and on the force that pulls the chain. Fig. 1.1 shows relative ds-DNA extension versus supercoiling σ [1] in moderate ionic conditions (10 mM PB). It's interesting to note three possible responses of the system.

At low forces ($F < 0.5$ pN) the molecule reacts symmetrically both to positive and negative supercoiling. While the external magnets rotate, the DNA chain reduces abruptly its length forming plectonemic domains. An example of plectoneme is reported in figure on the side (figure from Strick et al. [13]).

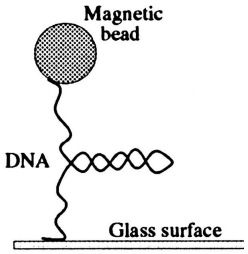

At intermediate forces ($0.5 < F < 3$ pN) overwound DNA molecules continue to create plectonemes, while underwound chains exhibit a completely different behavior [2] : for negative supercoiling, molecules seem insensitive to the rotation of the magnets, in fact their length doesn't change. This fact can be explained by considering local denaturation of double-stranded DNA: local bubbles, like the one in figure on the right (from Strick et al. [13]), form, provoking the stability of the relative extension despite the torque introduced by magnetic tweezers. In 1998 Strick et al. [13] demonstrated the formation of denaturation bubbles observing that underwound DNA was able to hybridize with a homologous single-stranded DNA.

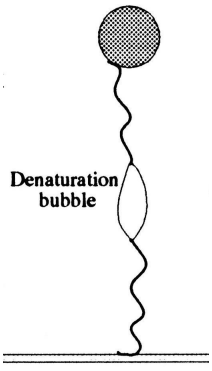

[1] We remind that supercoling σ is defined as $\sigma = \frac{Lk - Lk_0}{Lk_0}$ where Lk_0 is the link of a torsionally relaxed DNA and Lk is the actual link. The definition of link and an exhaustive explanation of the DNA topology can be found in Appendix C.

[2] An overwound DNA corresponds to a positively supercoiled molecule $\sigma > 0$, while we talk about underwound DNA if it's negatively supercoiled $\sigma < 0$.

At higher forces ($3 < F < 10$ pN) the relative extension of under- and overwound DNA molecules shows a symmetric response, even if their structures are completely different. Indeed, in underwound chains one finds denaturation bubbles, while overwound DNA changes its structure giving rise to the so called P-DNA. In figure on the side it's possible to observe differences between B-DNA (on the left) and P-DNA (on the right) (figure from Allemand et al. [14]). At high forces, positively supercoiled DNA was studied with experiments and molecular models by Allemand et al. [14], whose data suggested that this conformation is consistent with Pauling's DNA formed by interwound phosphate-sugar backbones with bases exposed outwards.

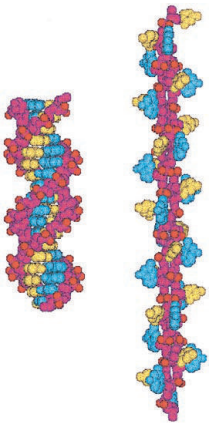

2.2.2 Braided DNA

Braids can form during DNA replication between the two synthesized molecules since the unwinding of the original DNA induces positive supercoils [15, 16, 17] .

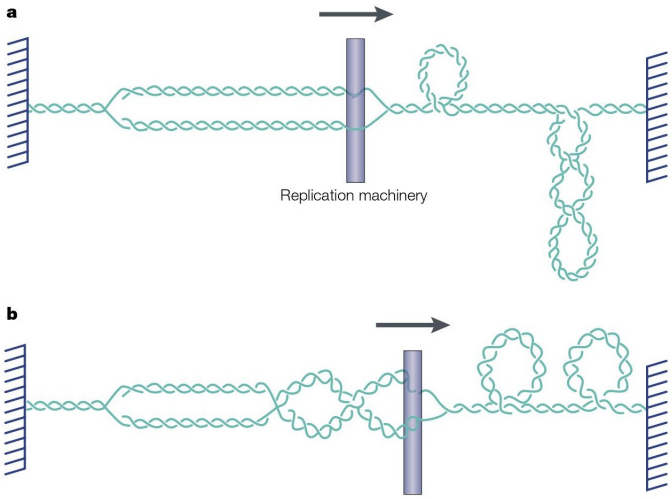

Figure 2.3: Representation of DNA replication: the anchoring points, represented as two dashed walls on both sides, can be membranes or the chromosome scaffold. **(a)** The replication machinery (that includes DNA polymerase) cannot rotate around the axis of the original ds-DNA: this causes the formation of supercoiled DNA ahead of the replication fork. **(b)** The replication machinery is allowed to rotate: in such a way the supercoiling is redistributed between braiding behind the replication fork and supercoiling ahead of it. Panels (a) and (b) from Wang [15].

In Fig. 2.3 one observes two possible scenarios that could occur during DNA replication: in the upper panel the replication machine, depicted as a grey rod, is immobile, while in the lower panel it is free to rotate around the helical axis of the template ds-DNA molecule. In the first case the linear movement of the fork unwinds the two strands of the template molecule which cannot rotate since they're attached to topological barriers. Therefore the advance of replication produces supercoils in the unreplicated DNA. In the second case the replication machine can rotate

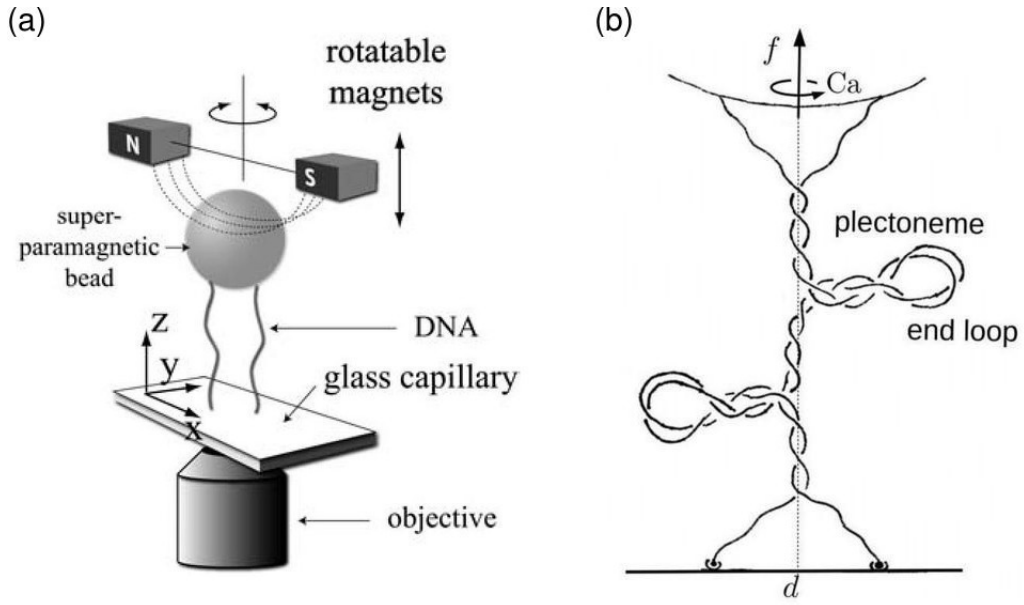

Figure 2.4: Braiding in DNA. **(a)** Diagram of experimental setup used for braiding two DNA molecules. Magnets rotate the two chains previously nicked. **(b)** Representation of braid formation: it's possible to note the presence of plectonemes. Distance d is known as *intertether distance* and f is the pulling force exerted by the magnets. The regions of the strands included between the anchoring points and the first (or the last) crossing are known as *end regions*. Panel (a) from Charvin et al. [6], panel (b) from Brahmachari et al. [20].

redistributing the torque between plectonemic domains ahead of the replication fork and a braid behind it.
Type IB and type II topoisomerases remove supercoiling or braiding: if type II topoisomerases don't resolve links between the two synthesized molecules , the replication can't continue, stopping the process of cell division [6].
First theoretical models of braiding were developed by Marko [18, 19], but even now there are only a few experimental results performed with magnetic tweezers [6, 7, 21].
Usually braiding is experimentally studied by using two nicked ds-DNA molecules: the introduction of a nick in a double-stranded DNA allows a strand to swivel about the other, so, when the magnets rotate the paramagnetic bead, the ds-DNA can relax the internal torsional stress due to hydrogen bonds. In this way a braid between two DNAs can be compared to a braid between two single strands (with appropriate interactions) as in Fig. 2.4.

As in supercoiling, plectonemic transition is observed in braiding too: exceeded a critical catenation (i.e. half of the number of crossings between the two strands) the braid starts to form plectonemic domains and the transition is highlighted by a change in the curve slope in the *Extension versus Catenation* graphic [3]. An example is reported in Fig. 2.5, where along the ordinate there is extension (or end to end distance of strands) and along the abscissa there's the number of turns n of the magnets, that is a measure of catenation.

[3]With terms *extension* or *end-to-end distance* we indicate the extension of the braid along its axis, while the meaning of *catenation* can be found in Appendix C.

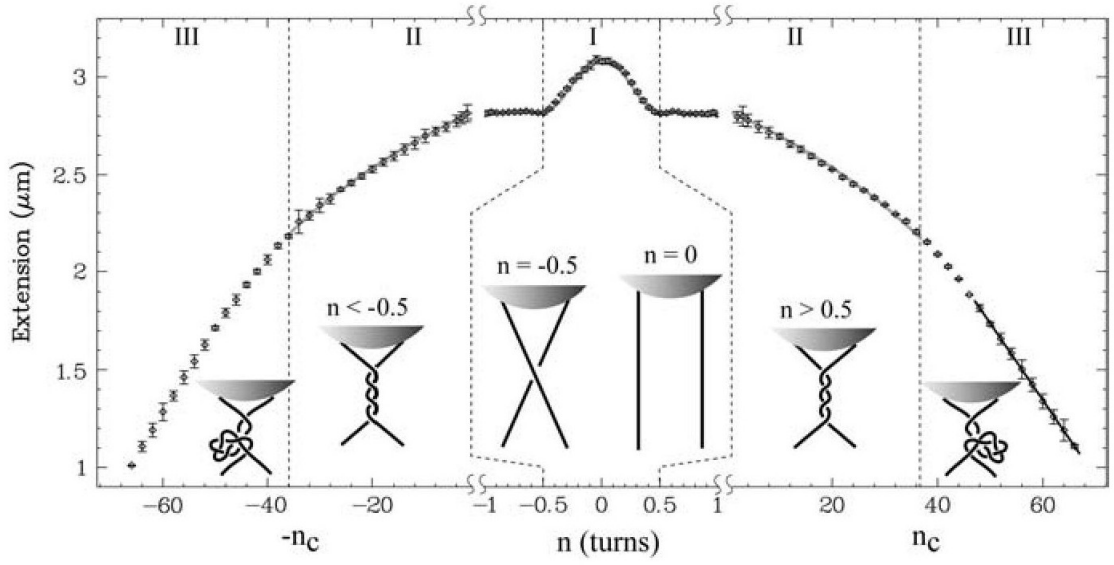

Figure 2.5: Extension versus catenation for d= 0.36 L. The catenation can be calculated as the number of turns of magnets, because every turn of the paramagnetic bead entails a crossing between the two strands. It's possible to distinguish the three regimes mentioned in the text: the abrupt decrease due to the first half turn ($0 <| n |< 0.5$), the braid formation ($0.5 <| n |< n_c$) and the plectonemic nucleation ($n \geq n_c$). Open diamonds are experimental data obtained with a pulling force $f = 2$ pN in 100 mM PB, while the curve in region III is a linear fit to the data. Finally in regions I and II there's a fit to the geometrical model developed by Charvin et al.. Figure from Charvin et al. [6].

Here three different regimes can be observed:

1. $0 <| n |< 0.5$: a sudden decrease is introduced by the first half turn. These experimental data are referred to the case where the relation between the intertether distance d (see Fig. 2.4) and the strands length L is d=0.36 L. Such a distance provokes a remarkable reduction in the extension when the first crossing forms (n=0.5);

2. $0.5 <| n |< n_c$: in regions II a strand wraps around the other creating a straight braid;

3. $| n |> n_c$: after a critical value n_c, the helically wrapped region undergoes a phase transition (*buckling transition*). An abrupt change in the curve slope is observed and this is due to plectonemes formation.

These experiments have allowed to study braiding in DNA and in the next chapter we will review the main results obtained so far on this issue.

Chapter 3

Braiding DNA: state of the art

The response curves commonly used to study braiding are those that represent *Extension versus Catenation*, like the one in Fig. 2.5 : it's interesting to see how these curves change with intertether distance d, pulling force f and ionic concentration of the buffer in the flow cell [1].
Such features were analyzed in depth by Brahamachari et al. by developing a statistical-mechanical model [20] and then testing their theoretical results with experiments [7]: in this model the total free energy of a braid is divided into the three terms $\beta\mathcal{E}_s$, $\beta\mathcal{E}_p$ and $\beta\Delta\mathcal{F}$.
The first term $\beta\mathcal{E}_s$ is the free-energy of the straight braid: it involves different contributions due to the elastic bending energy of the helix, to the force-extension energy and to the electrostatic potential calculated through the Debye-Huckel theory.
The second term $\beta\mathcal{E}_p$ is the contribution given by the plectoneme region and it depends on the bending and electrostatic energies of the braid forming plectonemes, on the bending and electrostatic energies of the superhelical structure of the braid within plectonemic domains and on the total elastic energy. It contains also a contribution related to the entropy of a buckled braid with m end-loops, whose origin is due to two main factors: the possible diffusion of a plectoneme along the braid (plectonemes can develop in different nucleation sites) and the exchange of DNA among plectonemes (the total length of the buckled state remains constant, but length of a single plectoneme can change).
Finally the last term $\beta\Delta\mathcal{F}$ represents the total free energy due to worm-like-chain fluctuations.
So the total free energy of a braid with a plectonemic length L_p and m end-loops is obtained by minimizing the following free-energy over the catenation of the straight phase Ca_s:

$$F(L_p, m) = \min_{Ca_s}(\mathcal{E}_s + \mathcal{E}_p + \Delta\mathcal{F}).$$

By summing over all configurations, one can write the partition function:

$$\mathcal{Z}(Ca, f) = e^{-\beta F(0,0)} + \sum_{m=1,2..} \sum_{L_p} e^{-\beta F(L_p,m)}$$

[1] DNA is a polyelectrolyte whose negative charge is due to the presence of phosphate groups; therefore the salt concentration of the solution where it is immersed in can influences its behavior.

where Ca is the total catenation divided between the straight phase (Ca_s) and the buckled (plectonemic) phase (Ca_p), i.e. $Ca = Ca_s + Ca_p$, and f is the applied force. The partition function allows to calculate equilibrium values of physical quantities such as the average end-to-end extension of the braid $< z/L >$ (where L is the contour length of each DNA strand), the torque in the system $< \tau >$ and the mean number of plectonemes $< m >$.
As we said at the beginning of this chapter, the behavior of the braid changes with the value of the pulling force, as shown in Fig. 3.1 : in this figure, along the abscissa, there is catenation density defined as $\sigma_c \equiv Ca/Lk_0$ ($Lk_0 = L/h$ where $h = 3.6nm$ is the pitch of a double-helix DNA).

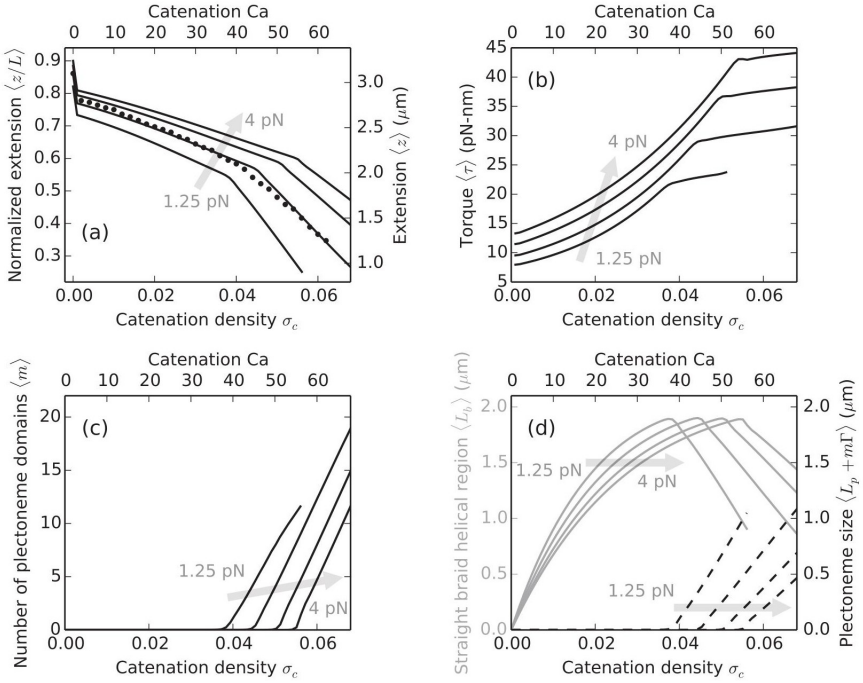

Figure 3.1: Braid behavior when force changes between 1.25 pN and 4 pN; theoretical curves are related to DNA chains of $\approx 11kbp$ ($L = 3.6\mu m$) with an intertether distance of $1.5\mu m$ ($d = 0.42L$). **(a)** Normalized end-to-end distance over catenation density. The buckling transition occurs at higher catenations for larger forces: the change the in curve slope is due to plectoneme nucleation. Solid circles are experimental data (for 2 pN at 100 mM univalent salt concentration) obtained by Charvin et al. [6]. **(b)** Torque in the braid over catenation density. It's interesting to note how torque doesn't increase linearly before the buckling point; instead, after the transition, it increases with a small slope thanks to the internal torsional relaxation provoked by plectonemic nucleation. **(c)** Number of plectonemic domains over catenation density. Beyond the buckling point, plectonemes start to nucleate: their number increases with decreasing force. **(d)** Length of the straight braid region $< L_b >$ (solid grey line) and length of the plectonemic region $< L_p + m\Gamma >$ (dashed black line) as a function of catenation density; m is the number of plectonemes, while Γ is the size of plectoneme end-loop. Obviously, after the transition, $< L_b >$ decreases abruptly, while the size of the plectoneme region starts to rise. Figure from Brahamachari et al. [20].

In panel (a) of Fig. 3.1 one can notice an initial abrupt drop due to the formation of the first half catenation: since the intertether distance is enough large ($d = 0.42L$), there is a noticeable reduction in the end-to-end distance when the two strands form the first crossing. After that, the extension is subject to a slow decrease: at this stage the helically wrapped region is formed, resulting in a straight braid. Finally we find the buckling point: in panel (a) of Fig. 3.1 it is identified as a *knee* in the curve and, in panel (c), we can observe that, at this critical catenation, nucleation of plectonemes appears.
After the transition the internal torsional stress is released and the plectoneme nucleation becomes energetically favorable: this is apparent in panel (b) where, beyond the buckling point, the torque in the braid increases slower thanks to the writhe contribution. It's interesting to note a deep difference between braiding and supercoiling: in supercoiling, before buckiling, the torque increases linearly, while here a non-linear response is observed. The origin of this difference is the lack of chemical bonds between the two strands forming the braid: in fact, in double-helix DNA, hydrogen bonds provide a constant twist stiffness to the structure, while in a braid the twist modulus depends on the catenation [7] .
It's also possible to distinguish effects due to the application of different forces: higher forces shift the buckling transition to larger values of Ca.
After the buckling, the number of plectonemic domains grows with Ca, as show in panel (c) of Fig. 3.1. Brahamachari et al. highlight another difference between supercoiling and braiding: supercoiling favors the nucleation of a single long plectoneme, while in braiding many short plectonemes appear beyond the transition point [7]. As they explain, this different behavior is due to two factors:

- electrostatic repulsions are more effective in braids (a braid has a charge that is twice of the one of a ds-DNA), so these interactions implicate a greater excluded volume which destabilizes the superhelical structure;

- braids are bulky structures with a larger bending stiffness respect to a double-helix DNA.

The intertether distance d plays an important role too, as can be noticed in Fig. 3.2. It's interesting to see how, keeping a fixed σ_c, the twist modulus grows with increasing intertether distances (panel (b)): this implies that the buckling transition occurs for lower catenations when d is larger.
As already mentioned, the initial abrupt decrease in the end-to-end distance takes place after the first half catenation: by looking at the panel (a), it's clear that when $d = 0.5L$ the extension reduction is more pronounced than when $d = 0.1L$. However, it can be calculated by simply using the Pythagorean theorem [21].

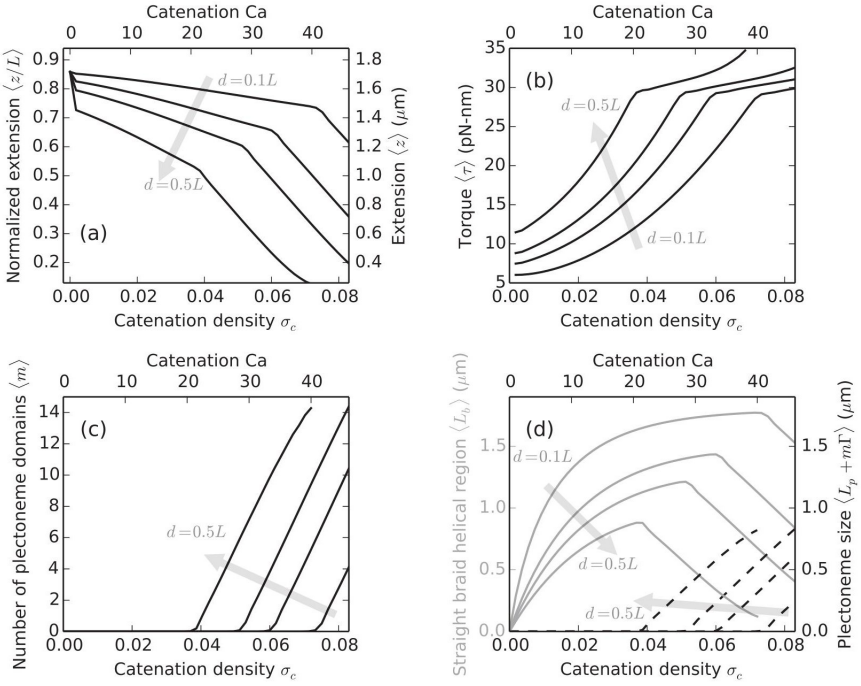

Figure 3.2: Braid behavior when intertheter distance is $d = 0.1L, 0.25L, 0.35L$ and $0.5L$. Data are referred to braids with length of $L = 2\mu m$ under $2pN$ force at $100mM$ salt. **(a)** Normalized extension over catenation density: a smaller intertether distance provokes a delay in the buckling transition. **(b)** Torque in the braid over catenation density. Torque is a thermodynamic property of the system and it doesn't depend on the distance d between the anchoring points: this means that the value of the critical torque doesn't change with d. **(c)** Number of plectoneme domains over catenation density: multiple domains form after the transition. **(d)** Length of the straight braid region $< L_b >$ (solid grey line) and length of the plectoneme region $< L_p + m\Gamma >$ (dashed black line) as a function of catenation density: one observes that the buckling value of L_b is smaller for greater distances since end-regions of the two strands (where there isn't the braid formation) have a larger size. Figure from Brahamachari et al. [20].

Finally, considering DNA as a charged polymer, also ionic conditions can influence the phase transition and so, in Fig. 3.3, it's represented the behavior of a braid surrounded by a buffer with various salt concentrations included between $0.1\,mM$ and $0.5\,mM$.
Lowering salt molarity induces a greater Debye length with a consequent growth of the excluded volume: the effective diameter increases, the straight phase becomes more instable and so the buckling transition occurs for lower catenation values (panel (a) of Fig. 3.3). At the same time, an higher ionic concentration stabilizes superhelical structures: as a consequence, the number of plectoneme domains decreases with the increasing molarity, as shown in panel (c).
As in Fig. 3.2 , also in panel (b) of Fig. 3.3 it's possible to observe the thermodynamic nature of the critical buckling torque, which therefore doesn't change according to ionic concentrations.

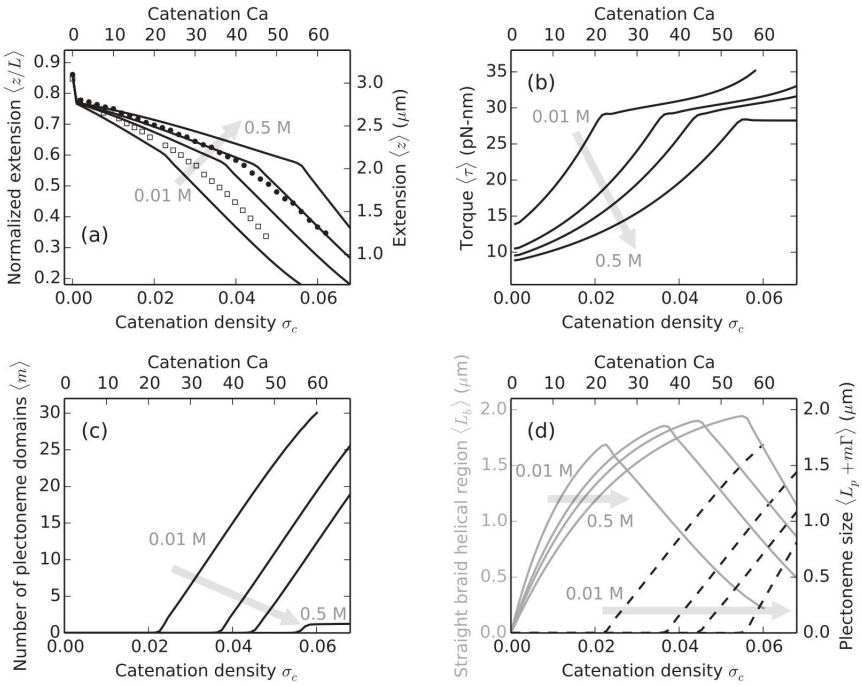

Figure 3.3: Effects of ionic concentration on DNA chains of 3.6 in length under $2pN$ force and divided by an intertether distance equal to $d = 0.42L$. Curves are referred to 0.01, 0.05, 0.1 and 0.5 M salt concentration. **(a)** Normalized extension over catenation density: an high ionic concentration stabilizes the straight braid delaying the buckling transition. Open squares and solid circles are experimental data obtained for 0.01 M and 0.1 M by Charvin et al. [6]. **(b)** Torque in the braid over catenation density: torque doesn't depend on salt concentration, so its critical value remains the same for different molarities. **(c)** Number of plectoneme domains over catenation density: an higher salt concentration provokes a reduction in the electrostatic repulsion, resulting in the nucleation of few domains. **(d)** Length of the straight braid region $< L_b >$ (solid grey line) and length the of plectoneme region $< L_p + m\Gamma >$ (dashed black line) as a function of catenation density: $< L_b >$ increases faster for lower concentrations, since the excluded volume is greater. Figure from Brahamachari et al. [20].

The last important graphic giving us informations about the buckling transition is shown in Fig. 3.4 and it was obtained by Charvin et al.[6]. The authors used Monte Carlo simulations to model DNA braiding, including various energy terms, such as the bending energy of a chain configuration, an energy term related to the pulling force and other three terms with the purpose of keeping the positions of the anchoring points.
The underlying force versus catenation equilibrium phase diagram shows the behavior of the buckling transition when the intertether distance is such that $d << L$. In the y axis we find a dimensionless variable depending on the pulling force, while in the x one it is reported the critical catenation density, namely the value of the catenation density at which the $(\sigma_c, < z/L >)$ graphic changes its slope revealing the buckling transition. Therefore above the transition line one observes unbuckled systems, while below we see buckled braids, in which, according to the model of Brahamachari et al., plectonemic domains nucleate.

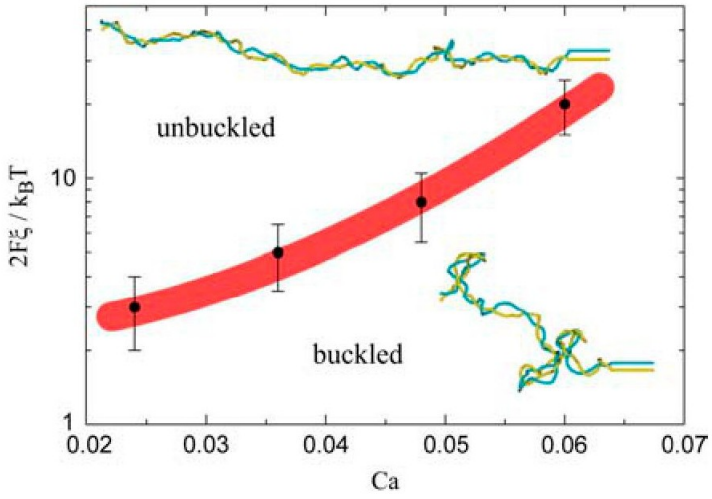

Figure 3.4: Force versus critical catenation density (Ca) when $d/L \ll 1$; this phase diagram is obtained with Monte Carlo simulations. Along the y axis there's a dimensionless variable $2F\xi/k_bT$ where ξ is the persistence length of a single DNA and T the temperature of the system; instead along the abscissa we find the critical catenation density at which the buckling transition occurs. Figure from Charvin et al. [6] .

Chapter 4

Our model of braiding and simulation methods

In our study braiding of two chains is simulated by using the LAMMPS software: different elements compose the simulations setup, in such a way that we can work on a coarse-grained model that mimics, at a given scale, the experimental setups.

4.1 Coarse-grained model of strands

Each strand is described by a chain of N beads. Lennard-Jones units are used (see Appendix B), therefore lengths are expressed in term of σ and as reference length we take the DNA diameter which depends on the ionic conditions of the buffer surrounding the chain.
An example of our setup is reported in Fig. 4.1.

As can be seen, a ds-DNA molecule is given by a sequence of beads bonded together and we can distinguish between two main types of interactions:

- two body interactions;

- three body interactions.

Two body interactions embrace pair potentials both between bonded and unbonded atoms.
Unbonded beads interact via the Lennard-Jones (LJ) 6-12 potential 4.1 [1] :

$$E = 4\epsilon \left[\left(\frac{\sigma}{r - \Delta} \right)^{12} - \left(\frac{\sigma}{r - \Delta} \right)^{6} \right] \tag{4.1}$$

This form of the LJ potential includes a variable Δ that allows us to work with beads of different sizes. This can seem worthless since atoms forming the strands have the same dimensions, but we'll see that various diameters will be necessary in order to simulate experimental magnetic tweezers.

[1] In our runs this potential is cutoff at $\sqrt[6]{2}\sigma + \Delta$.

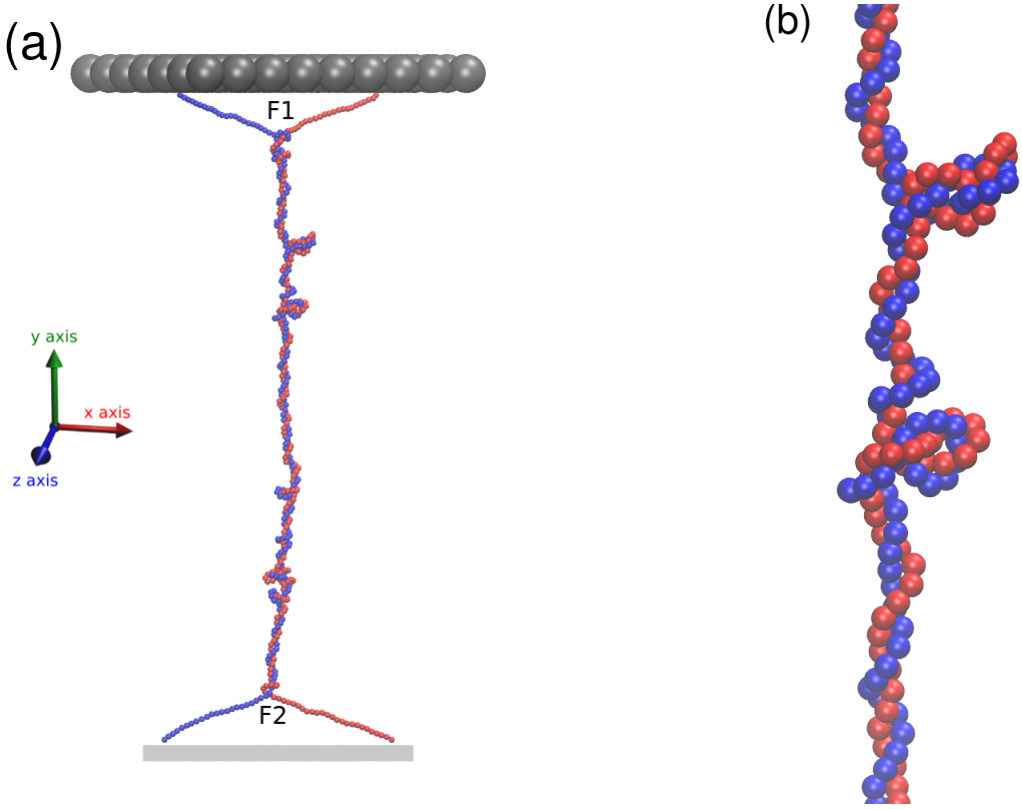

Figure 4.1: Example of the setup. **(a)** The entire setup where it's possible to distinguish between the different elements composing our model. The point *F1* indicates the upper fork where the two strands start to form the braid; on the other hand *F2* corresponds to the lower fork. **(b)** A detail of the braid: one can notice that in this configuration the braid has yet undergone the phase transition giving rise to plectonemes.

Instead, bonded beads interact via a potential given by 4.2:

$$E = -\frac{1}{2}KR_0^2 ln\left[1-\left(\frac{r}{R_0}\right)^2\right] + 4\epsilon\left[\left(\frac{\sigma}{r}\right)^{12} - \left(\frac{\sigma}{r}\right)^{6}\right] + \epsilon \tag{4.2}$$

The first term corresponds to a finitely extensible nonlinear elastic (FENE) potential, whose extended expression is the following:

$$E = \begin{cases} -0.5KR_0^2\, ln\left[1-\left(\frac{r}{R_0}\right)^2\right] & if \quad r < R_0 \\ \infty & if \quad r > R_0 \end{cases}$$

It is often used for bead-spring polymer models: it reduces to an harmonic potential for little r values, while it diverges for large extensions, causing the finite extensibility of the polymer. The value of R_0 stands for the maximum extension of the bond, while K is related to its strength. In our simulations we use to set $R_0 = 1.5$ and $K = 30$, both expressed in LJ units.
The last two terms of Eq. 4.2 represent a shifted Lennard-Jones potential: in simulations it is cutoff at $\sqrt[6]{2}\sigma$, so it describes interactions between rigid spheres.

The potential 4.2 is reported in Fig. 4.2, where the values of coefficients R_0 and K are set as just said and furthermore σ and ϵ are equal to 1.

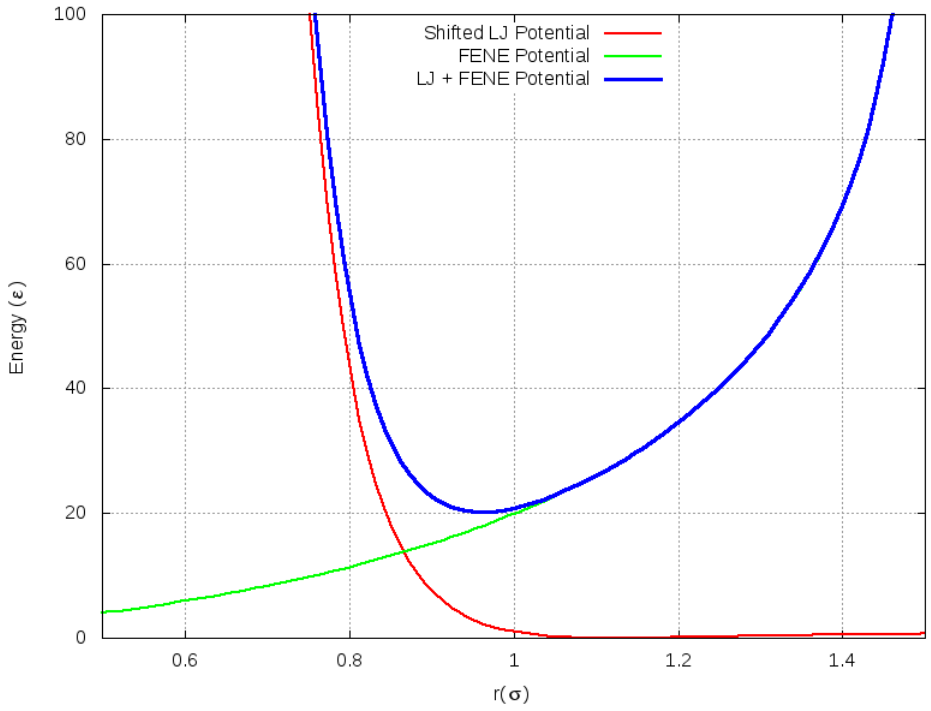

Figure 4.2: Fene and shifted Lennard Jones potentials used for bonded beads. The blue line shows the sum between these two terms.

Three body interactions emerge between three bonded beads forming an angle θ. This potential has the following form:

$$E = K[1 + cos\theta] \tag{4.3}$$

Using a worm-like-chain model, one observes that K is proportional to the persistence length of the polymer, so, depending on what we want to simulate, we can use different values for it: usually we deal with a persistence length of 50 nm, therefore $K = \frac{50}{\sigma}$.

For polyelectrolytes as DNA, one should also consider the energy contribution due to the charges of the molecule and the ions of the solution where the polymer is immersed in. This can be done in an approximate way by using a Deby-Huckel interaction

$$\Psi(r) = \frac{z_j e}{4\pi\epsilon_r\epsilon_0}\frac{e^{-kr}}{r} \tag{4.4}$$

where z_j is the charge of the ion we're considering, ϵ_r is the relative permittivity of the medium and k is the reciprocal of the Debye length λ_D.
By lowering salt concentration, the Debye length grows and so the electrical repulsion is more effective causing an increase in the braid diameter. Normally we'll consider a DNA molecule 2.5 nm in diameter, which will be equal to the braid radius: this value of the braid radius corresponds to an high salt concentration of about 0.5 M ($\lambda_D \simeq 0.4$ nm) and, consequently, the electrical interaction can be ignored [20].

4.2 Simulating the experimental setup

Experimental magnetic tweezers, which rotate and pull DNA chains, are represented by several beads forming a wall. The number and the size of beads depend on the distance between the DNA strands: with bigger distances bigger beads are used in order to create a wall with a little number of atoms reducing simulation time.
The x-y-z axes are oriented as in Fig. 4.1. The central bead is pulled by a constant force: since the wall is a rigid body, this force has the effect to move the entire wall and the upper beads of the strands joined with it. In such a way one can pull polymers simulating the action of magnetic tweezers.
Magnetic tweezers can rotate the strands too, so in our simulations rotations are obtained by imposing a torque to the rigid body formed by the wall and the upper beads of the chains.
The interactions between the beads of the wall can be neglected: the wall has only the purpose of moving the chains, so it's also possible to exclude these interactions during runs improving their speed.
Interactions between the wall and the strands are instead crucial: these would forbid the strands to overcome the wall, which could give rise to unphysical situations. Therefore potential 4.1 is used: σ and ϵ are equal to 1, while Δ takes on value $\sqrt[6]{2}\sigma(R-r)$ where R is the radius of the beads of the wall and r the one of the beads of the chains [2].

4.3 Dynamics

In our stochastic simulations, the chain beads follow Brownian dynamics, where the position vector of the i-esim bead, $\vec{r}_i$, respects the Langevin equation 4.5

$$m\frac{d^2\vec{r}_i}{dt^2} = -\lambda\frac{d\vec{r}_i}{dt} + \vec{\eta}(t). \tag{4.5}$$

The first term on the right is a viscous force and it's proportional to particle velocity, while the second one is the stochastic part of the motion due to collisions between DNA bases and particles of the buffer.

The beads forming the bottom part of the strands are held in fixed position: they are also in contact with a region that stands for the surface of the experimental flow cell. This region, represented in Fig. 4.1 as a grey wall, interacts with the strands through the harmonic potential

$$E = \epsilon(r - r_c)^2 \tag{4.6}$$

where ϵ plays the role of a spring constant and r_c is the cutoff distance.
In order to maintain distances between the region and the strands, we use $\epsilon = 200$ and $r_c = 1$ expressed in Lennard-Jones units.
Another force to be taken into account is the one imposed on the central bead of the upper wall that causes the stretching of the braid along the y-axis (normally this is kept constant during an experiment).

[2] In our simulations the beads of the chains are 1σ in diameter, so $r = \sigma/2$.

The last term that could be included in the dynamics is a constant torque applied on the upper wall. So we recognize two possible setups:

- varying catenation setup: the upper wall is moved by a torque directed along the y-axis provoking a change in the catenation between the two strands;

- fixed catenation setup: the wall is fixed and the two strands were prepared with a given catenation. The system is then allowed to relax with a constant pulling force acting on it.

We now give a more detailed description of these two setups.

4.3.1 *Varying catenation* setup

In order to study the buckling transition and find the equilibrium phase diagram (Ca_c, F) [3], we need to work at constant catenation. To obtain these configurations we add a torque to the upper wall: the torque rotates the wall in the x-z plane, so it's directed along the y-axis. Such a dynamics let the braid formation, since the strands, initially straight and parallel, can wrap around each another. At this stage we use a strong pulling force, so we can reach high values of Ca without causing the formation of plectonemes.
For a given simulation the value of the torque is fixed and it's chosen so that it can provide the greatest number possible of initial configurations with different catenations .

4.3.2 *Fixed catenation* setup

The configurations with a fixed Ca are then used as initial conditions for the equilibrium simulations: in this case the upper wall cannot rotate any more, so we simply allow the system to relax while the pulling force is kept constant. Generally its value is lower than the one used in the first setup, but this choice doesn't influence the evolution of the system: since we aim to reach the equilibrium, the result wouldn't have changed if the force in the first setup had been lower than the force in the second one.

[3] Ca_c indicates the critical catenation where the buckling transition starts, while F is the pulling force.

Chapter 5

Statics of the buckling transition

In this chapter we'll analyze the buckling transition in a braid formed by two strands.
Since we know from previous studies that the intertether distance d affects the buckling transition, we're going to study it for three values of d.
We choose to use two strands composed by 250 beads 1σ in diameter (see Appendix B) and, once fixed the catenation Ca, we apply different forces F to the upper wall: for higher forces we expect that the transition occurs at larger values of Ca. Since $\sigma = 2.5$ nm, our chains have a contour length of 625 nm.
By imposing $L_0 = 250\,\sigma$, we analyze the following cases:

	d(σ)	d/L_0
1	6	0.024
2	42	0.168
3	120	0.48

For each one of the three cases we inspect different catenations obtained from the *varying catenation* setup. As d decreases, we need to handle larger values of Ca in order to observe the formation of plectonemes.

5.1 Intertether distance d=0.024L_0

We start with the case in which the two strands are very close to each another ($d = 0.024\,L_0$): this ratio between d and L_0 was studied by MC simulations in [6]. An example of our setup is shown in Fig. 5.1

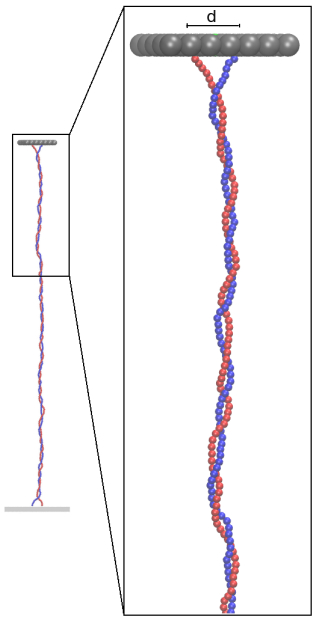

Figure 5.1: Example of the setup employed for the case $d = 0.024\,L_0$ when $Ca = 19$ and $F = 13.3$ pN. The right panel is a zoom to highlight the braided phase.

We now report the forces used for studying the buckling transition:

Force (pN)		
10.0	11.6	13.3
14.9	16.6	18.3
19.9	21.6	23.2

Table 5.1: Values of the forces used in the setup $d = 0.024L_0$

For each catenation and force, we allow the system to relax: in order to reach equilibrium, note that at high Ca one has to wait longer because the braid has to form plectonemes. To decide whether the system has reached equilibrium we look at the time behavior of the extension *Ext* (i.e. the end-to-end distance) of the braid. Below we show two graphics reporting *Extension versus Time*.

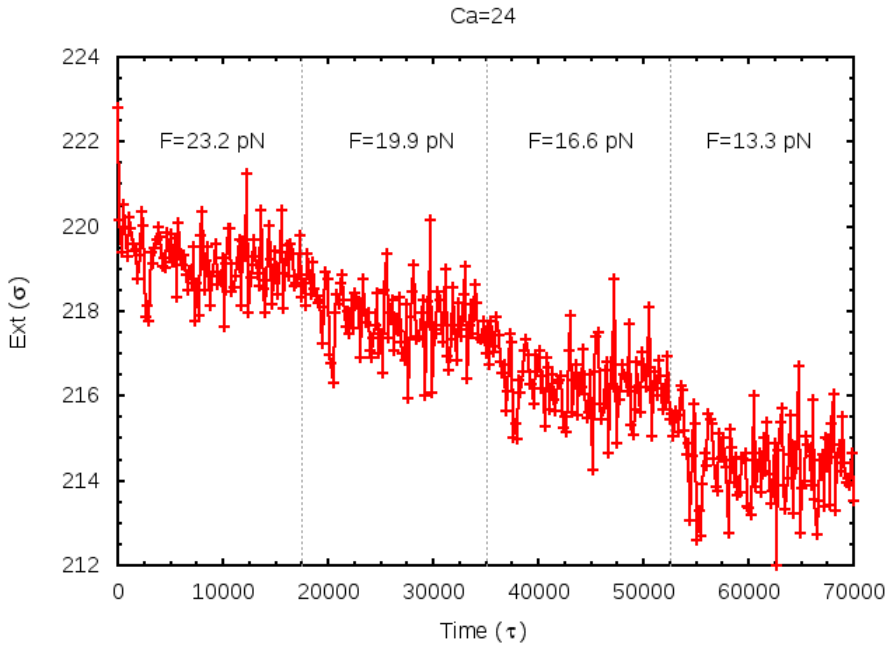

Figure 5.2: Extension versus time at Ca=24 with the force F varying from 23.2 pN to 13.3 pN. In the two axis we use Lennard-Jones units (see Appendix B).

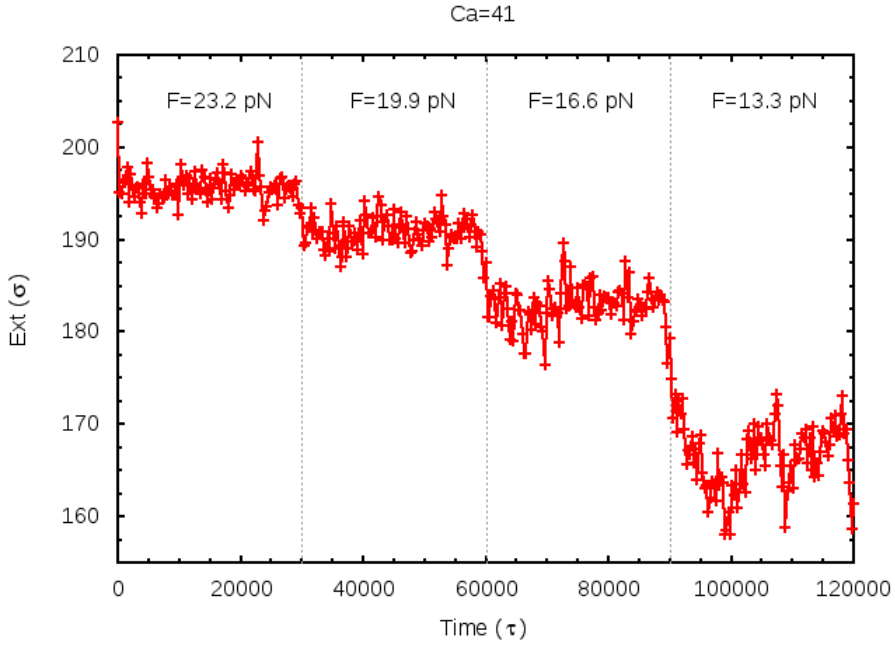

Figure 5.3: Extension versus time at Ca=41 with F varying from 23.2 pN to 13.3 pN.

Note that the system reaches the equilibrium for every considered force. As the force varies, the values of the braid extension are similar for $Ca = 24$, while there are greater gaps when $Ca = 41$: this is a signal of the buckling transition which, as we'll show, has yet occurred for F=19.9, 16.6 and 13.3 pN. Furthermore, for these forces, fluctuations around the equilibrium value are larger because the system is near the buckling point and so there is a continuous formation and destruction of plectonemes causing an instability in the extension of the braid.
For fixed *Ca* and *F*, by averaging the values belonging to the equilibrium plateaux (such as the ones reported in Figs. 5.2 and 5.3), one can extract the trend of the average braid extension as a function of *Ca*. An example is reported below in Fig. 5.4. [1]

The slope variation indicates that buckling occurred, so internal twist is converted into writhe (see Appendix C), giving rise to plectonemic nucleation. As the force increases, the buckling point moves to higher catenations.
We can draw the diagram of the phase transition *(Ca,F)* by fitting the two curves (before and after the plectonemes formation) for every force of Fig. 5.4 and finding their intersection point: this can be made both for positive and negative catenation values, but, due to the symmetry of the curve, the phase diagram would be specular for $Ca > 0$ and $Ca < 0$, so we report it only for positive catenations.
Fig. 5.5 shows an example of fit when the pulling force is $F = 10.0$ pN: by searching for the minimum reduced chi square, we find the two functions (indicated through red and green lines) which fit points before and after the transition. The points used in the unbuckled system (before the transition) correspond to the red dots, while the ones used for the buckled braid are identified by green dots. The abscissa of the intersection point between the two functions provides the value of the critical catenation Ca_c, i.e. the point where the buckling starts.
Table 5.2 and Fig. 5.6 show the transition point for several forces as a function of Ca_c.

[1] In plateaux with a fixed F and *Ca*, we consider only uncorrelated configurations. For example, if we look at Fig. 5.3 and focus on $F = 13.3$ pN, we follow this scheme: we choose a time from which the system has reached the equilibrium ($t^* > 9000\,\tau$) and we calculate the autocorrelation function (ACF) between different extension values, each of which corresponds to a time t such that $t^* < t < 120000\ \tau$. For $X_1, X_2, X_3 .... X_N$ measurements (i.e. extensions) and for a lag time i, this function is defined as: $ACF = \frac{\sum_{k=1}^{N-i}(X_k-\mu)(X_{k+i}-\mu)}{\sum_{k=1}^{N}(X_k-\mu)^2}$ where μ is the mean of the N data. In our case, N is the number of data in the plateau with a time t as defined above. One can say that these extensions are uncorrelated if $| ACF | \leq \frac{1.96}{\sqrt{N}}$: so, if ACF respects this condition when the lag time is i^*, we calculate the mean extension only taking those configurations with a time $t \geq t^*$ and divided by i^* steps. All results we'll report are averaged between 10 trajectories, namely, for each fixed force and catenation, we work with 10 simulative runs.

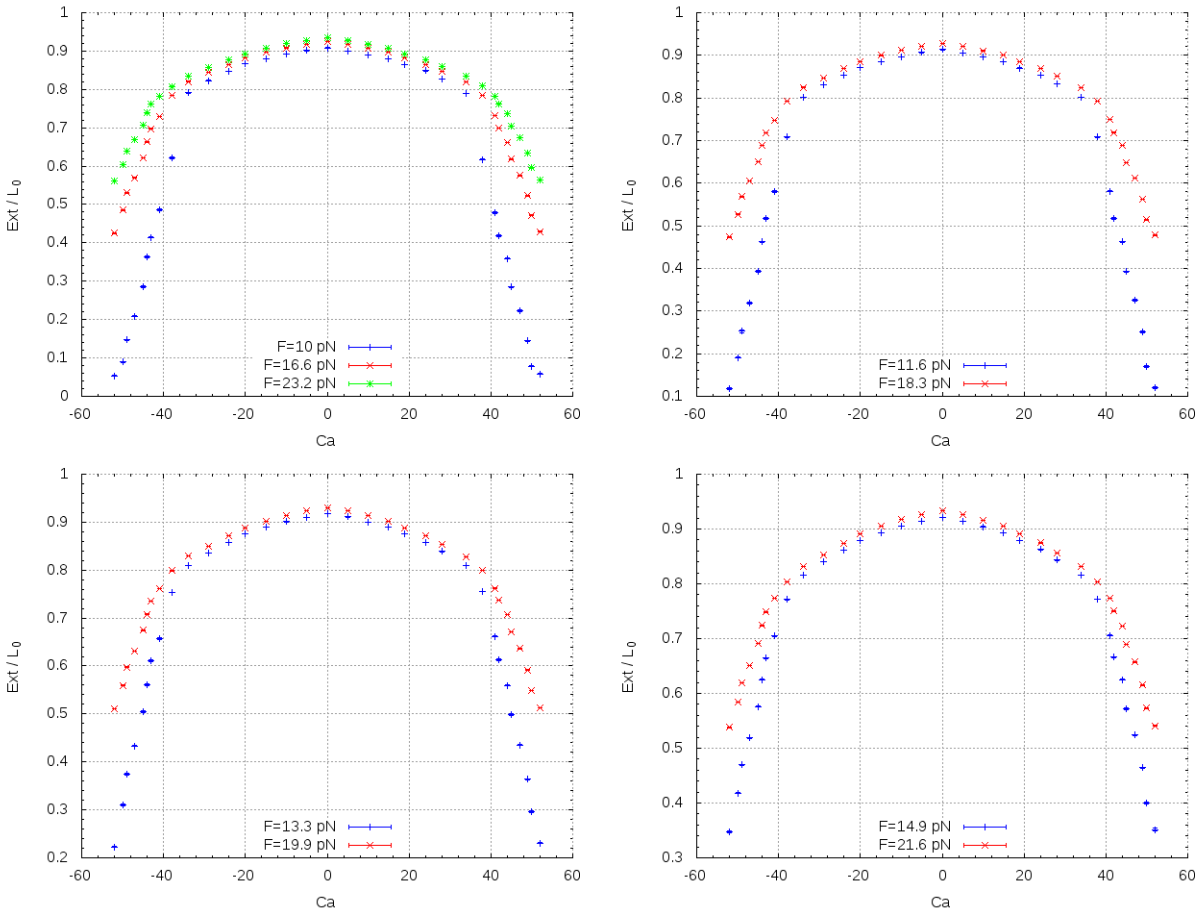

Figure 5.4: Normalized extension versus catenation for $d = 0.024L_0$ and different values of the force F.

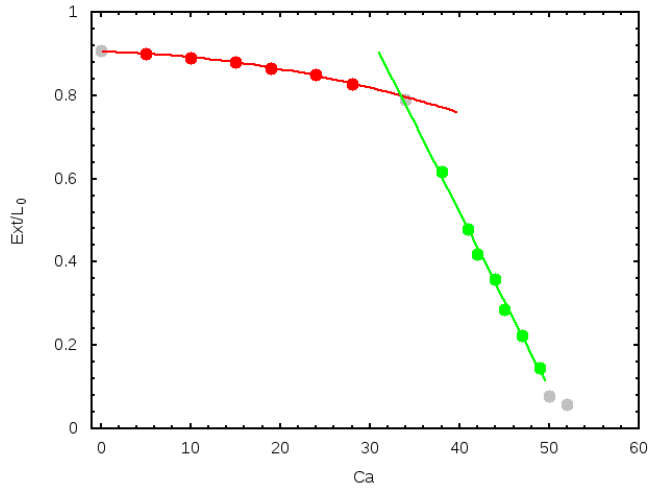

Figure 5.5: Example of fit for the case $F = 10.0$ pN and $d = 0.024L_0$.

Ca_c	σ_{Ca}	Force (pN)
33.5	0.5	10.0
35.9	0.4	11.6
37.8	0.4	13.3
38.9	0.6	14.94
39.4	0.6	16.6
39.9	0.5	18.3
40.2	0.5	19.9
40.6	0.6	21.6
41.1	0.5	23.2

Table 5.2: Values of the positive critical catenation (and its error) for each examined force.

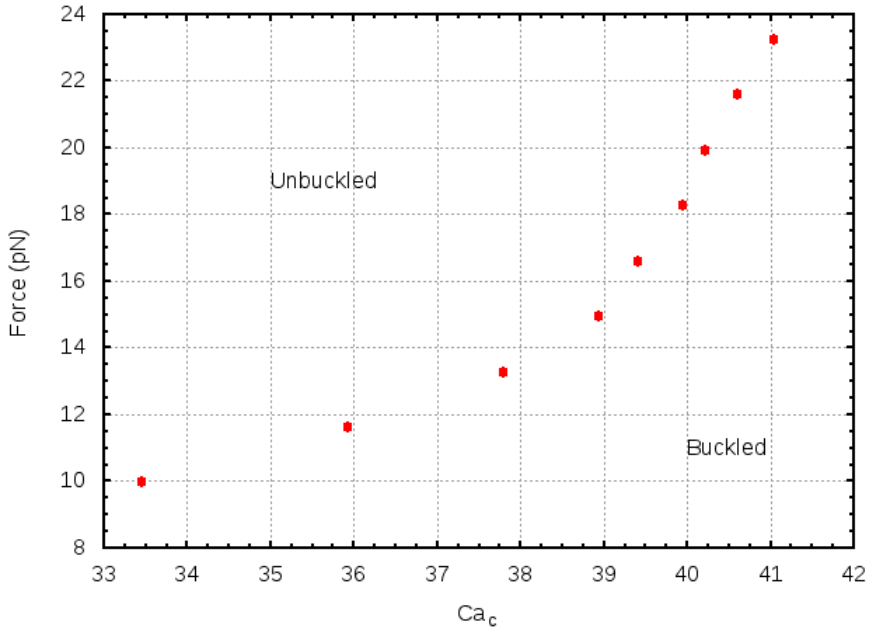

Figure 5.6: Force versus critical catenation for positive values of Ca. The diagram is divided into two regions: the *unbuckled* area includes those systems which are in the braided phase, while the *buckled* area contains systems that have yet undergone the buckling transition.

Another interesting property of the system to measure is the writhing number Wr (see Appendix C).

Writhe is used to describe supercoiling of DNA chains, but it also gives informations about the formation of plectonemes during braiding.
We study both the writhe of each strand and the writhe of the braid.
Working on the equilibrium plateau of the *extension vs time* curves, we calculate the mean between Wr_1 and Wr_2 where Wr_1 and Wr_2 refer to the writhe of the first (the blue one in Fig. 5.1) and second strand respectively . By plotting this average, indicated as Wr_{ss}, over the catenation, one obtains Fig. 5.7.
A similar study can be made for the curve C_{braid} relating to the braid. This curve is made up of points found by calculating the center of mass of the two strands when they're forming the braid.
In order to find these points, we consider each bead of the blue strand and we search for the bead of the red strand closest to it: we accept them as a pair only if the distance between them is smaller than 2σ.[2] If a blue bead doesn't have a red bead closer than 2σ it won't take part to the formation of the curve C_{braid}.
The writhe of C_{braid} is shown in Fig. 5.8.

[2]We set 2σ as cutoff because each bead is 1σ in diameter.

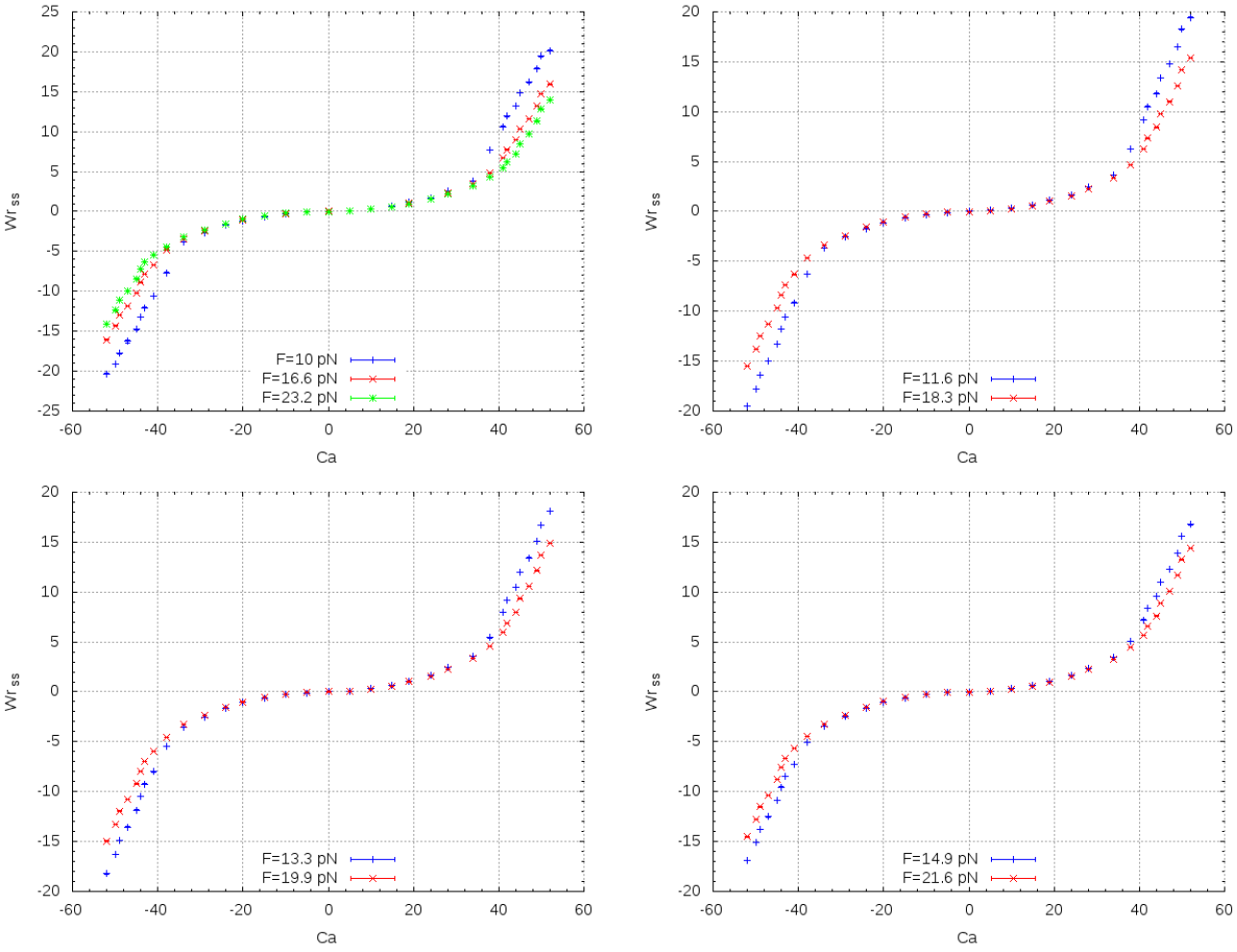

Figure 5.7: Writhe of the single strand (Wr_{ss}) as a function of the catenation for $d = 0.024L_0$ and different forces. Wr_{ss} corresponds to the average between Wr_1 and Wr_2.

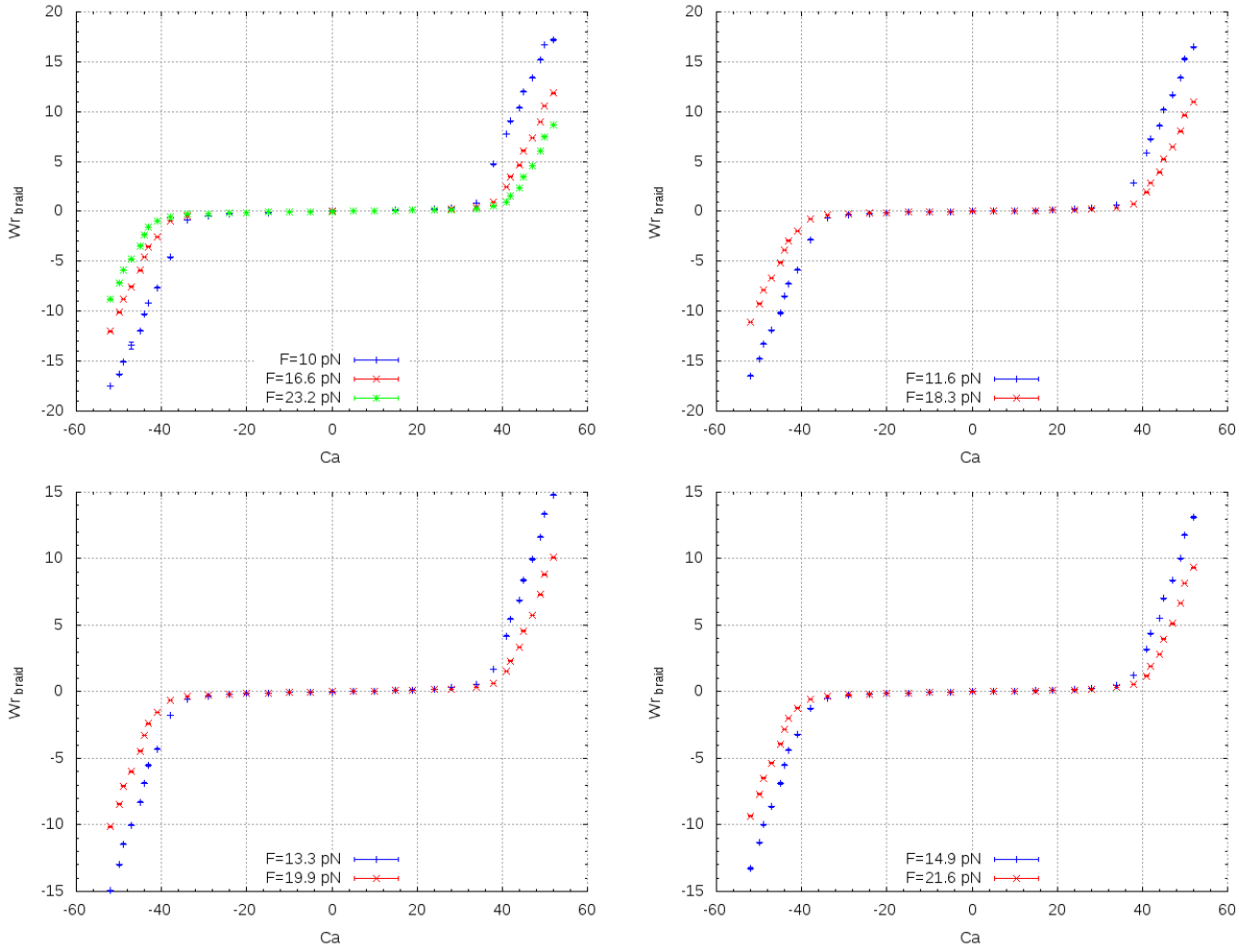

Figure 5.8: Wr_{braid} over catenation for $d = 0.024L_0$ and different forces .

In Figs. 5.7 and 5.8 the absolute value of the writhe increases with catenation, but Wr in Fig. 5.7 starts to raise for $|Ca| \simeq 20$, while in Fig. 5.8 this happens for $|Ca| \simeq 40$. The writhe of the single strand Wr_{ss} is generally higher than the one of the braid Wr_{braid} and this is due to the wrappings of a strand around the other one which increase Wr_{ss}: so the writhing number reported in Fig. 5.7 does not provide a sharp location of the buckling point as Wr_{braid} does.
In fact the curve C_{braid}, that is a kind of backbone of the braid, is characterized by a Wr_{braid} approximately equal to zero until there isn't the buckling transition and then its value suddenly increases (or decreases for Ca<0).

Finally we study the number of plectonemes and their length.
To detect plectonemes we look at the contact maps of each strand: a contact map is a two-dimensional heat map as the one in Fig. 5.9.

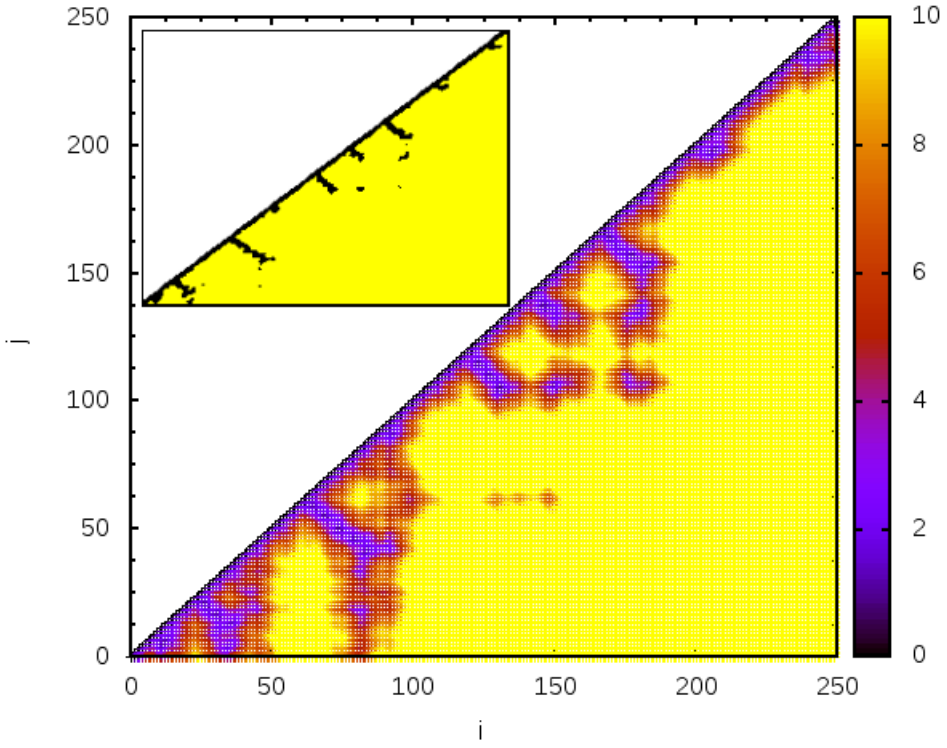

Figure 5.9: Example of a contact map for the blue strand when $Ca = 52$ and $F = 13.3$ pN. In the inset we show the same contact map, but with a cutoff on the physical distance equal to 3σ: all the black areas represent beads (i,j) such that $dist(i, j) \leq 3\sigma$. There are 5 main black regions moving away from the diagonal and, indeed, this configuration is characterized by 5 plectonemes.

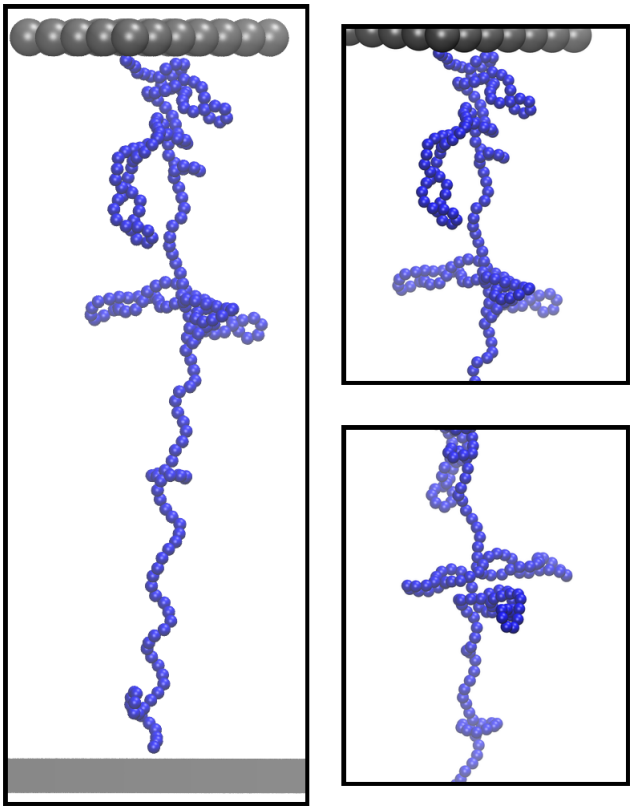

Figure 5.10: Snapshot of the blue strand corresponding to the contact map in Fig. 5.9. In the two right panels one can observe a zoom on the plectonemes.

We now give a brief description of how we obtain Fig. 5.9 which is referred to the blue strand and to a given configuration obtained during runs with Ca=52 and F=13.3 pN (see Fig. 5.10).

- x-axis: in the x axis we find the i-index that is included between 1 and 250, in other words it indicates the identification (ID) number (see Appendix A) of beads forming the blue chain;

- y-axis: in the y-axis there is the j-index that moves from 1 to i, so it refers to blue beads whose ID number has a value between 1 and i;

- colour palette: the colour palette provides the distance (in sigma units) between the beads i and j. A cut-off of 10σ is set, so that if i and j have a distance greater than it, in Fig. 5.9 we report a distance of 10σ anyway.

A similar map can be obtained for every configuration with fixed catenation, both for the blue and the red strand.
Note that in map 5.9 there are blue-violet regions moving away from the diagonal. This is a signal of the plectonemic nucleation: in fact, in the lower extremity of these regions (the extremity with a smaller value of j), one finds two beads (i and j) which are far along the backbone but spatially close (see Fig. 5.11). This condition occurs when a plectoneme forms, so we can use contact maps to locate plectonemic domains and determine their length.

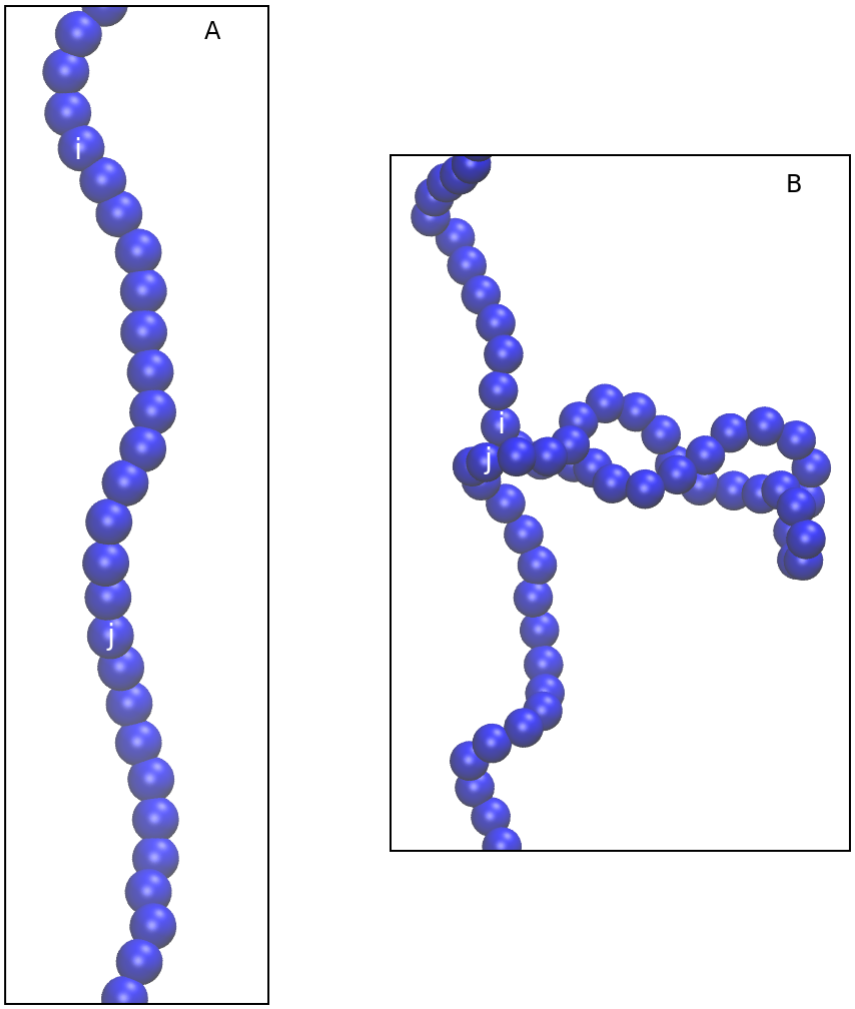

Figure 5.11: Difference between the braided and the plectonemic phase. (A): in the braided phase two beads numerically far (e.g. $\mid i - j \mid > 10$) are separated by a large physical distance. (B): at the starting point of a plectoneme we find two close beads whose ID numbers are diveded by a remarkable distance.

However other considerations are required here.
First of all it's important to note that plectonemes end-loops are placed at the beginning parts of the blue-violet regions [3] : here we find beads with a similar ID number and a small physical distance, which are characteristics of plectonemes end-loops.
Instead the starting beads of a plectonemic domain are found in the lower extremities of these regions, so, if we want to know its length, we have to pinpoint the far ends. The cutoff for the physical distance is 3σ: when we find two points i and j such that $dist(i,j) \leq 3\sigma$, we focus on them because they can be signal of a plectonemic domain as the one in panel (A) of Fig. 5.12. Here it's possible to observe that the two red beads A and B are divided by a distance of about 3σ (since every bead is 1σ in diameter). Obviously the distance between A and B could be greater (for example if the superhelix doesn't form a *compact* structure, as the plectoneme *1* in panel (B) of Fig. 5.12), but by imposing a cutoff bigger than 3σ we would consider a greater number of beads that are physically near, but they don't belong to the same plectoneme (Fig. 5.13). This would provoke evident errors in the determination of plectonemes length.

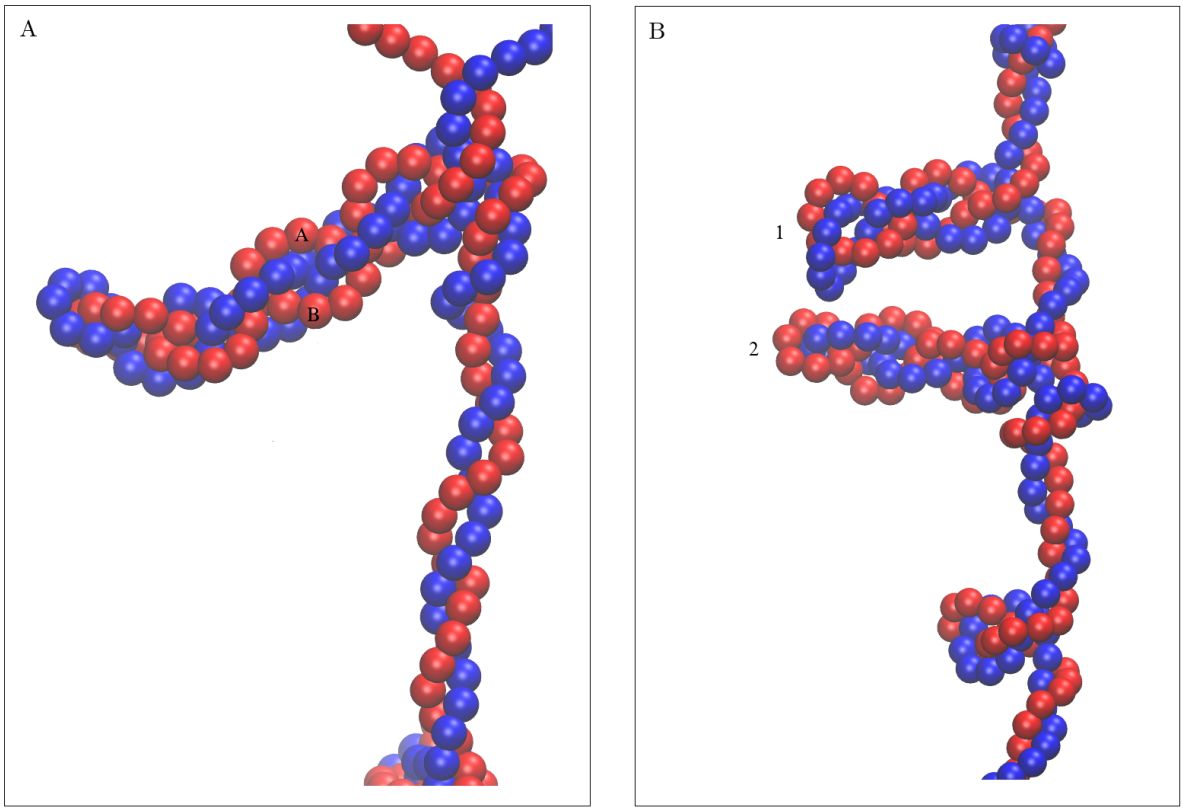

Figure 5.12: Different plectonemes that can nucleate during braiding

[3] With the term *beginning part* we mean the blue-violet area closer to the diagonal.

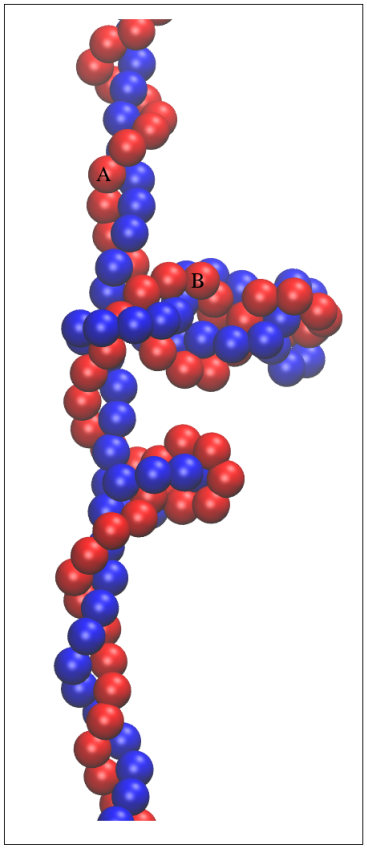

Figure 5.13: Beads A and B have a distance included between 3σ and 4σ: if we set 4σ as the cutoff, we would commit important errors in the determination of the initial and final beads of the plectoneme, i.e. in its length.

Another problem emerging from Fig. 5.9 is the size of the blue-violet regions. Clearly it's necessary to set a minimal length (i.e. a minimal numerical distance between i and j) above which we accept that region as a plectoneme. It's possible to see that near the diagonal there are numerous point pairs characterized by a distance lower than 3σ, but not all belong to a plectoneme. For example the blue-violet areas for $i \simeq 210$ and $j \simeq 200$ are due to wrappings of the blue strand around the red one. Therefore setting a threshold for the numerical distance between i and j allows us to distinguish between plectonemes and simple windings of a strand. This numerical cutoff is 13: by depicting the braid as a ribbon with a thickness of 2σ and looking at the smallest possible plectoneme (represented in Fig. 5.14), one can say that its circumference is equal to $4\pi\sigma$, so it includes $\frac{4\pi\sigma}{\sigma} \simeq 13$ beads.

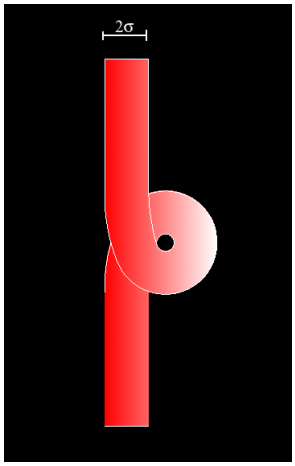

Figure 5.14: We can think about the braid as a ribbon 2σ in thickness: if we approximate the smallest possible plectoneme as a circumference, we can say that it contains almost 13 beads.

Finally it's necessary to pay attention to possible *spots* far from the diagonal, such as the one in Fig. 5.9 for $i \simeq 150$ and $j \simeq 110$. The origin of these spots is due to the approach between beads belonging to two different plectonemes, so they must be excluded when we're counting the number of plectonemic domains. Simply by imposing that a plectoneme is localized when we find two beads (i,j) such that $dist(i,j) \leq 3\sigma$ and $\mid i-j \mid = 13$, we are able to exclude most of these spots (which often correspond to a couple (i,j) with $\mid i-j \mid > 13$). Thanks to all these thresholds, once localized a plectoneme, we can move through the corresponding blue-violet region and find its extremity far from the diagonal, i.e. we can calculate the length of the domain.
By taking into consideration all the previous warnings, we can now evaluate the plectonemes number (N_{plect}) and their length (L_{plect}).
We use contact maps both for the blue and red strand, but sometimes the number of plectonemes in the two chains is different. This situation occurs because some wrappings of a strand around the other can satisfy the conditions which define a plectoneme($dist(i,j) \leq 3\sigma$ and $\mid i-j \mid = 13$), so our method counts an excess of plectonemic domains (see Fig. 5.15).

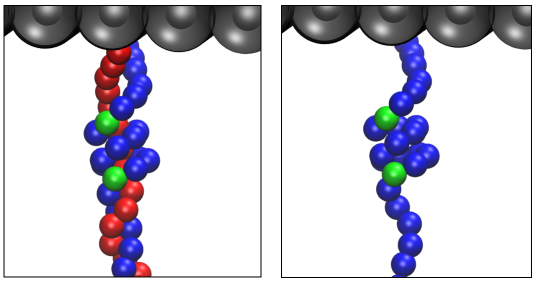

Figure 5.15: The two green beads (belonging to the blue strand) satisfy the conditions required for a plectonemic domain ($\mid i-j \mid = 13$ and $dist(i,j) \leq 3\sigma$), but they don't locate a plectoneme of the braid. The snapshot is obtained from a run with $d = 0.024\, L_0$, $F = 23.2$ pN and $Ca = 50$.

To avoid this problem we choose to take the minimum value between N_{p1} and N_{p2} where N_{p1} and N_{p2} are respectively the number of plectonemes in the blue and in the red strand. If this value correspond to N_{p1}, the lengths of plectonemes are deduced by contact maps of the blue chain [4] ; supposing that a plectoneme contains N beads, its length is $N\sigma$.
The plectonemes length reported in figures below is the total length of that part of the braid which underwent the transition .
Note that N_{plect} and L_{plect} are obtained by considering only uncorrelated data that belong to the equilibrium plateau of the extension seen in Figs. 5.2 and 5.3. In Figs. 5.16 and 5.17 we show the behavior of these two quantities as a function of the catenation.

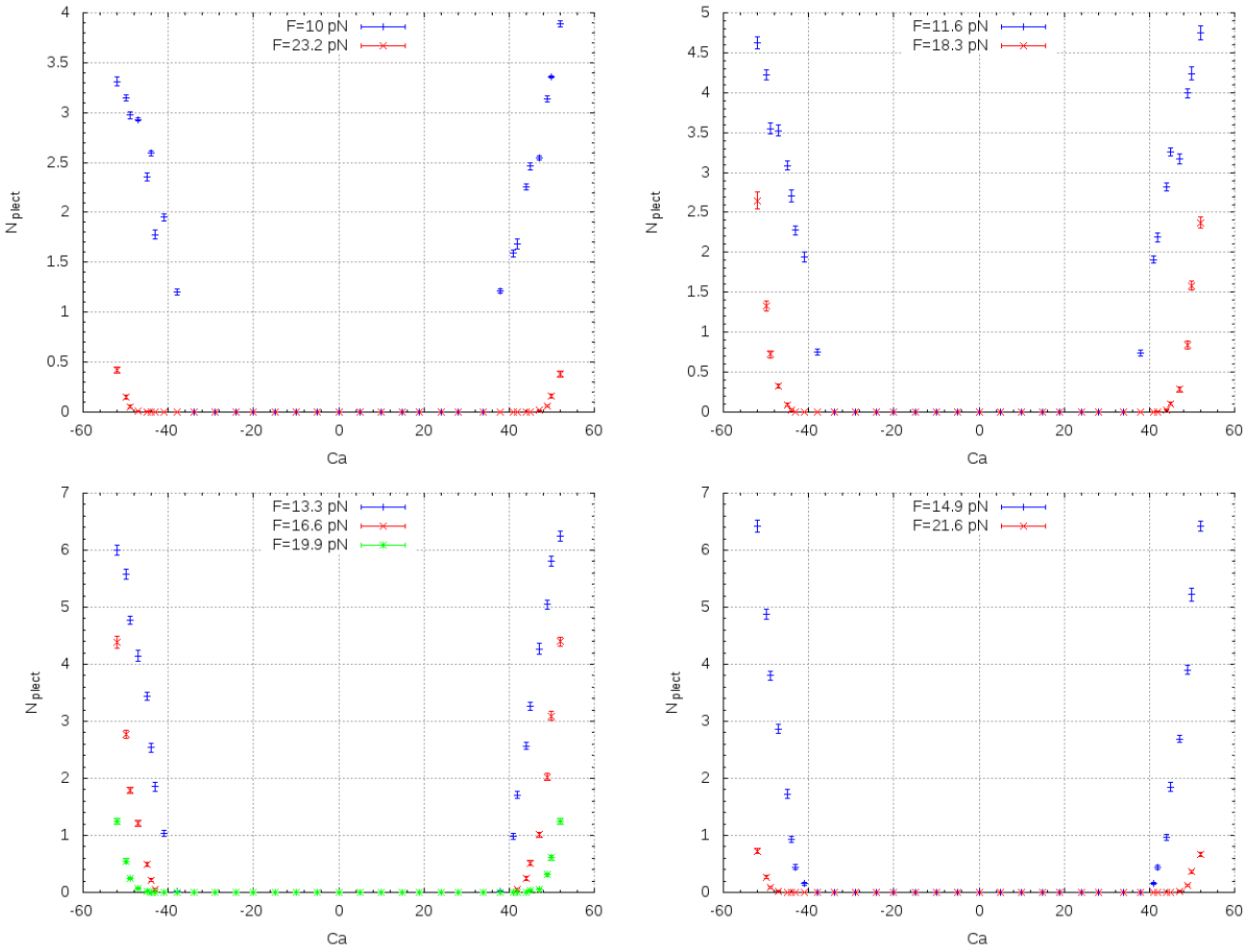

Figure 5.16: N_{plect} versus catenation for $d = 0.024\,L_0$.

[4] If $N_{p1} = N_{p2}$ the plectonemic length is given by the blue strand.

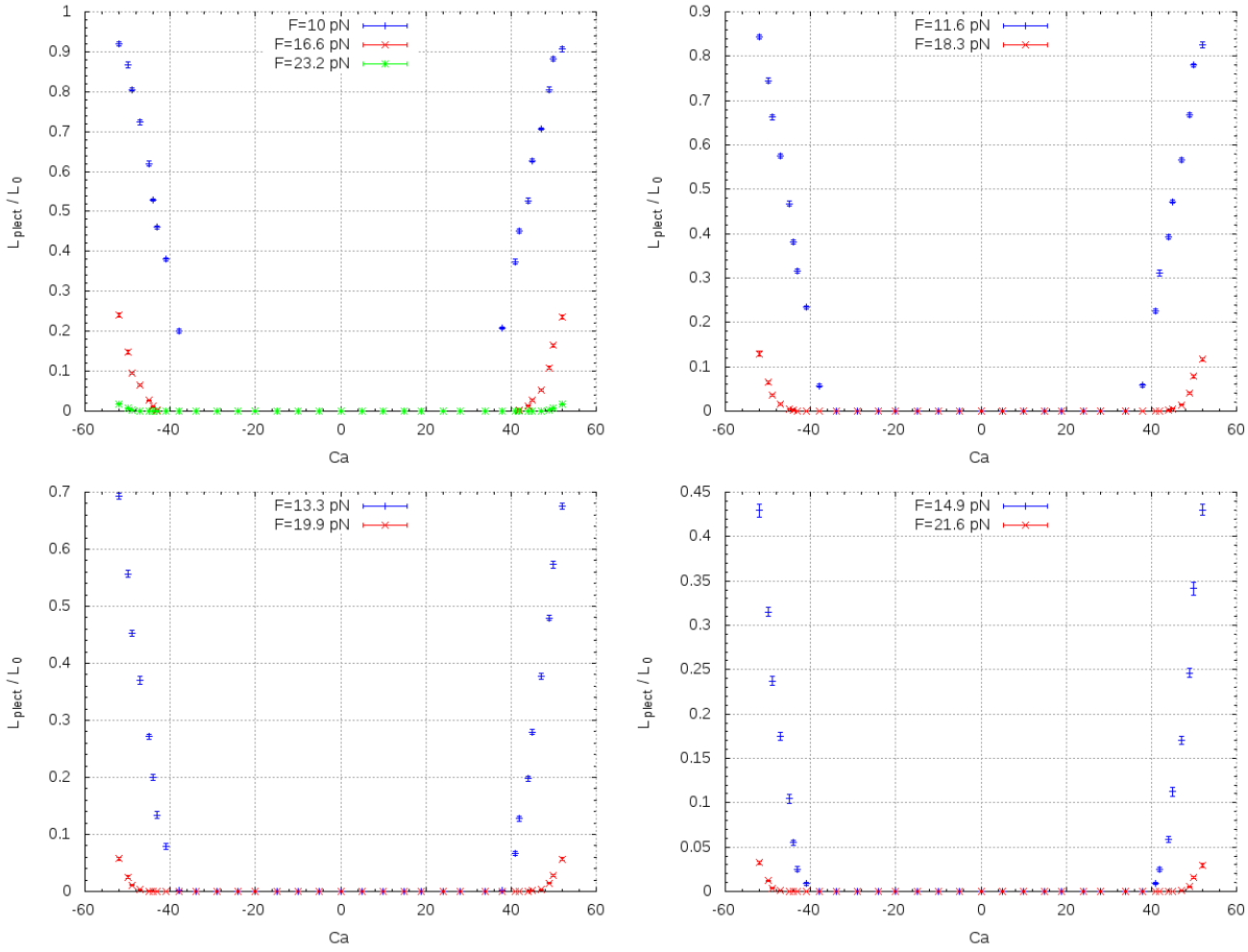

Figure 5.17: Total length of the plectonemic phase versus catenation for $d = 0.024\,L_0$.

5.2 Increasing the intertether distance: d=0.168L_0

We now study a braid formed by two strands separated by a larger intertether distance d: we set $d = 42\sigma$, therefore $d = 0.168\, L_0$.

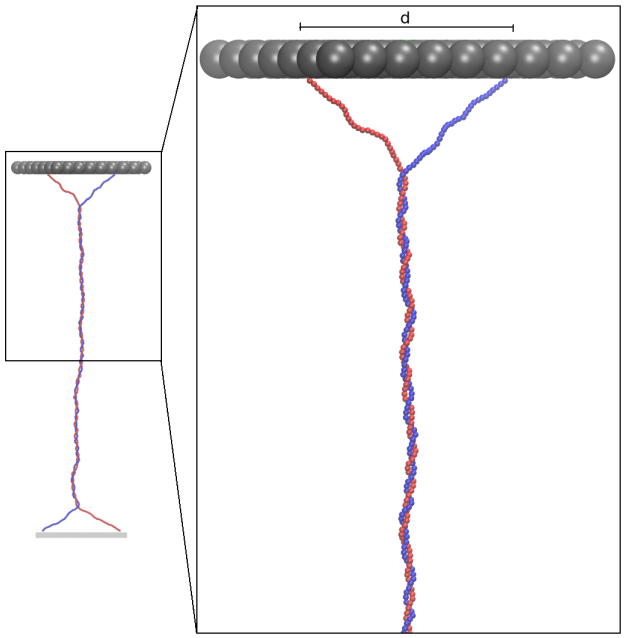

Figure 5.18: Example of the setup used for $d = 0.168\, L_0$, $Ca = 23$ and $F = 11.6$ pN. A zoom is reported on the right.

For this case we investigate the following forces:

Force (pN)	
10.0	11.6
13.3	14.9
16.6	18.3
19.9	

Table 5.3: Values of the forces used in the setup $d = 0.168\, L_0$.

As in the previous paragraph, we work with fixed catenation searching for the equilibrium of the extension. We obtain Fig. 5.19 by averaging over the extension values that form plateaux.

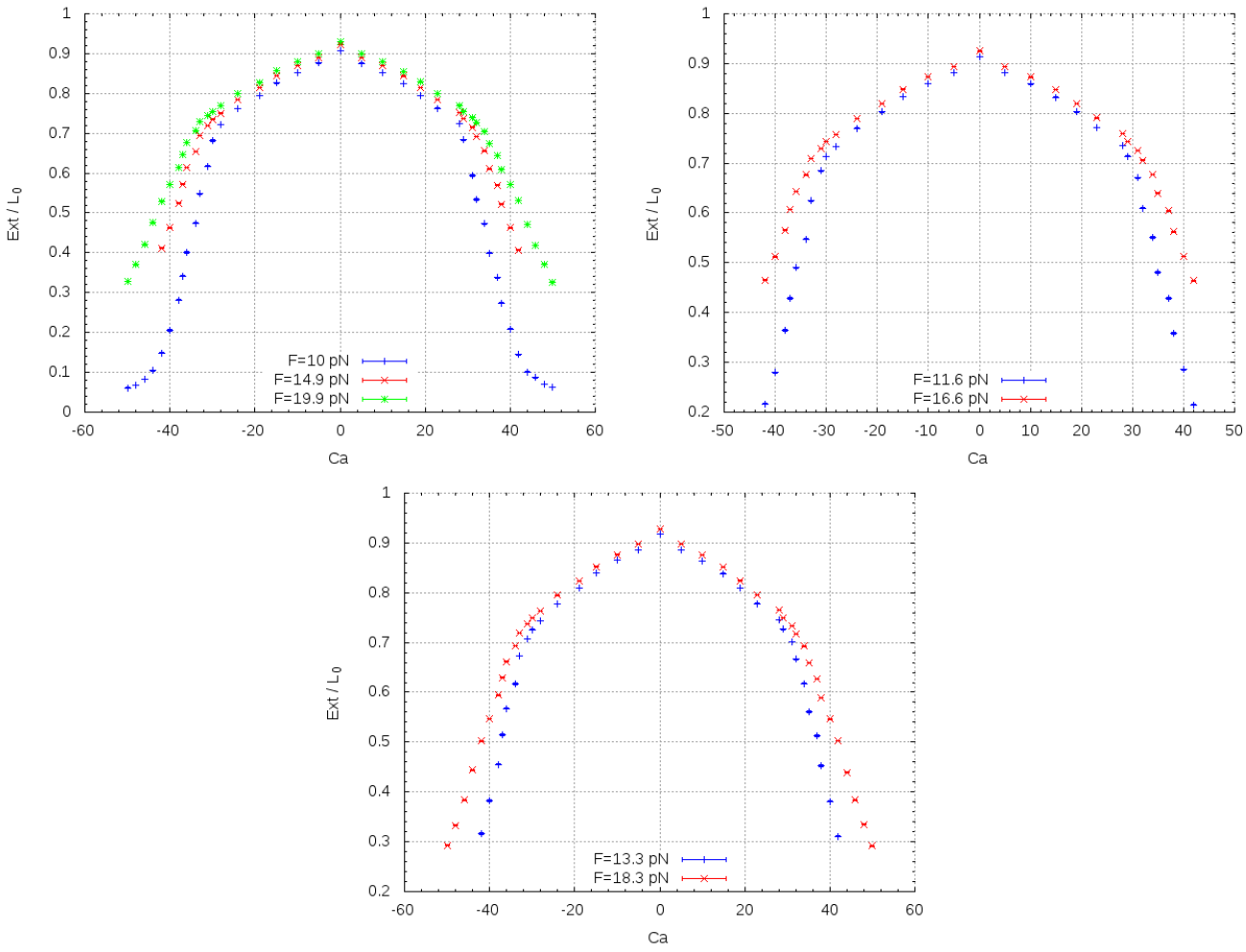

Figure 5.19: Normalized extension versus catenation for $d = 0.168\,L_0$.

For each force, the change in the curve slope reveals the buckling transition, which occurs for the critical catenations Ca_c shown in Table 5.4.

Ca_c	σ_{Ca}	Force (pN)
28.0	0.5	10.0
29.7	0.6	11.6
31.8	0.4	13.3
32.8	0.4	14.9

Ca_c	σ_{Ca}	Force (pN)
33.6	0.9	16.6
34.2	0.6	18.3
34.6	0.7	19.9

Table 5.4: Values of positive critical catenation (and its error) for each examined force.

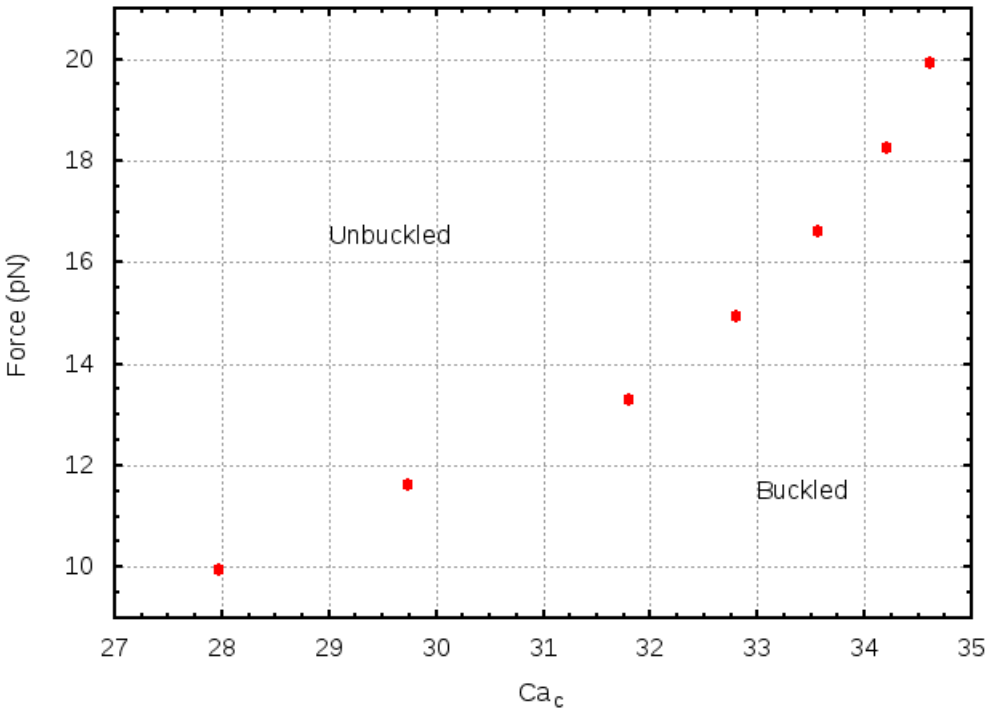

Figure 5.20: Force versus critical catenation for positive values of Ca.

By recalling what we said in Chapter 3, one notes that the buckling transition is shifted towards lower values of Ca as the intertether distance increases (see Fig. 3.2).

As in the case $d = 0.024\,L_0$, even now the writhing number is a useful quantity to check and its behavior is reported in the underlying graphics.

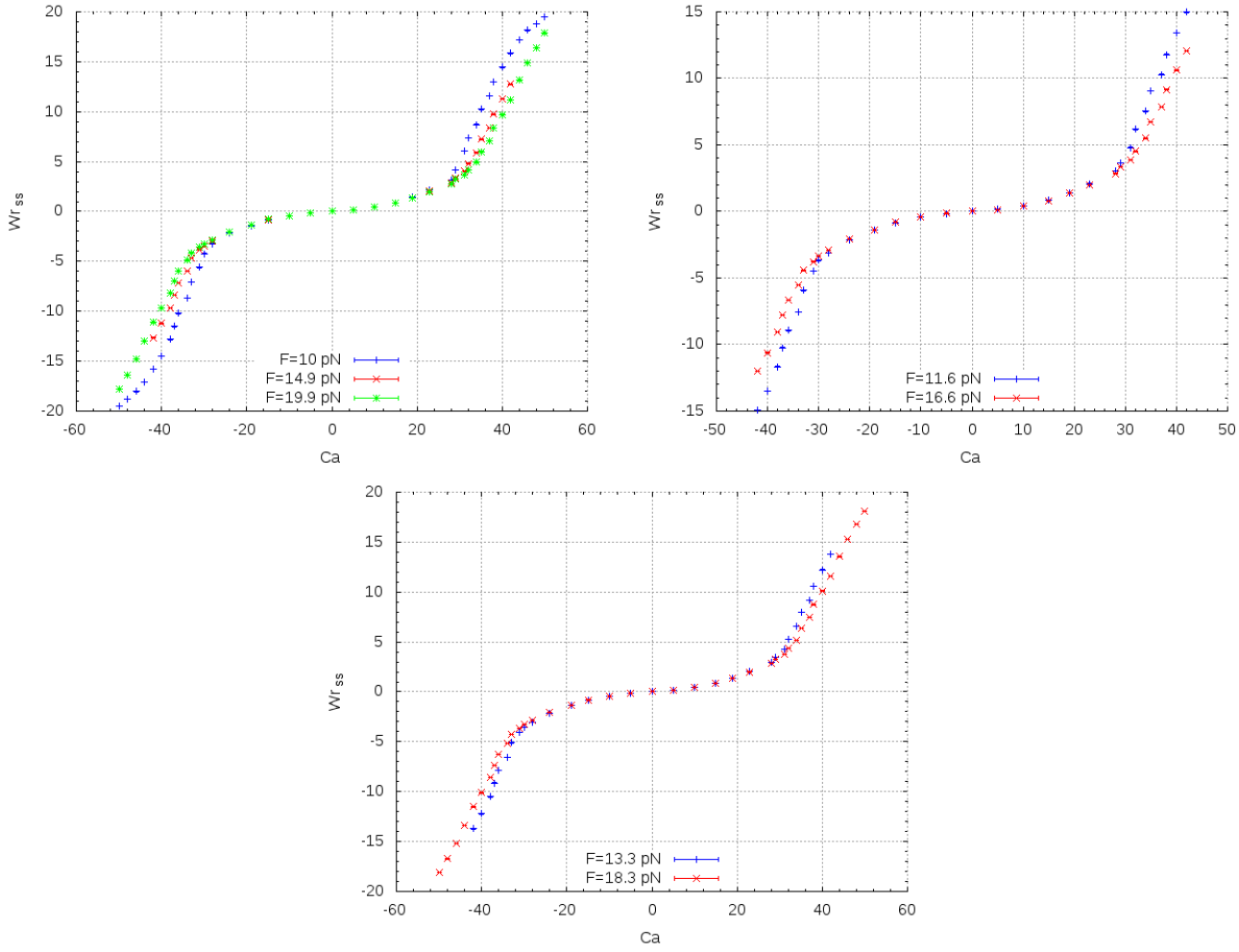

Figure 5.21: Writhe of the single strand versus catenation for $d = 0.168\, L_0$.

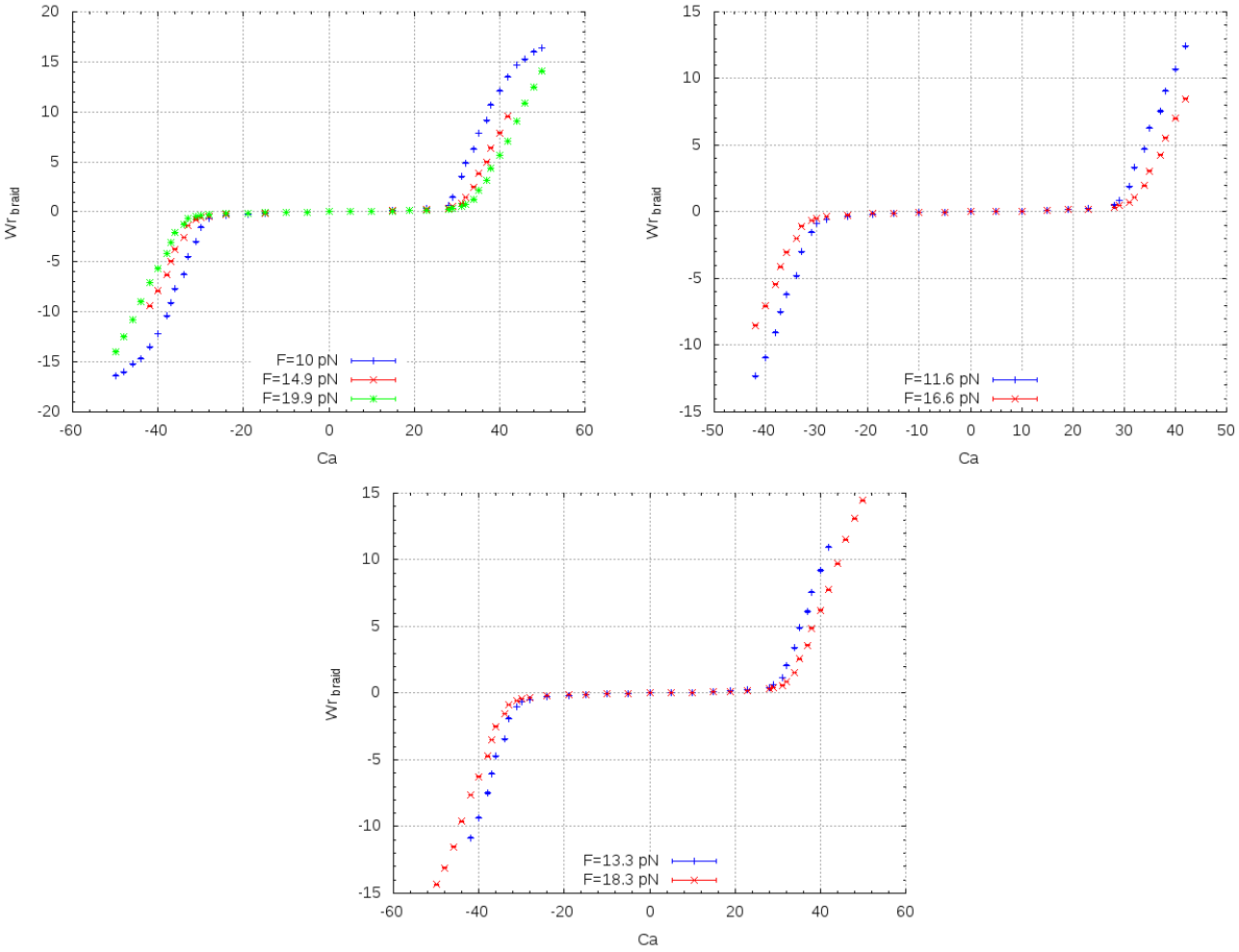

Figure 5.22: Writhe of the braid as a function of the catenation for $d = 0.168\,L_0$.

Once again it's possible to notice that Wr_{ss} doesn't highlight the buckling transition, since it starts to raise before the Ca_c; instead Wr_{braid} is a more reliable tool.
Finally we're interested in studying the number and the length of plectonemic domains: we employ contact maps with the same conditions seen in Section 5.1, obtaining Figs. 5.23 and 5.24.

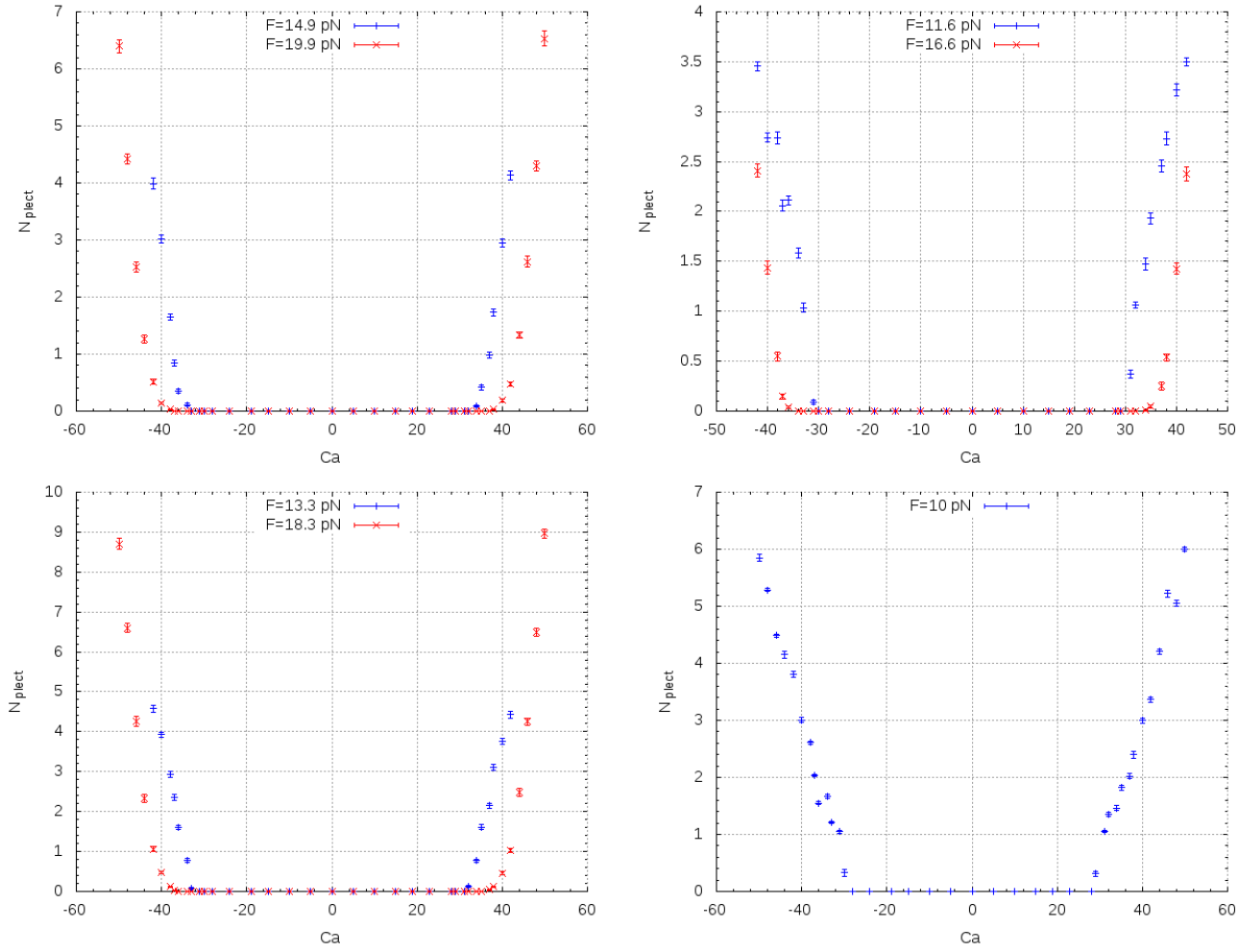

Figure 5.23: Number of plectonemic domains versus catenation for $d = 0.168\, L_0$.

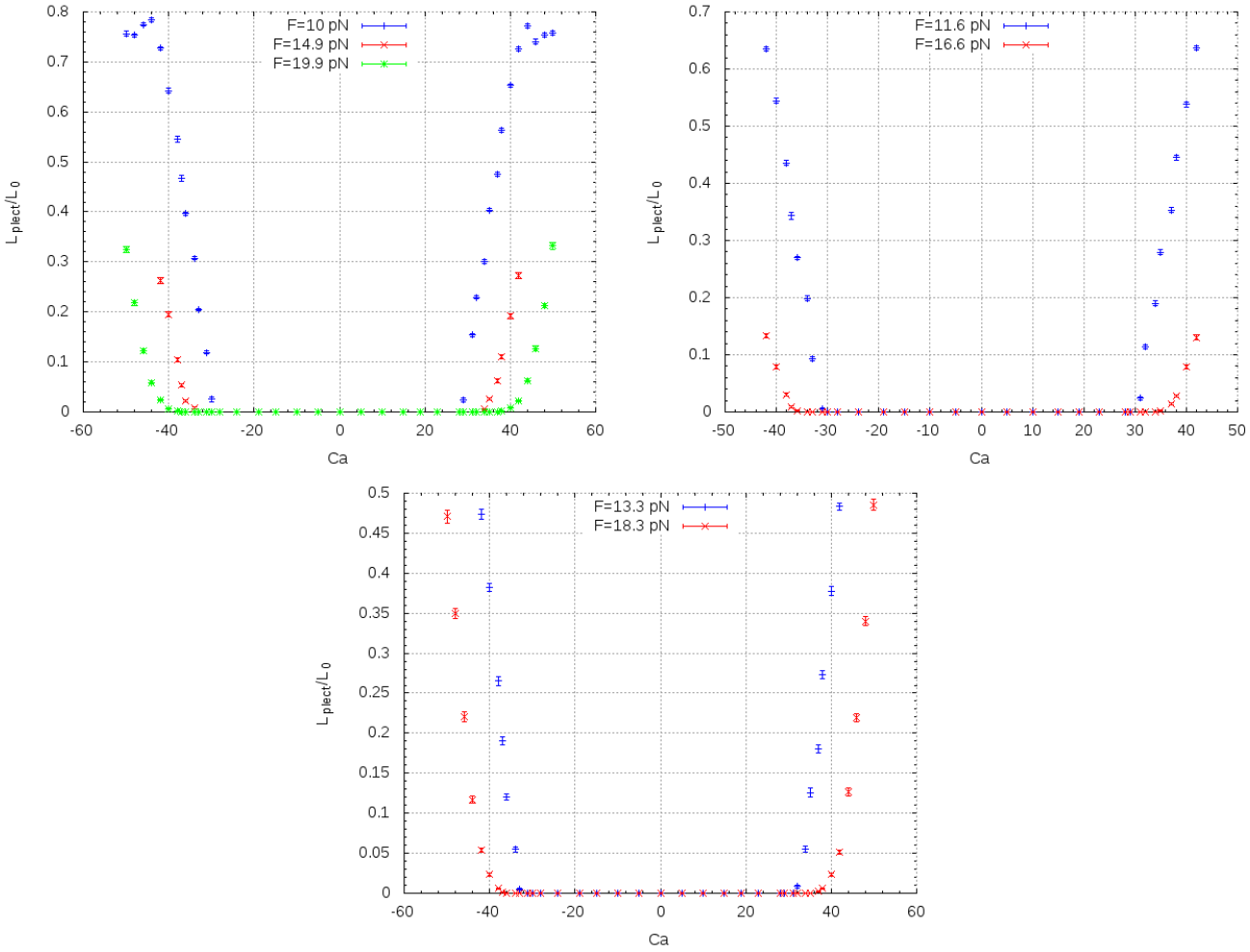

Figure 5.24: Normalized length of the plectonemic phase over catenation for $d = 0.168\,L_0$.

In Fig. 5.24 it's interesting to note that the curve for F=10 pN reveals an evident drop when $Ca \gtrsim 45$: its origin will be discuss in Section 5.4.

5.3 Large intertether distance: d=0.48L_0

The last configuration we study is the one in which the two strands are separated by a distance almost equal to half of their length: $d = 0.48\,L_0$.

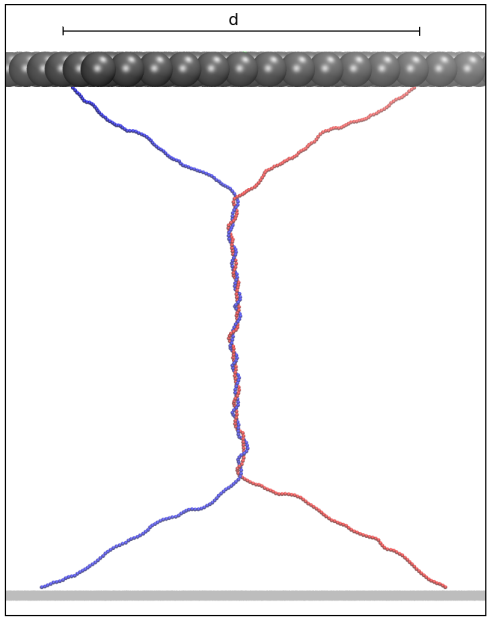

Figure 5.25: Example of the setup for $d = 0.48\,L_0$, $Ca = 13$ and $F = 8.3$ pN.

We study this setup for the forces reported in Table 5.5.

Force (pN)	
6.6	11.6
8.3	13.3
10.0	14.9

Table 5.5: Values of the forces used in the setup $d = 0.48L_0$

Note that the *Ext vs Ca* curves reported in 5.26 exhibit an abrupt decrease after the first half catenation since d is much larger than in the previous two cases: this is due to the formation of the first helical bend which requires a greater length of the end regions (see panel (b) of Fig. 2.4) as d increases.

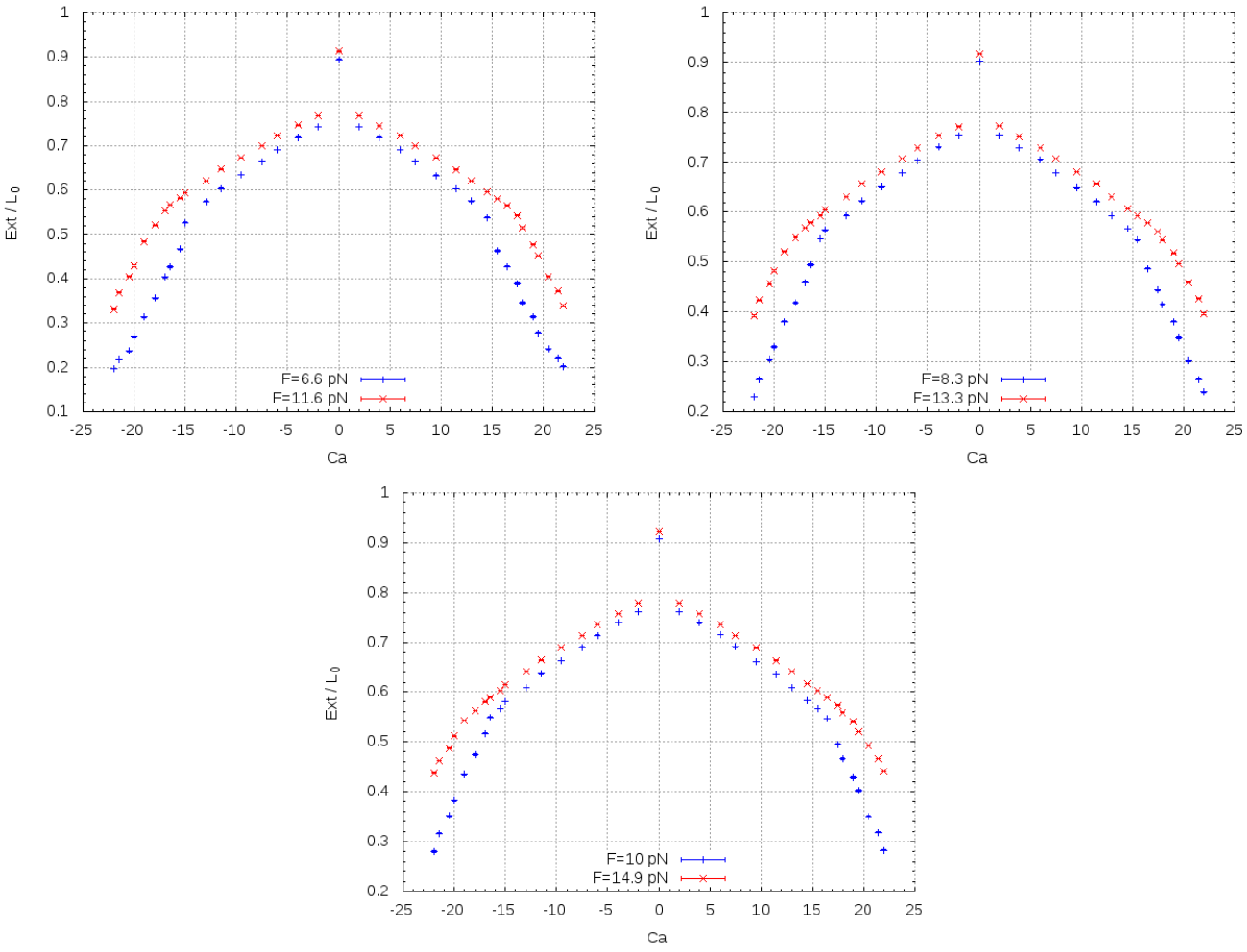

Figure 5.26: Normalized end-to-end distance over Ca for $d = 0.48\,L_0$.

As before, we can fit our data and estimate the critical catenation corresponding to the buckling transition. These estimates are reported in Table 5.6 and, as points, in the (Ca_c, F) phase diagram of Fig. 5.27.

Ca_c	σ_{Ca}	Force (pN)
13.7	1.2	6.6
14.6	0.3	8.3
15.7	0.2	10.0

Ca_c	σ_{Ca}	Force (pN)
16.7	0.2	11.6
17.5	0.2	13.3
18.1	0.3	14.9

Table 5.6: Estimates of the positive critical catenation (and its error) for each force.

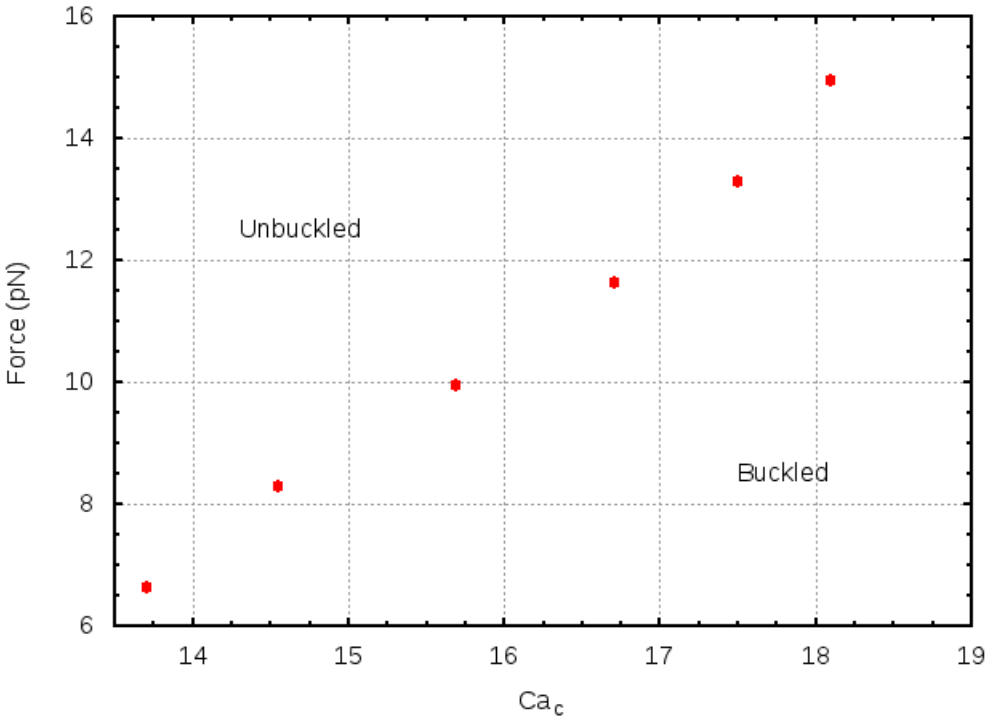

Figure 5.27: (Ca_c, F) phase diagram for positive values of Ca.

By employing the same techniques described in Section 5.1, we obtain informations about the writhe of the single strand Wr_{ss} and the writhe of the braid Wr_{braid}. As in Sections 5.1 and 5.2, Wr_{ss} corresponds to the average value between the writhe of the blue and the red strand (Wr_1 and Wr_2), while Wr_{braid} is calculated by moving along the the backbone of the braid as seen for the case $d = 0.024\, L_0$. The (Ca, Wr_{ss}) and (Ca, Wr_{braid}) graphics are reported in Figs. 5.28 and 5.29.

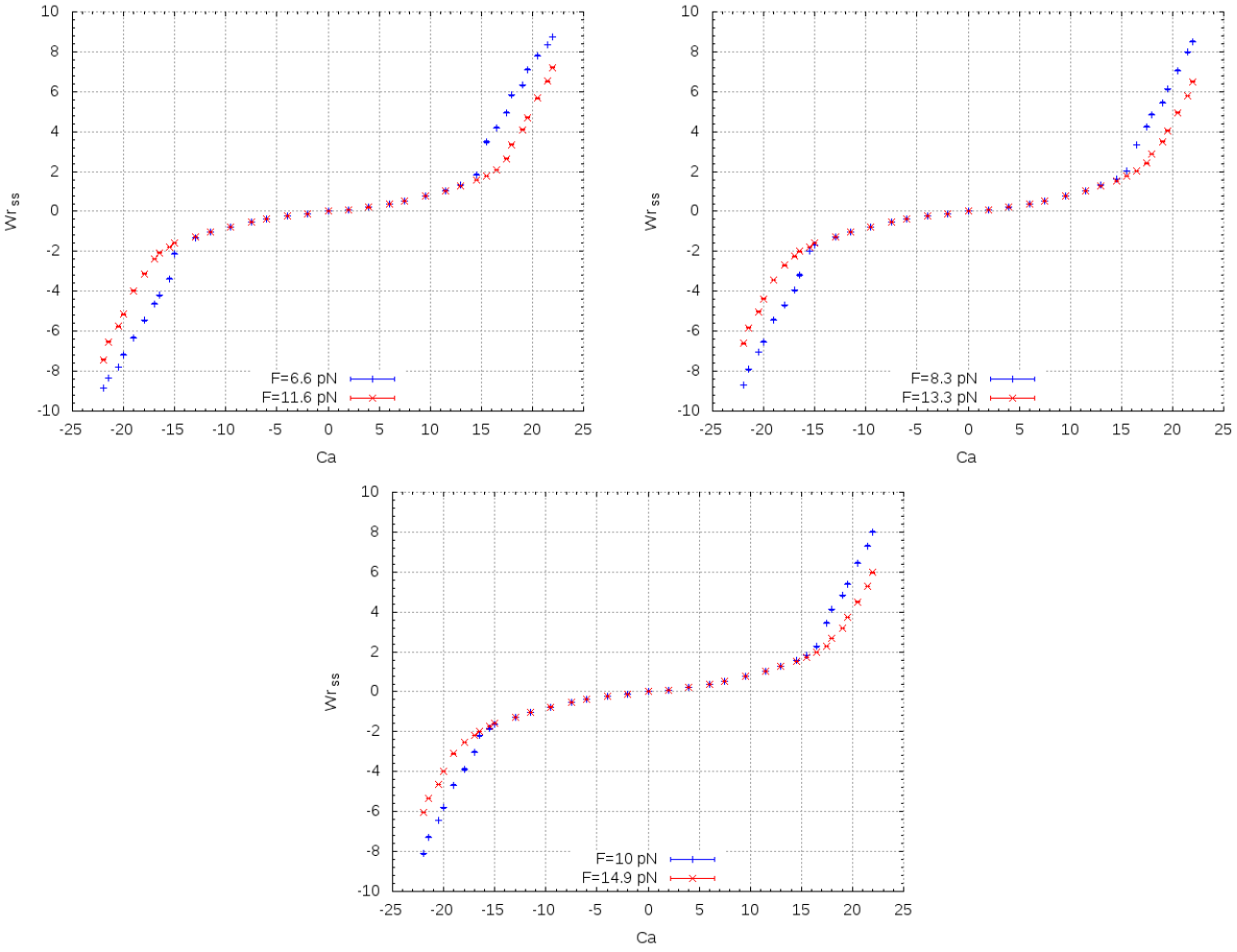

Figure 5.28: Wr_{ss} as a function of Ca for $d = 0.48\,L_0$.

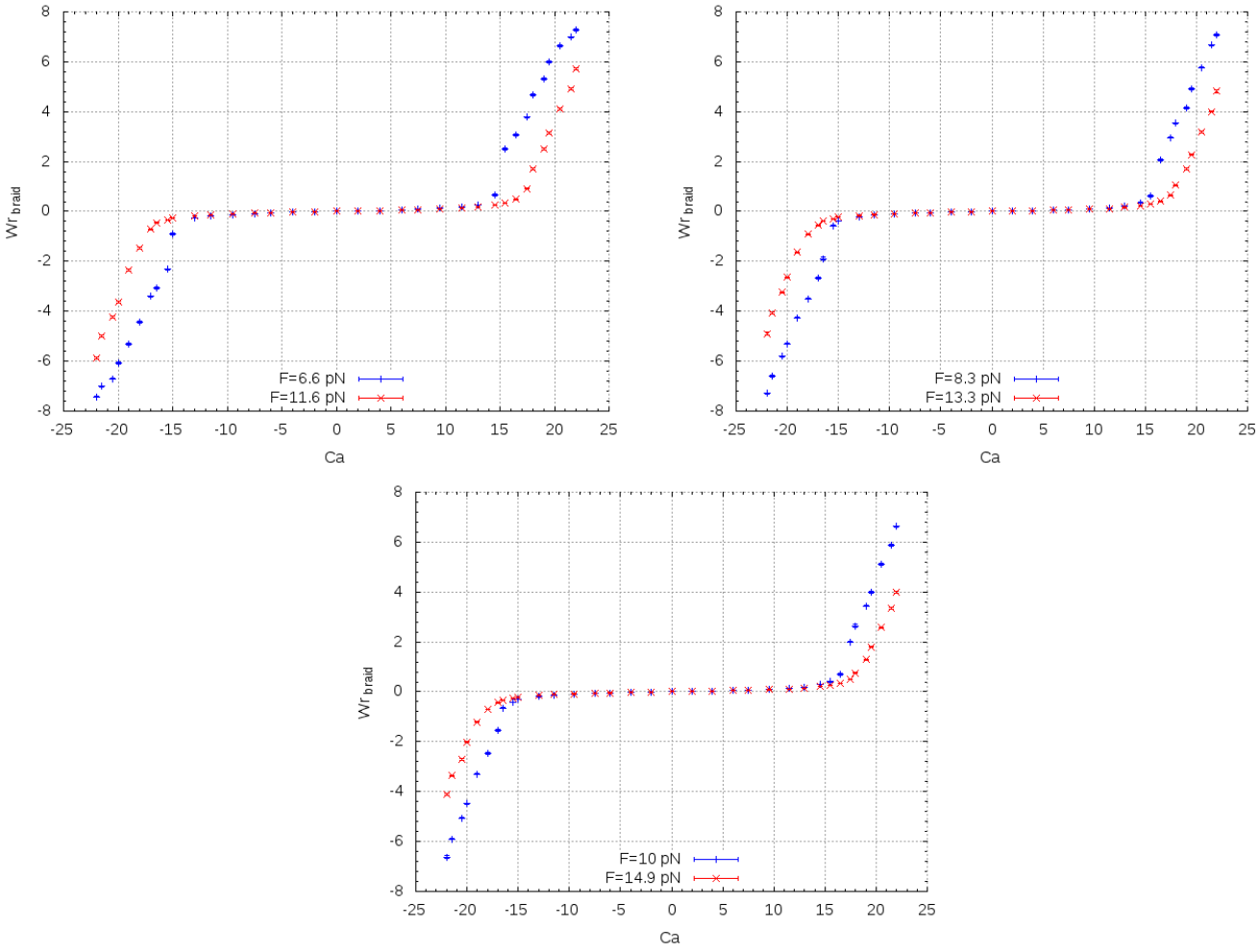

Figure 5.29: Writhe of the braid versus Ca for $d = 0.48\,L_0$.

Finally, contact maps allow us to investigate the statistics of plectonemes. In Figs. 5.30 and 5.31 we show their number and length as a function of the catenation.

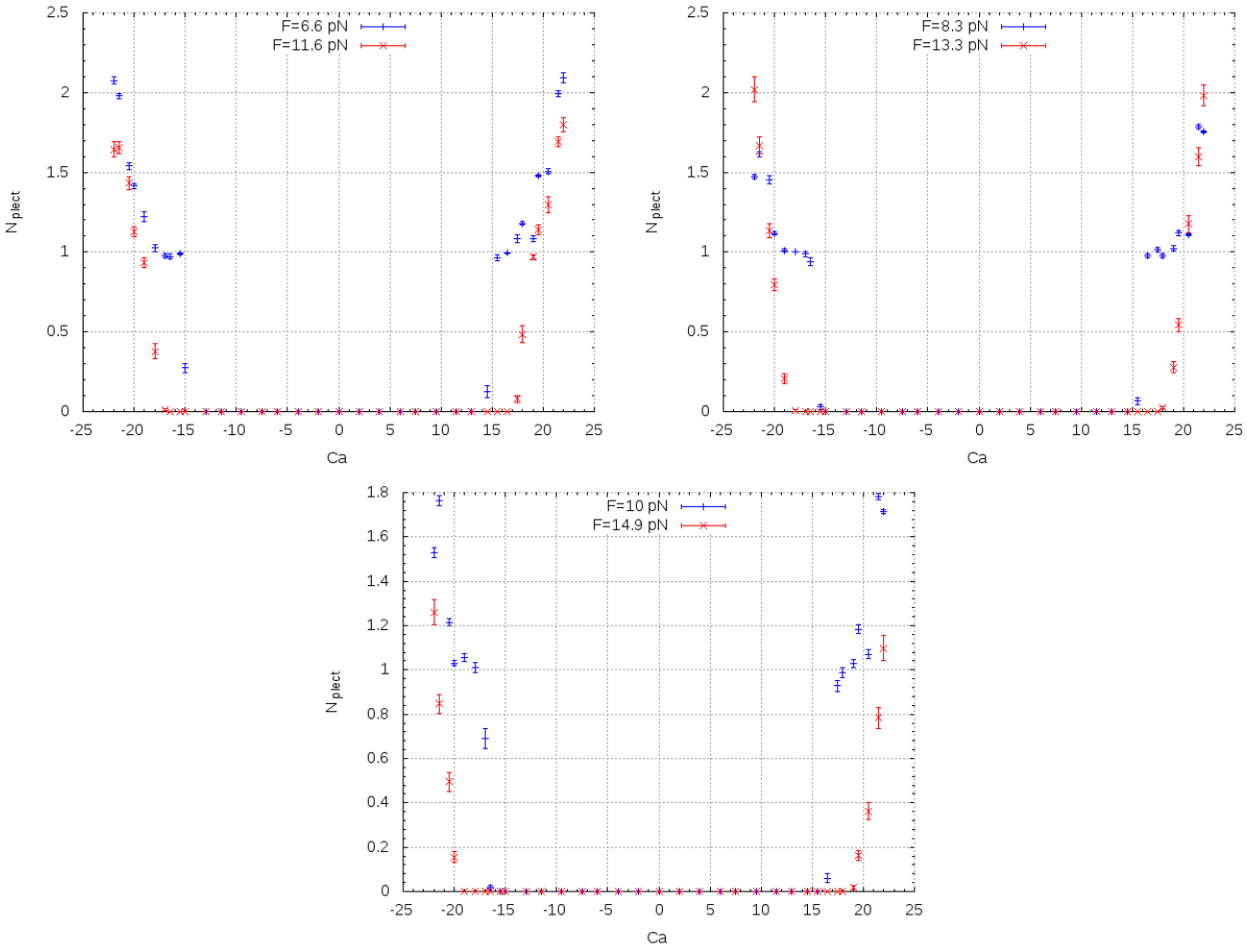

Figure 5.30: Number of plectonemic domains as a function of the catenation for $d = 0.48\,L_0$.

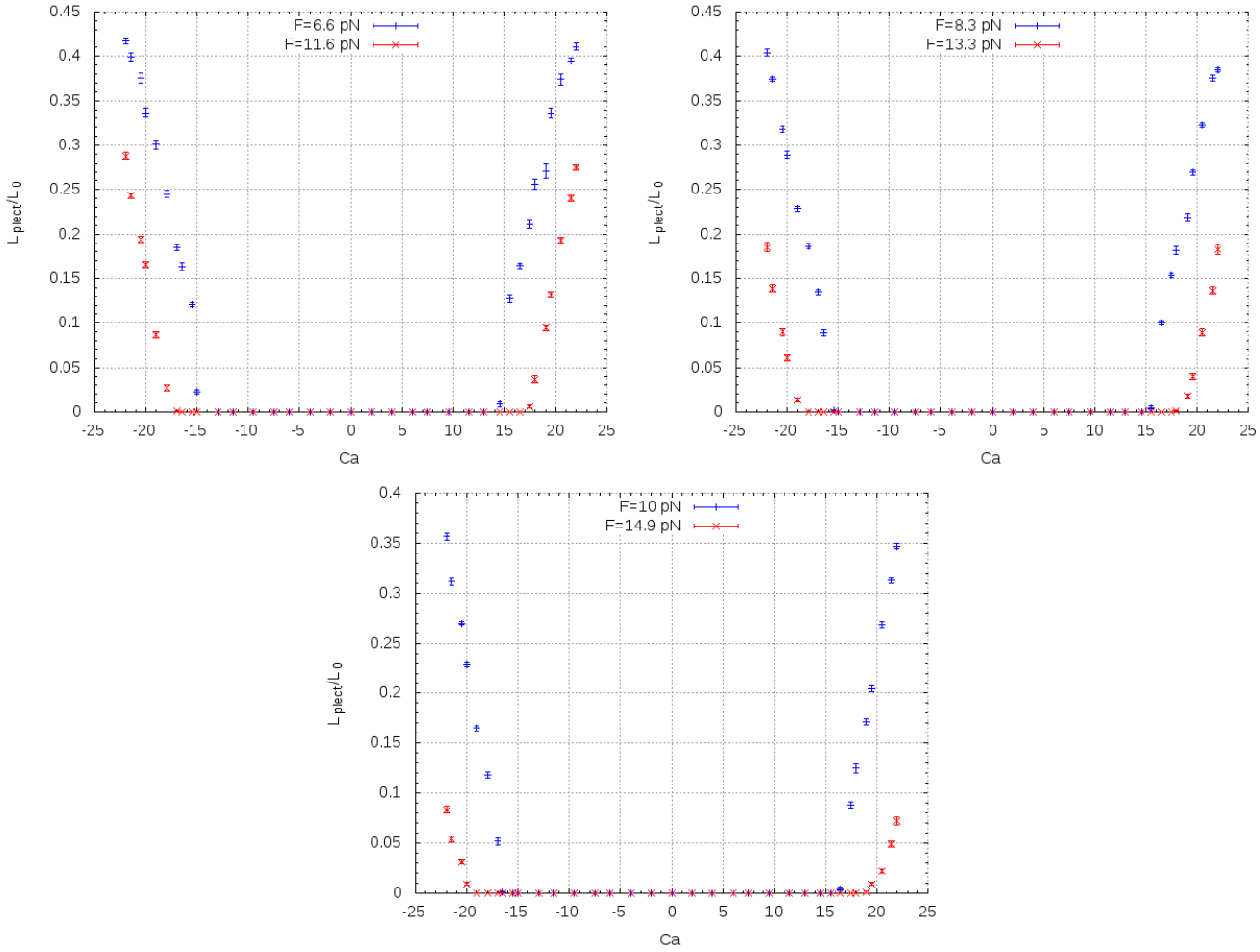

Figure 5.31: Normalized total length of plectonemic domains over Ca for $d = 0.48\,L_0$.

In Fig. 5.30 we observe that N_{plect} reaches a plateau when the pulling tension is $F = 6.6$ pN, 8.6 pN or 10.0 pN: for these values of F and Ca, the two strands prefer to form a single domain whose length grows while the catenation increases. Only by adding further twist, the system can nucleate new plectonemes. Instead this trend doesn't appear for $d = 0.024\,L_0$ and $d = 0.168\,L_0$, where the braid responds to the injected torque by giving rise to numerous plectonemic domains without achieving a constant value of N_{plect}.

5.4 Discussion of results

In light of the results reported in Sections 5.1 , 5.2 and 5.3 we can make the following considerations.

5.4.1 Comparison between the three intertether distances

Our study confirm previous works [6, 7, 20] : the buckling transition occurs later for greater forces F and Ca_c decreases with increasing intertether distances d (see Fig. 5.32).

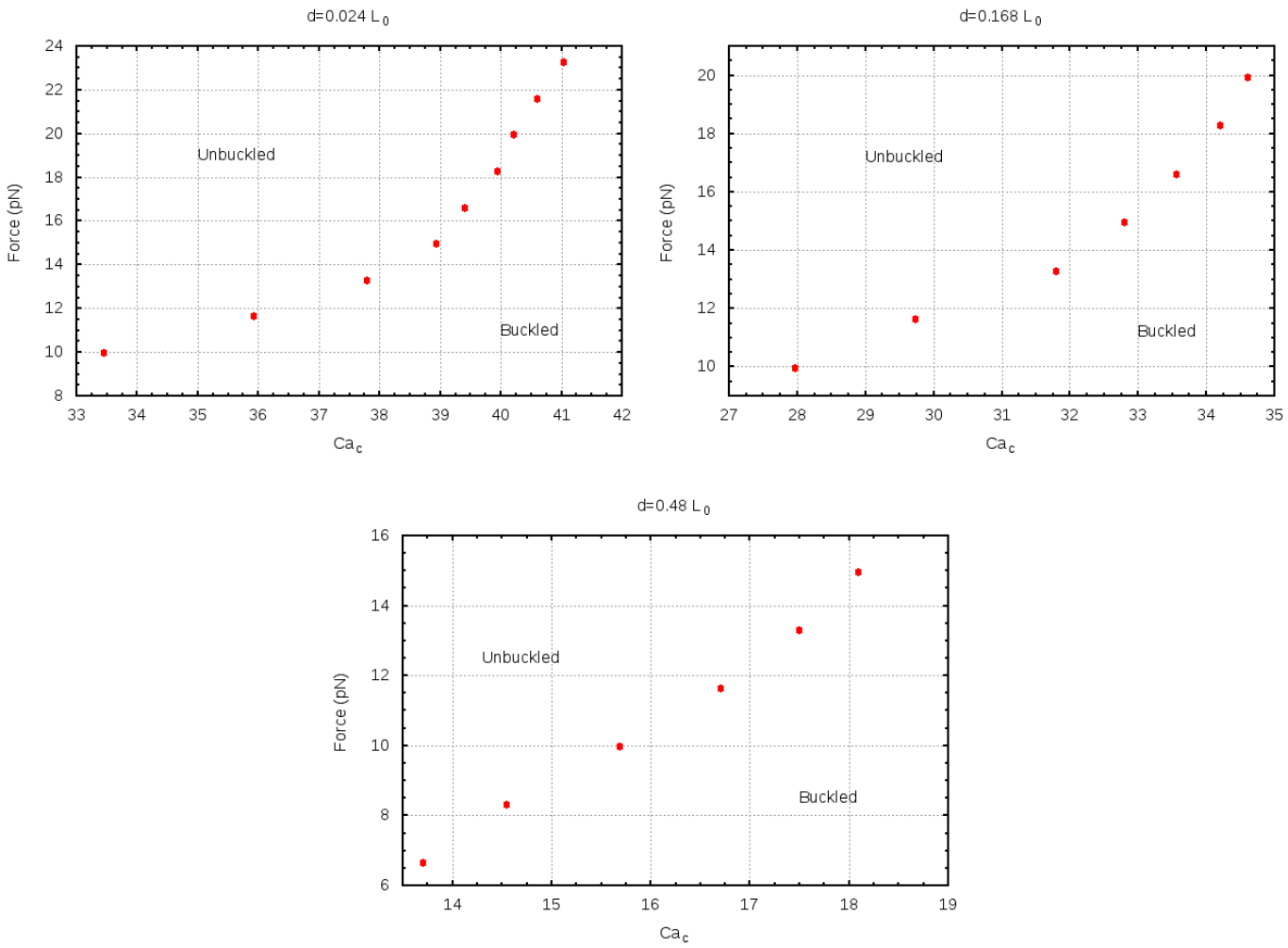

Figure 5.32: Summary graphic of the buckling transition for the three intertether distances d.

Results concerning the number and length of plectonemes cannot be completely compared to what has been already said by Brahamchari et al., because we don't include charges in our polymers.
However we can point out that at intermediate forces (e.g. $F = 11.6$ pN and $F = 13.3$ pN) and for a fixed Ca beyond the buckling point, the configurations with a larger d present greater values of N_{plect} and L_{plect}/L_0 than the case where the strands are closer (see Figs. 5.33 , 5.34). These results agree with previous works (see panel (c) and (d) of Fig. 3.2).

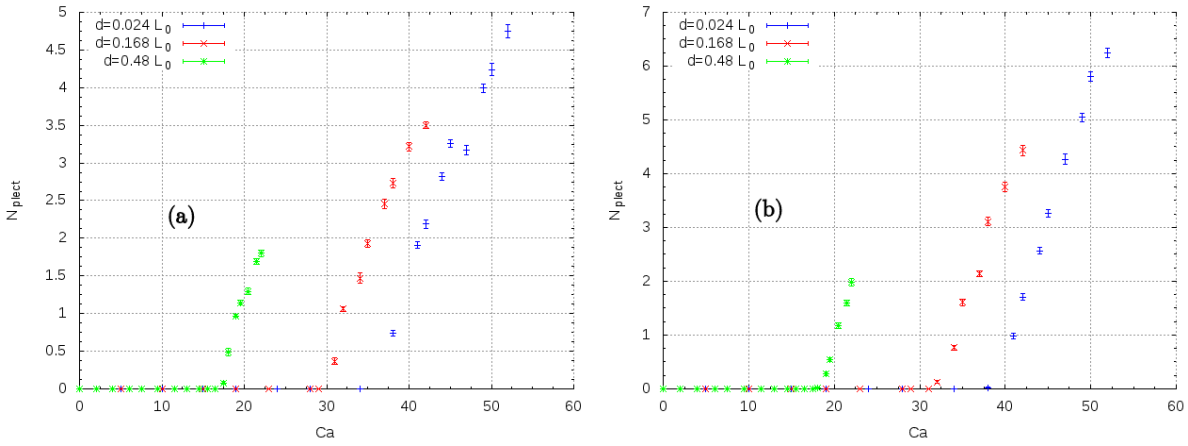

Figure 5.33: Number of plectonemes versus positive catenation for the three investigated intertether distances. **(a)**: N_{plect} over Ca for $F = 11.6$ pN. **(b)**: N_{plect} over Ca for $F = 13.3$ pN.

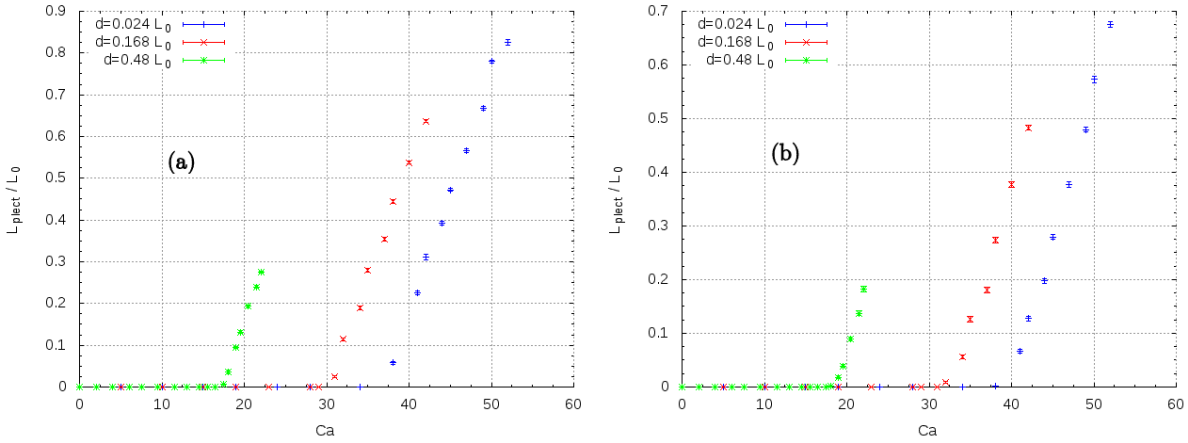

Figure 5.34: Normalized length of the plectonemic phase versus positive catenation for the three investigated intertether distances. **(a)**: L_{plect}/L_0 over Ca for $F = 11.6$ pN. **(b)**: L_{plect}/L_0 over Ca for $F = 13.3$ pN.

5.4.2 Branched plectonemes

When $d = 0.168c\,L_0$ and $F = 10.0$ pN, the normalized end-to-end distance saturates and the addition of catenation doesn't provoke an apparent reduction in the extension of the braid (see Fig. 5.35).

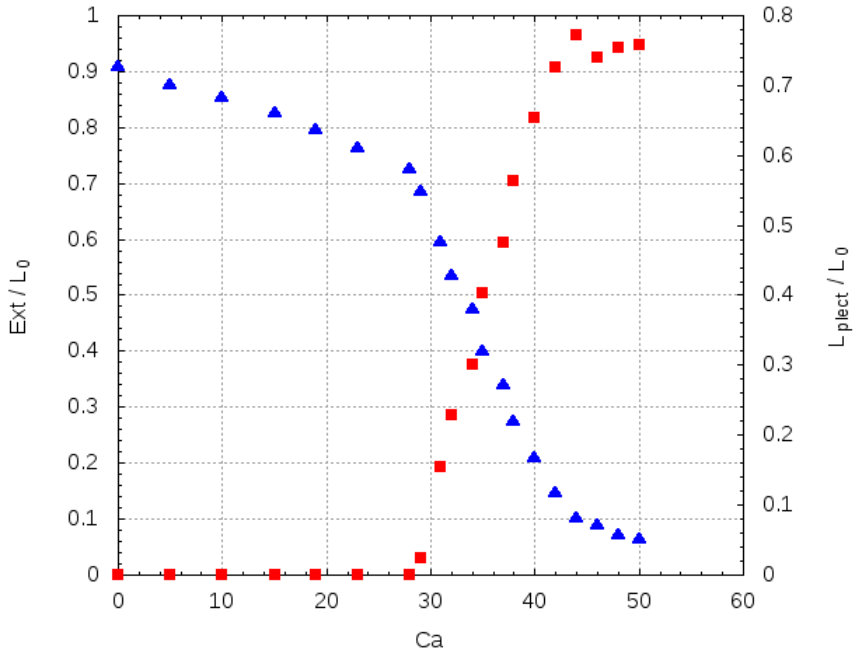

Figure 5.35: Saturation for $d = 0.168\,L_0$ and $F = 10.0$ pN. The blue triangles represent the normalized end-to-end distance (left y axis); the red squares are referred to the normalized total length of the plectonemic phase (right y axis).

The system has thus reached a critical value of Ext/L_0 and almost the total contour length has undergone the buckling transition. [5] This saturation is accompanied by a decrease in L_{plect}/L_0 (see Fig. 5.24): it seems that when the extension reaches a plateau, a part of the plectonemic domains returns to the braided phase dropping the total buckled length. The strangeness of this behavior suggests that maybe our method to define the number and the length of plectonemes is no longer reliable when the system is subject to a very strong torque. In fact, by checking the contact maps and the movies of these simulations, we discover that the braid starts to form a superhelix which doesn't correspond to a single plectoneme end-loop: so a single superhelix exhibits a fork where one finds the nucleation of two different plectonemes (see Figs. 5.36 , 5.37).

[5] It's important to keep in mind that there is always a part of the two strands which cannot participate to the braid because it forms the conjunctions between the anchoring points and the first (or last) crossing of the chains. The larger is the intertether distance d and the greater is the percentage of the contour length that doesn't take part to the braid.

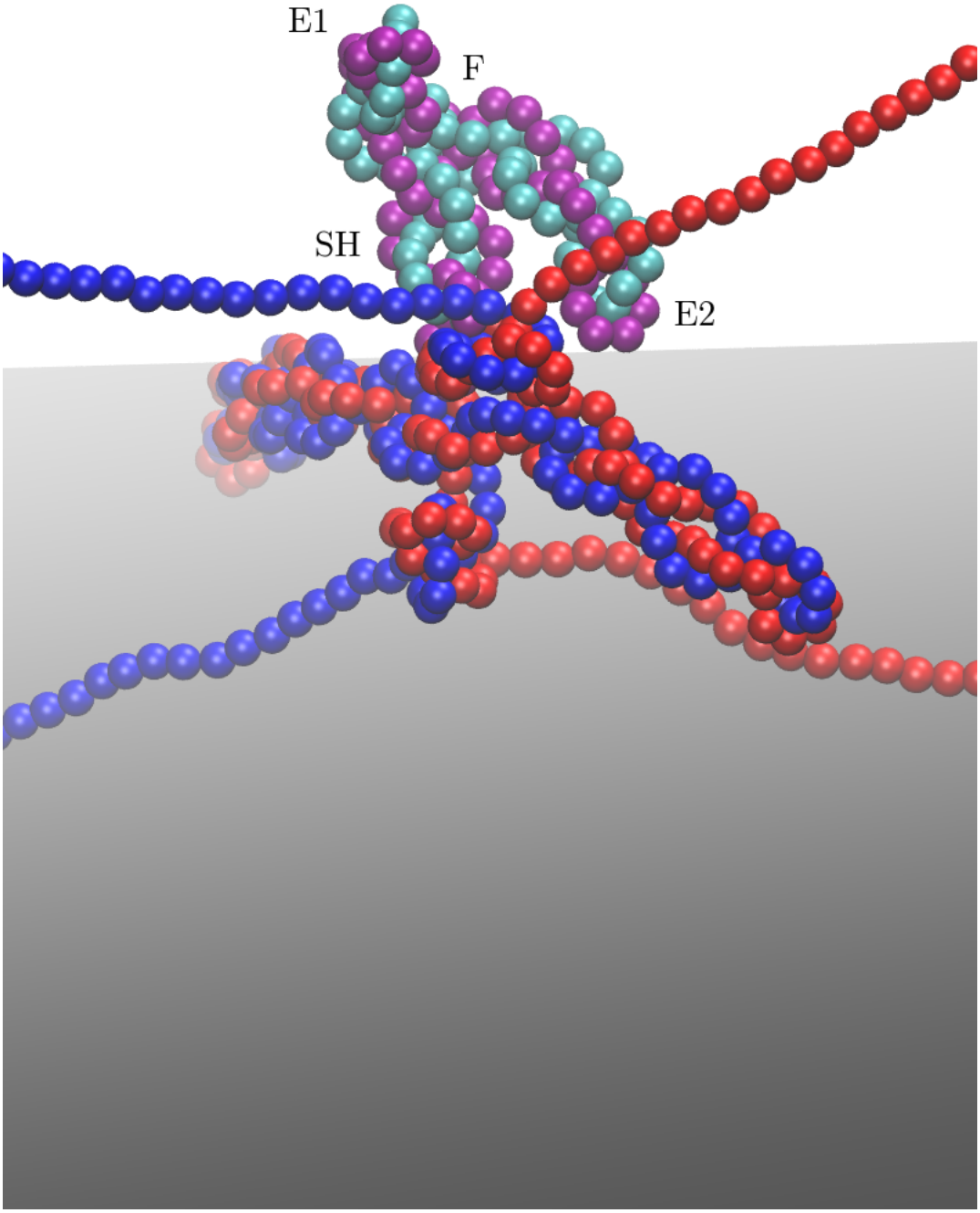

Figure 5.36: Snapshot from a simulation for $d = 0.168\,L_0$, $F = 10.0$ pN and $Ca = 46$. The beads involved in the superhelix diveded in two plectonemes are highlighted by different colours (violet and sea green).The initial superhelix is marked by the label *SH*; *E1* and *E2* are the two end-loops, while F is the fork.

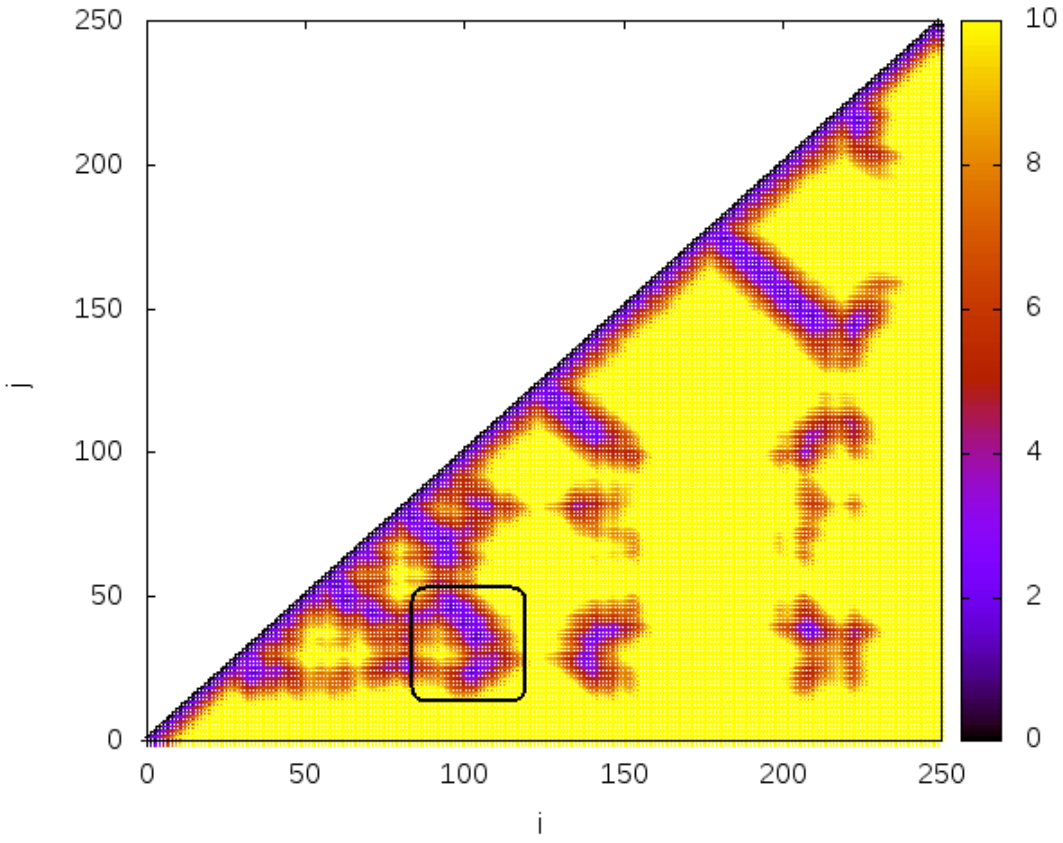

Figure 5.37: Contact map of the frame reported in Fig. 5.36. The area enclosed within the black rectangle corresponds to the initial superhelix labeled with *SH*.

The initial superhelix (labeled with *SH* in Fig. 5.36) appears as a blue-violet spot far from the diagonal (Fig. 5.37): our method explained in Section 5.1 doesn't count this area as a plectonemic region and therefore the total length of the plectonemic phase in Fig. 5.24 decreases. By increasing the catenation, the size of *SH* gets smaller and we can observe a new growth of L_{plect}/L_0.
Therefore the plectoneme reported in Fig. 5.36 reveals a branching: this conformational regime has already been predicted for DNA supercoils by Krajina and Spakowitz through MC simulations [25].

5.4.3 Solenoidal phase

Finally, the case $d = 0.024\,L_0$ shows a particular characteristic: the number and the length of plectonemic domains grow very slowly after the buckling transition if the pulling force is quite large ($F = 21.6$ pN and $F = 23.2$ pN). This is apparent in Figs. 5.38 and 5.39 where one can see the different behavior of N_{plect} and L_{plect}/L_0 depending on the tension.

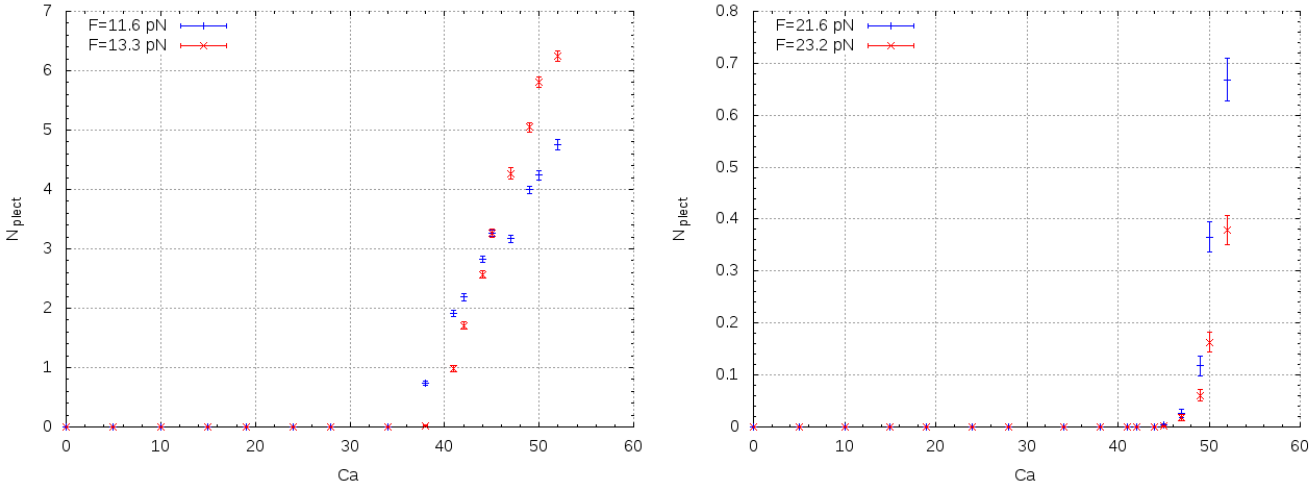

Figure 5.38: Number of plectonemes for two low tensions ($F = 11.6$ pN and $F = 13.3$ pN) and for two larger ones ($F = 21.6$ pN and $F = 23.2$ pN). Both panels are referred to the case $d = 0.024\,L_0$.

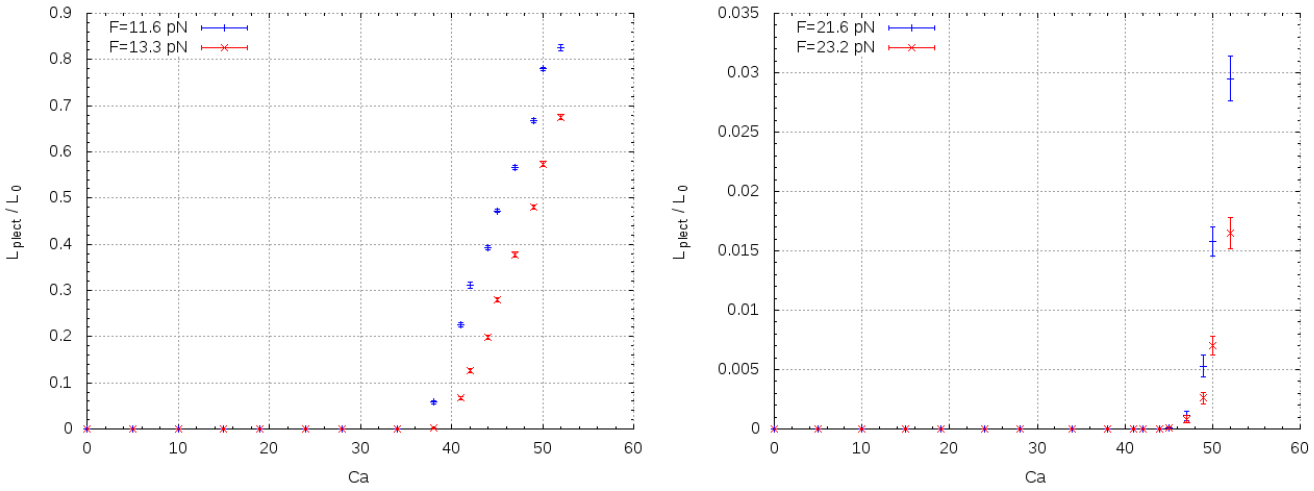

Figure 5.39: Normalized length of the plectonemic phase for two low tensions ($F = 11.6$ pN and $F = 13.3$ pN) and for two larger ones ($F = 21.6$ pN and $F = 23.2$ pN). In this two graphics the intertether distance is $d = 0.024\,L_0$.

In particular conditions, such as the ones just mentioned (little intertether distances d and high forces F), we note that the buckling transition doesn't coincide with the nucleation of the first end-loop: for example for $F = 21.6$ pN one has $Ca_c = 40.6$, but for catenation values slightly higher (i.e. $41 \lesssim Ca \lesssim 50$) the number of plectonemes is negligible (even lower than 0.5). By studying movies of our runs, we find that in similar situations the braid forms a structure where a strand starts to wrap around the other one forming a little, but visible, solenoid (see Fig. 5.40). Therefore it seems that, if d is small and F large enough, the buckling transition isn't due to a plectonemic nucleation, but to a solenoidal phase. By injecting further twist into the system, we can reach a plectonemic phase anyway, but the first end-loop doesn't form at $Ca = Ca_c$.
A solenoidal phase was observed on macroscopic filaments by Ghatak et al. [26], but it has never been mentioned for braiding. We still don't know if solenoids weren't observed in the previous works [7] and [20] because they didn't investigate such a high forces or because they included also electrostatic repulsions which could modify the structure of the braid. If this last point is correct (namely the Coulomb repulsion plays an important role on the buckling transition), we could however suppose that solenoidal structures form during braiding between strands immersed in a buffer with an high salt concentration where the Coulomb potential is negligible.
Lastly, we see that the writhe of the braid *follows* the buckling transition and its value grows for $Ca > Ca_c$ even if there isn't plectonemes nucleation. Anyway it's reasonable to think that also solenoids give a contribution to the computation of Wr_{braid} and therefore its increase after the buckling point is expected.

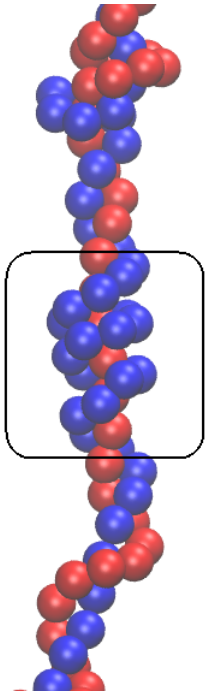

Figure 5.40: Example of solenoidal structure formed during a run with $F = 23.2$ pN, $Ca = 50$ and $d = 0.024\, L_0$.

Chapter 6

Equilibrium dynamics and statistics of plectonemes

In Chapter 5 we introduced contact maps as a tool through which recognize and count plectonemes. We can now address some questions about the behavior of plectonemic domains: how do they move along the braid? How does their number fluctuate at equilibrium for fixed Ca and F? Can two plectonemes merge forming a single domain? What can be said about their statistics (i.e. number, size, position, etc.)?
In the next two sections we'll try to answer all these points, first by focusing on the equilibrium dynamics of plectonemes and then on their statistics. The study will be carried out only for the case $d = 0.168\,L_0$ and we'll concentrate our efforts on four points of the phase diagram (Ca_c, F): two near the buckling transition, $A = (31, 11.6)$ and $B = (32, 13.3)$, and the other two deep in the buckling phase, $A^* = (31, 10.0)$ and $B^* = (32, 10.0)$ (see Fig. 6.1).

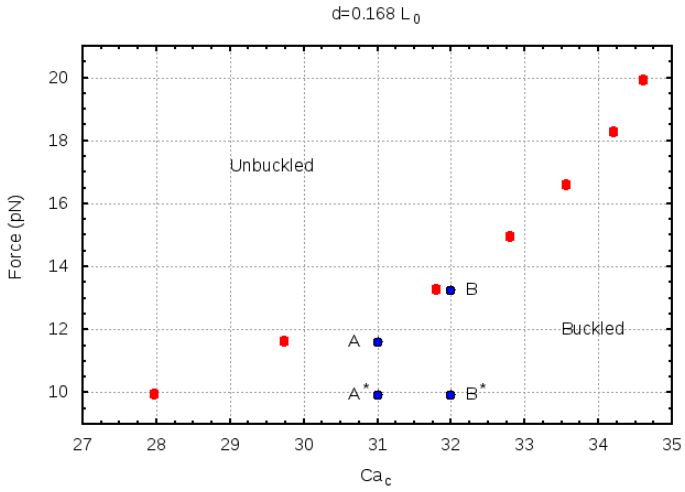

Figure 6.1: Phase diagram for the case $d = 0.168\,L_0$. In the next two sections we'll give an overview on the dynamics and statistics for the four points $A = (31, 11.6)$, $B = (32, 13.3)$, $A^* = (31, 10.0)$ and $B^* = (32, 10.0)$.

6.1 Plectonemes' dynamics

In the two works of Brahamachari et al., [7] and [20], the plectonemic transition has been extensively analyzed via a statistical-mechanical model (Chapter 3) that allows to investigate the dependence of the transition on the intertether distance d, the pulling force F and the ionic concentration. Nevertheless all these results concern the static of plectonemes, while their dynamics, as far as we know, has never been examined.
Our method of plectoneme detection gives us the possibility to follow the time evolution of plectonemes formed during braiding: in particular we can determine how many plectonemic domains there are as well as their positions along the braid. We'll analyze the equilibrium dynamics, namely we first allow the system to relax and then we monitor the plectonemes movements.

6.1.1 Dynamics close to the transition

The motion of plectonemes is studied through kymographs: in the x axis there is the time, while in the y axis we find the plectonemes position along the braid [1]. Following Chapter 5, we study plectonemes both of the blue and of the red strand (thanks to contact maps): if a frame of a simulation contains N_b blue domains and N_r red domains, we say that the number of plectonemes in this frame is equal to $min(N_b, N_r)$. For example, if at time $t = t^*$ one has $N_b \leq N_r$, the plectonemes are given by the blue strand: this means that the blue chain provides the number of domains, their length and also their position along the contour length. Otherwise, if $N_r > N_b$, these informations are derived from the red strand.
So in the kymographs that we'll show there are continuous *jumps* between blue and red plectonemes: if at time $t = t_1$ the plectonemes are given by the blue strand (because $N_b \leq N_r$), at the following time step, $t_2 > t_1$, they can be given by the red one (because $N_r > N_b$). One could think that this procedure is incorrect, since two corresponding blue and red domains (namely, two blue and red domains which form the same plectoneme of the braid) have different positions in relation to their own strand (see Fig. 6.2).
However, the shift between these positions is negligible and so we can study the dynamics of the braid's plectonemes by considering the blue or the red domains depending on whether $N_1 \leq N_2$ or $N_2 < N_1$.

[1] Along the ordinate we choose to set the normalized position, i.e. the position N divided by the number of atoms composing the single strand $N_0 = 250$. For the blue chain, N is simply the ID number reported in the LAMMPS *Input File* (see Appendix A), for the red one N is the ID number minus 250. So N moves between 1 and 250, since each strand is composed by 250 beads: the bead (blue or red) with position $N = 1$ corresponds to the first upper bead (the bead with the greater value of y in Fig. 4.1), while the one with $N = 250$ coincides with the atom held in fixed position on the bottom part of the flow cell. Therefore, if there are two plectonemes, one with the end-loop in position $N_1/N_0 = 0.2$ and the other with $N_2/N_0 = 0.6$, one can say that the first domain is closer to the upper fork where the two strands start to form the braid.

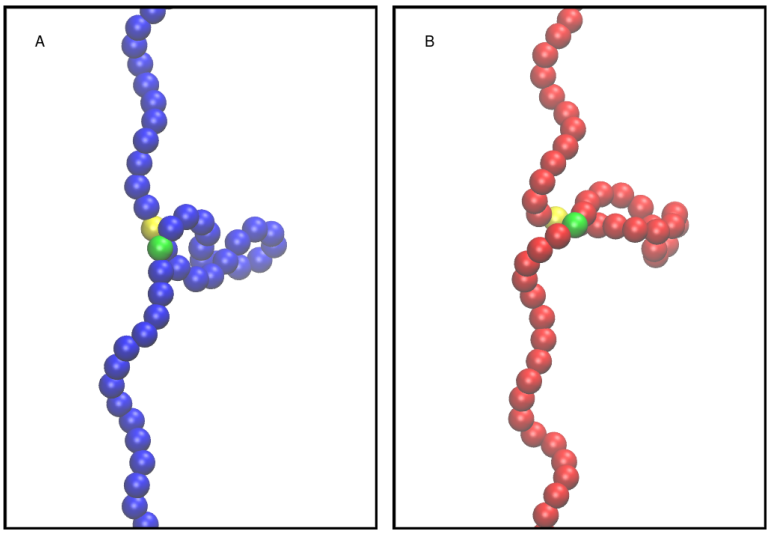

Figure 6.2: Blue and red plectonemes forming the same plectonemic domain of the braid for $F = 10.0$ pN and $Ca = 31$. In the two panels (A and B), we highlight the initial and the final beads of the domains with the yellow and green colors respectively. In panel (A) the yellow bead corresponds to $N_{(A,y)} = 159$, while the green one to $N_{(A,g)} = 178$. In panel (B) the two atoms have positions $N_{(B,y)} = 151$ and $N_{(B,g)} = 170$. Therefore the shift between the positions is equal to $N_{(A,y)} - N_{(B,y)} = N_{(A,g)} - N_{(B,g)} = 8$. This value is quite low if compared to the total number of beads (250): this means that we can consider the blue or the red plectonemes without committing important errors in the position of the braid's plectonemes.

First of all we analyze the dynamics near the buckling transition, i.e. for points $A = (31, 11.6)$ and $B = (32, 13.3)$.
A kymograph for the point A is reported in the top panel of Fig. 6.3, while in the bottom panel it's possible to observe a zoom for a time t such that $30000\,\tau \leqslant t \leqslant 70000\,\tau$ [2].
The yellow points coincide with the parts of the chains enclosed in a plectoneme, whose extremities [3] are marked with red points. These yellow bars are referred to the left y axis, where we find the normalized position N/N_0.
On the other hand, the dotted blue line shows the time evolution of the normalized end-to-end distance Ext/L_0 and its values can be found in the right y axis.
The graphic contains two additional horizontal green lines that indicate the mean position of the upper and lower fork (see panel A of Fig. 4.1): these averages are calculated by moving between uncorrelated frames of the trajectory represented in each kymograph. After a period of equilibration (the blue line drops abruptly in the first part of the simulation) [4], we observe the formation of numerous short-lived plectonemes.

[2] In our kymographs the time is expressed in Lennard-Jones units τ; in Appendix B we explain the conversion between τ and seconds.

[3] The extremities coincide with the initial and final bead of a domain, e.g. the yellow and green atoms in Fig. 6.2.

[4] The initial drop of the end-to-end distance is due to the starting configuration of the braid. In fact the input configuration, with fixed Ca, has been obtained through the *varying catenation* setup, where we use a very strong pulling force F. Then in these runs we allow the system to relax fixing a lower tension F^* and keeping a constant Ca value: so the Ext decreases abruptly reaching a plateau depending on F^*.

The *Ext* fluctuates and sometimes it is affected by the nucleation of plectonemic domains: this is apparent at time $t = t^*$, when the formation of a plectoneme implies a decrease in the braid extension.
It's also interesting to note how plectonemes are constrained within the two forks: their centers of mass (i.e. their end-loops) are always enclosed in this region and the initial or the final part of a domain (namely the yellow points close to the red ones) seldom exceed the green lines.

Figure 6.3: Kymograph for $F = 11.6$ pN and $Ca = 31$ (top panel) and a zoom (bottom panel). Yellow bars indicate plectonemes and they are referred to the normalized position N/N_0 (left y axis); the dotted blue line represents the normalized braid extension Ext/L_0 and its values are reported in the right y axis. The horizontal green lines highlight the average positions of the upper and lower fork.

In Fig. 6.4 we show other two kymographs for point A. Again one observes the presence of a *gas* of small plectonemes: several plectonemic domains are created and destroyed, but they aren't able to form stable structures.

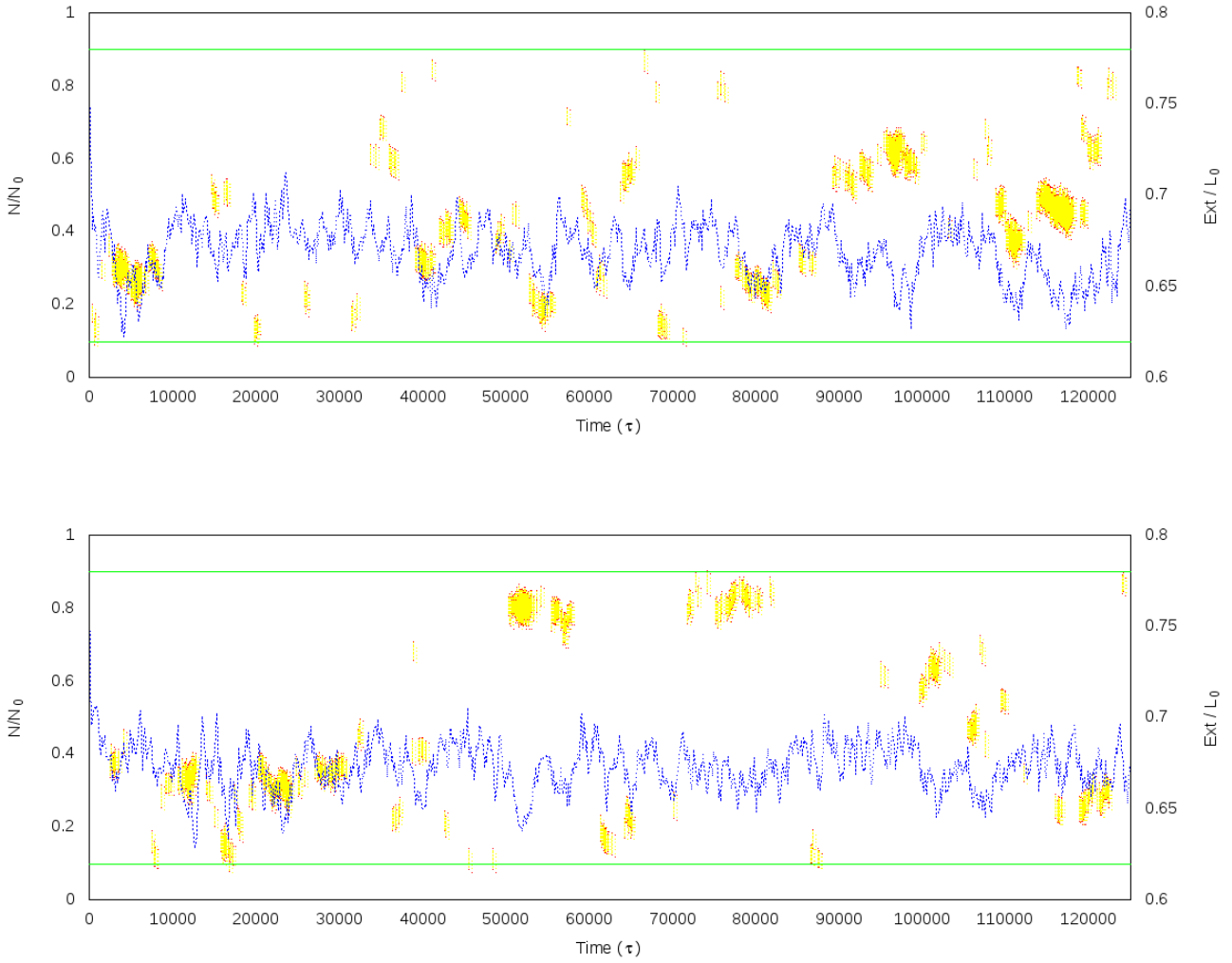

Figure 6.4: Two different kymographs for $F = 11.6$ pN and $Ca = 31$. On the left y axis one finds the normalized position, while on the right one there are the values of the normalized end-to-end distance.

A similar study can be performed for $B = (32, 13.3)$. In Fig. 6.1 one sees that this point is closer to the transition line than point A: therefore we expect to find fewer plectonemes, since in Fig. 5.23 we observe that N_{plect} is lower when one is nearer the critical catenation.
Fig. 6.5 shows a kymograph (and a zoom) for B. As in the previous case, the extension Ext is weakly influenced by the presence of plectonemes, such as at time $t = t^*$.

Figure 6.5: Kymograph for $F = 13.3$ pN and $Ca = 32$ (top panel) and a zoom (bottom panel). The left y axis shows the normalized positions of plectonemes; the right y axis refers to the normalized end-to-end distance (dotted blue line).

In Fig. 6.6 we report two additional kymographs for the same values of F and Ca ($F = 13.3$ pN and $Ca = 32$). It's interesting to note how these domains seem to have a smaller lifetime than the ones seen for point A (Figs. 6.3 and 6.4): the proximity to the buckling transition doesn't affect only the number of plectonemes, but also their survival time.

Figure 6.6: Two different kymographs for $F = 13.3$ pN and $Ca = 32$.

From the examination of these two cases (A and B) we have obtained that just past the buckling transition [5] one observes the formation of a plectonemic *gas*: numerous small domains form, but they are short-lived and cannot merge forming a larger plectoneme.

[5] We are dealing the situation in which the buckling transition coincides with the plectonemic one, since in Section 5.2 we saw that for $Ca \gtrsim Ca_c$ and $F = 11.6, 13.3$ pN there is the nucleation of plectonemes.

6.1.2 Dynamics deep in the buckling phase

We now focus on points $A^* = (31, 10.0)$ and $B^* = (32, 10.0)$ that are well inside the plectonemic phase.
From Chapter 5 we know that, going deeper into the buckling phase by keeping the pulling force fixed, the number of plectonemes N_{plect} and their total length L_{plect} increase: so one could think that in point B^* more and larger plectonemes will be observed than in point A^*.

Taking into consideration $A^* = (31, 10.0)$ one gets kymographs as the one in Fig. 6.7.

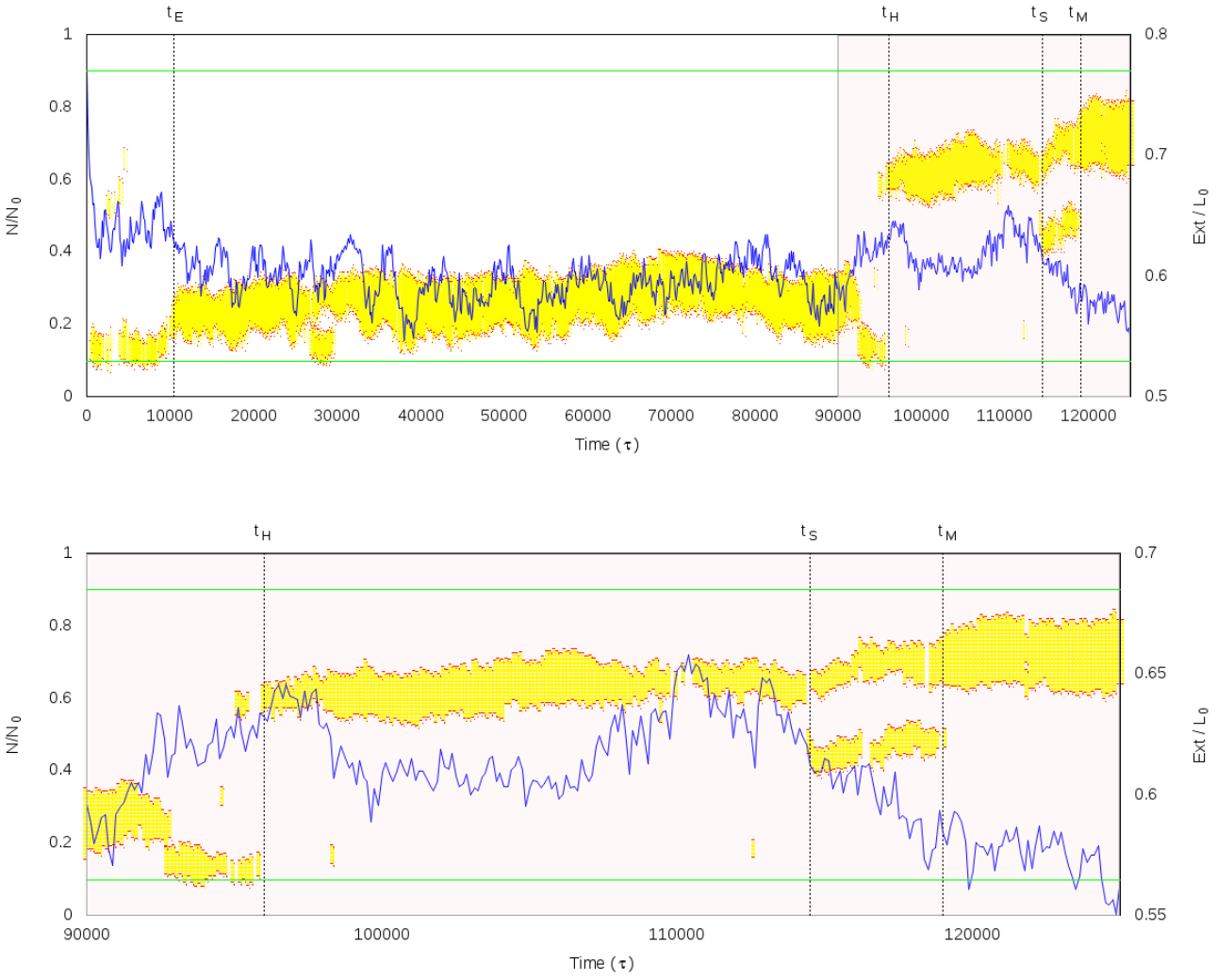

Figure 6.7: Kymograph for $F = 10.0$ pN and $Ca = 31$ (top panel) and a zoom (bottom panel). The solid blue line corresponds to the time evolution of the end-to-end extension and its values are in the right y axis.

Several considerations can be made about this dynamics:

- after an initial drop due to relaxation, the ratio Ext/L_0 reaches a plateau approximately at time $t = t_E$. From this moment and before $t = t_H$, we find a long-lived plectoneme, which rarely branches into multiple domains. This plectoneme stays close to the upper fork of the braid;

- at $t = t_H$ an *hopping* event occurs: just before $t = t_H$, the plectoneme disappears from its original position and at time t_H reappears in another point, where $N/N_0 \sim 0.6$.
  Note that this kind of hopping mechanism was observed experimentally for supercoiled DNA [27]. The authors observed that the energetics of this event is correlated to the nucleation cost of a new loop and to the rotation of the intermediate DNA (see Fig. 6.8). Non local mechanism of motion allow the fast movement of plectonemes along the contour length (they found a maximum hopping distance of $\sim 5\mu m$ in a time range < 20 ms);

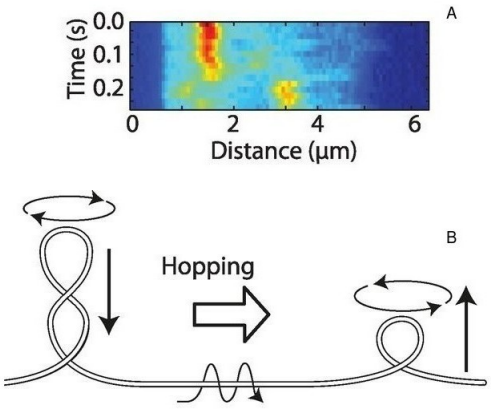

Figure 6.8: Hopping mechanism in supercoiled DNA. (A): experimental kymograph of an hopping event. (B): the formation of a plectoneme in a new far site is correlated to the energy cost of the nucleation of a new loop and to the transfer of writhe, namely to the rotation of the intermediate DNA. Figure from Leonhout et al. [27].

- at $t = t_S$ the plectoneme separates into two shorter domains, that merge later at time t_M by forming a single loop whose size increases with time. For $t > t_M$ the normalized extension Ext/L_0 is evidently affected by this growth, in fact its value lowers.

Other two trajectories for point A^* are shown in the kymographs of Fig.6.9, where one can see behaviors similar to the ones explained for Fig. 6.7.

Figure 6.9: Kymographs for two different trajectories simulated at $F = 10.0$ pN and $Ca = 31$.

Finally let us examine point B^*, i.e. the case $F = 10.0$ pN and $Ca = 32$.
From the data of Chapter 5 we know that between A^* and B^* the number of plectonemes increases by 28%, while the total length of the plectonemic phase by 49%: therefore one expects to observe more frequently bigger plectonemic domains rather than two or three small ones.
Fig. 6.10 suggests that this is indeed the case: after the equilibration, a large plectoneme forms and stays in the same position until, at $t \sim t_S$, it splits into two smaller ones. At t_M they merge again forming a single plectoneme which survives until the end of the simulation. Note that this splitting and rejoining mechanism results into an effective spatial displacement of the original plectoneme.

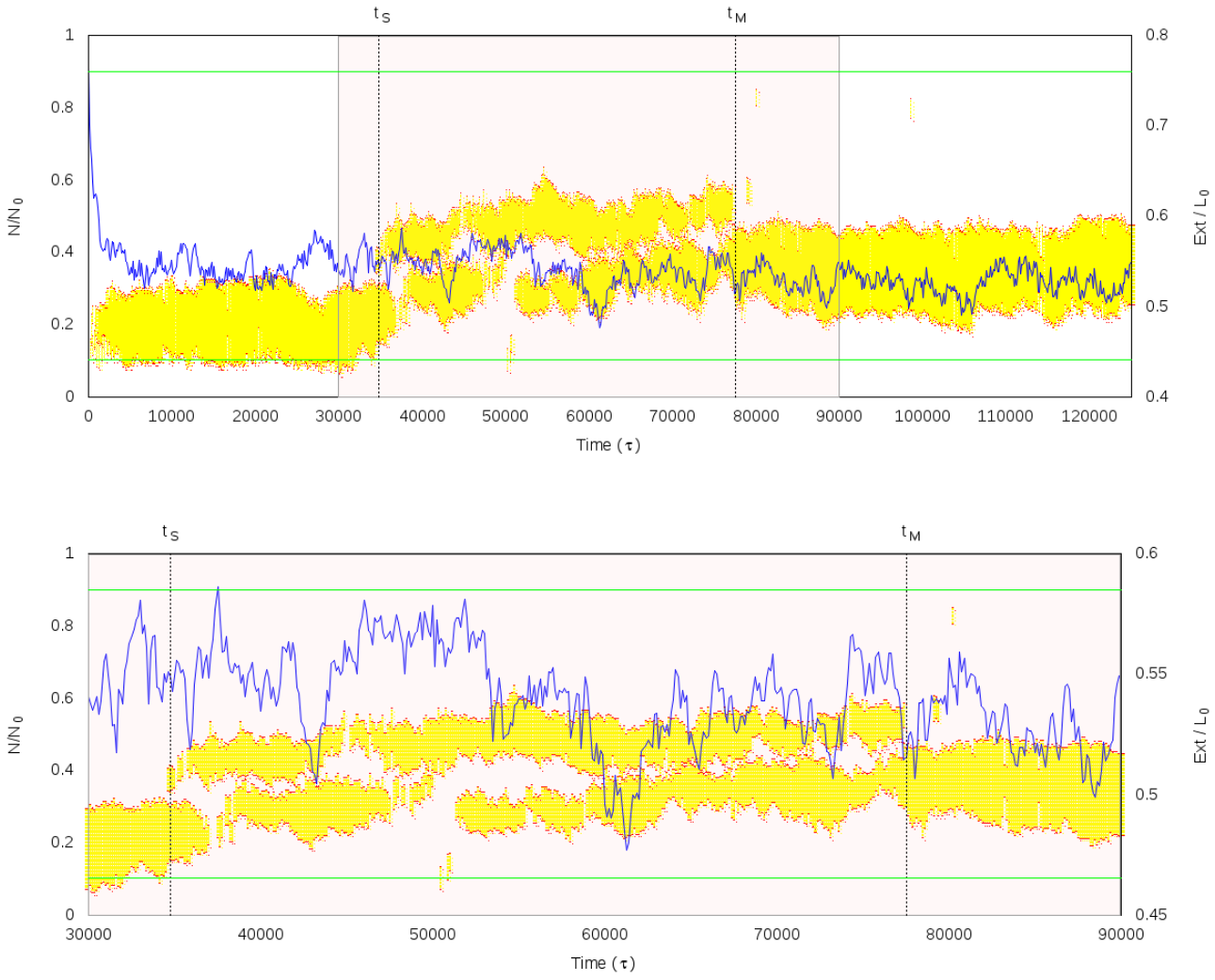

Figure 6.10: Kymograph for $F = 10.0$ pN and $Ca = 32$ (upper panel) and a zoom (bottom panel).

In Fig. 6.11 we show two further trajectories for point B^*. In both these two cases, the single large plectoneme is rather stable during the simulation.

Figure 6.11: Kymographs for $F = 10.0$ pN and $Ca = 32$.

Comparing all the previous figures (for A, B, A^* and B^*) one notes that the fluctuations of the extension are similar. From the zooms of Figs. 6.3, 6.5, 6.7 and 6.10 it's possible to observe that they are slightly higher when we are in the deep buckling phase (points A^* and B^*): however the distance or the proximity to the buckling transition don't seem to affect the oscillations around the equilibrium throughly.

6.2 Statistics of plectonemic domains

In this section we'll introduce the statistics of plectonemes at equilibrium. As far as we know, the only statistical study has been performed by Brahamachari et al. [7], who investigated the distribution of the braid extension experimentally, succeeding in recognizing the nucleation of different domains (see Figs. 6.12 and 6.13).

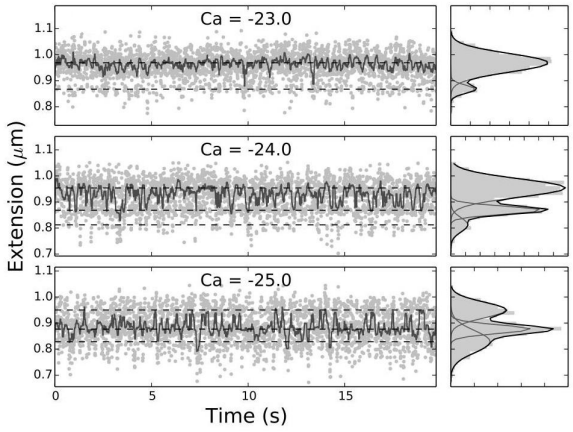

Figure 6.12: Experimental time evolution of the braid extension for two 6 kb DNAs under a pulling force of 0.8 pN and immersed in 100 mM NaCl. The panels show three catenation values near the buckling transition: on the right it's possible to observe the corresponding frequency histograms, which are fit to a sum of Gaussian distributions. Figure from Brahamachari et al. [7].

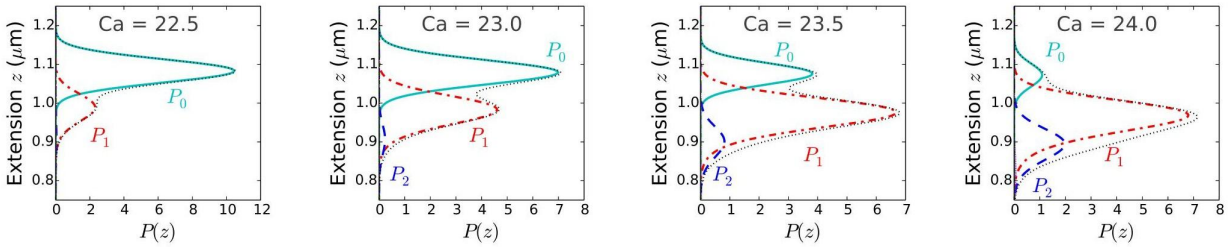

Figure 6.13: Theoretical histograms of the end-to-end distance for four catenations near the buckling transition. The probability distributions were calculated via the statistical-mechanical model reported in [20]. P_0, P_1 and P_2 are the probabilities correlated to the presence of 0,1 or 2 plectonemes respectively. Increasing the catenation one finds the nucleation of multiple plectonemic domains. Figure from Brahamachari et al. [7].

Thanks to our simulations we can extract the behavior of the extension Ext as a function of the number of plectonemes N_{plect}; however we are also able to know what is the trend of the total plectonemic length and of the size of the single plectoneme depending on N_{plect}. Another interesting feature which will be studied is the position of the center of mass of each plectoneme [6].

[6]The center of mass of a plectoneme coincides with the position of its end-loop: if the initial and the final beads of a domain have position N_i and N_f, its center of mass is given by $\frac{N_i+N_f}{2}$.

As in the previous section, we'll focus on points A, B, A^* and B^* of Fig. 6.1. For each point we have simulated 200 trajectories. To perform an unbiased estimate, we take only configurations well separated in time to be considered uncorrelated (see footnote *1* of Chapter 5).

6.2.1 Histograms of the end-to-end distance

Let us start with the statistics of the normalized end-to-end distance Ext/L_0. In Figs. 6.14, 6.15, 6.16 and 6.17 we show Ext/L_0 as a function of the number of plectonemes and on the right panels we set the related histograms. The bin size is equal to 0.004 which is the relative size of a bead (i.e. $\frac{\sigma}{L_0} = \frac{\sigma}{250\sigma} = 0.004$); moreover, we plot the normalized frequency, namely we divide the frequency in each bin by the total number of data.

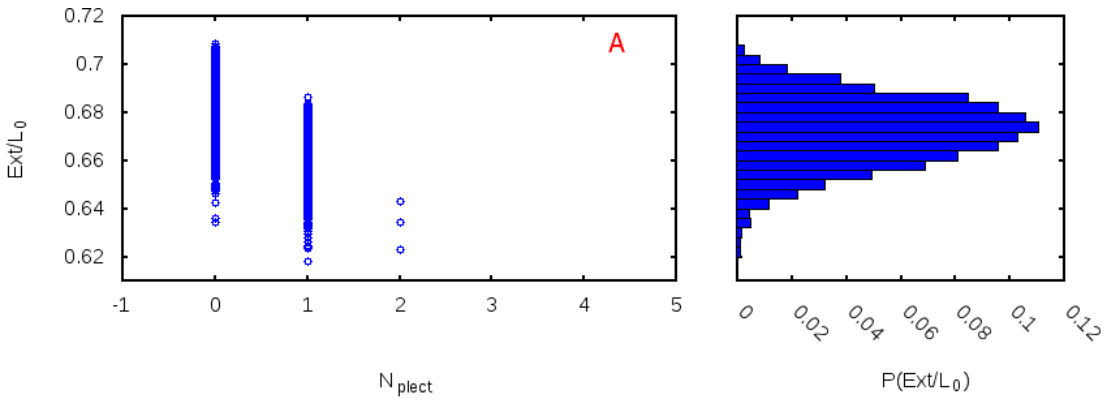

Figure 6.14: Left panel: ratio Ext/L_0 as a function of the number of plectonemes for point A ($F = 11.6$ pN and $Ca = 31$). Right panel: normalized frequency histogram of the extensions reported on the left.

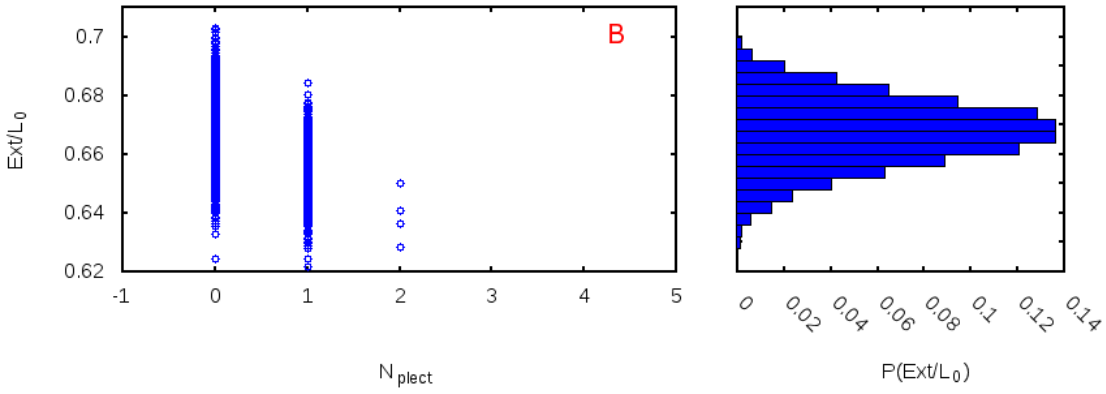

Figure 6.15: Left panel: end-to-end distance over plectonemes number for point B ($F = 13.3$ pN and $Ca = 32$). Right panel: normalized frequency histogram of the extensions reported on the left.

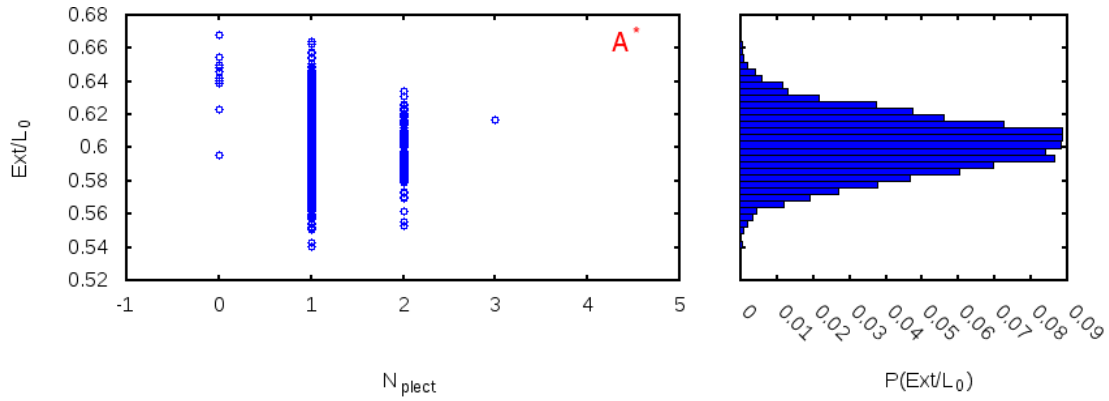

Figure 6.16: End-to-end distance over N_{plect} (left panel) and the corresponding histogram (right panel) for point A^* ($F = 10.0$ pN and $Ca = 31$).

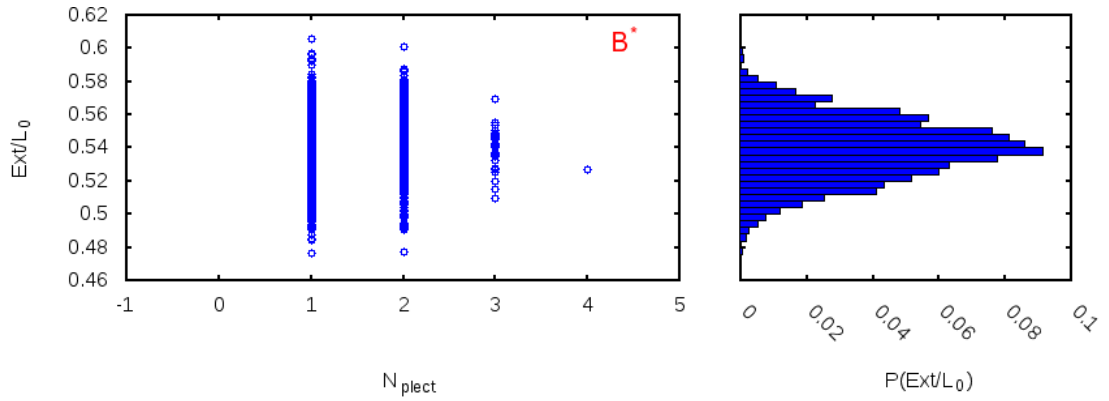

Figure 6.17: End-to-end distance over N_{plect} (left panel) and the corresponding histogram (right panel) for point B^* ($F = 10.0$ pN and $Ca = 32$).

The data included in the previous graphics are summarized in Table 6.1 which contains the mean normalized extensions $\widehat{Ext}$ for A, B, A^* and B^*, depending on the number of plectonemes. Let us indicate the mean normalized extension for a point P [7] and $N_{plect} = N$ with the symbol $\widehat{Ext}^{(P,N)}$.
In Figs. 6.14 and 6.15 there is an apparent shift between extension values for $N_{plect} = 0$ and $N_{plect} = 1$, since the nucleation of an end-loop reduces the end-to-end distance. From Table 6.1 we note that the formation of the first domain provokes an $\widehat{Ext}$ reduction equal to 0.02 for point A ($\widehat{Ext}^{(A,0)} - \widehat{Ext}^{(A,1)} \simeq 0.02$) and to 0.01 for point B ($\widehat{Ext}^{(B,0)} - \widehat{Ext}^{(B,1)} \simeq 0.01$).
Nevertheless in Figs. 6.16 and 6.17 we cannot recognize different peaks related to the nucleation of multiple domains (as Brahamachari et al. made in Fig. 6.13). Looking at the following table, we see that $\widehat{Ext}^{(A^*,1)} - \widehat{Ext}^{(A^*,2)} \simeq 0.001$ and $\widehat{Ext}^{(B^*,1)} - \widehat{Ext}^{(B^*,2)} \simeq 0.005$: these differences are up to 10 times smaller than the decreases brought by the growth of the first plectoneme.

[7] P can be A, B, A^*, B^*

(Ca, F)	N^o of plectonemes	N^o of data	$\widehat{Ext}$
$A = (31, 11.6)$	0	2258	0.6778 ± 0.0002
	1	1044	0.6592 ± 0.0003
	2	3	0.6334 ± 0.0059
$B = (32, 13.3)$	0	4171	0.6696 ± 0.0002
	1	690	0.6553 ± 0.0004
	2	4	0.6389 ± 0.0046
$A^* = (31, 10.0)$	0	11	0.6413 ± 0.0056
	1	3036	0.6017 ± 0.0003
	2	159	0.6003 ± 0.0012
	3	1	0.6166
$B^* = (32, 10.0)$	1	2091	0.5378 ± 0.0004
	2	860	0.5433 ± 0.0006
	3	35	0.5310 ± 0.0020
	4	1	0.5272

Table 6.1: Values of the mean normalized extension depending on (Ca, F) and on the number of plectonemes.

The discrepancy between our results and the ones seen in Figs. 6.12 and 6.13 could be due to the absence of charges in our chains: in fact, in works [7] and [20], the charged DNA strands form numerous and short plectonemes, therefore the nucleation of a new end-loop provokes a shortening in the end-to-end extension. Instead our plectonemes can grow in size getting deeper into the buckling phase, and so, even if a domain splits into two different plectonemes during a run, the total plectonemic length stays constant and this event doesn't affect the braid extension.

6.2.2 Statistics of the total plectonemic length

We now consider the behavior of the total length of the plectonemic phase L_{plect} as a function of the number of plectonemes N_{plect}. Figs. 6.18, 6.19, 6.20 and 6.21 show how L_{plect}/L_0 changes depending on N_{plect} and in the right panels we report the corresponding normalized histograms.
Table 6.2 contains all the results dividing them according to the point of the phase diagram (A, B, A^* and B^*) and to N_{plect}: with $\widehat{L_{plect}}$ we refer to the average of the normalized total plectonemic length and, if we have to indicate a particular configuration (point P of the phase diagram and $N_{plect} = N$), we use the symbol $\widehat{L}_{plect}^{(P,N)}$.

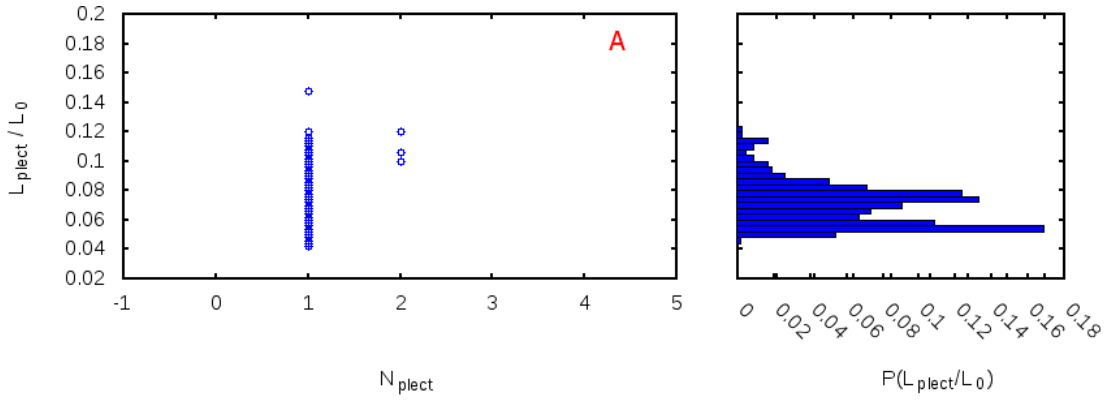

Figure 6.18: Normalized total plectonemic length over N_{plect} (left panel) and the corresponding histogram (right panel) for point A ($F = 11.6$ pN and $Ca = 31$).

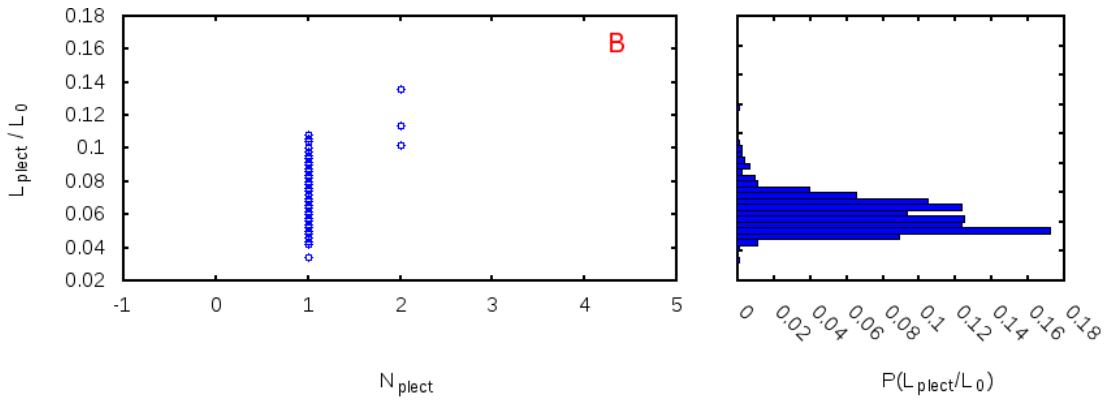

Figure 6.19: Normalized total plectonemic length versus N_{plect} (left panel) and its histogram (right panel) for point B ($F = 13.3$ pN and $Ca = 32$).

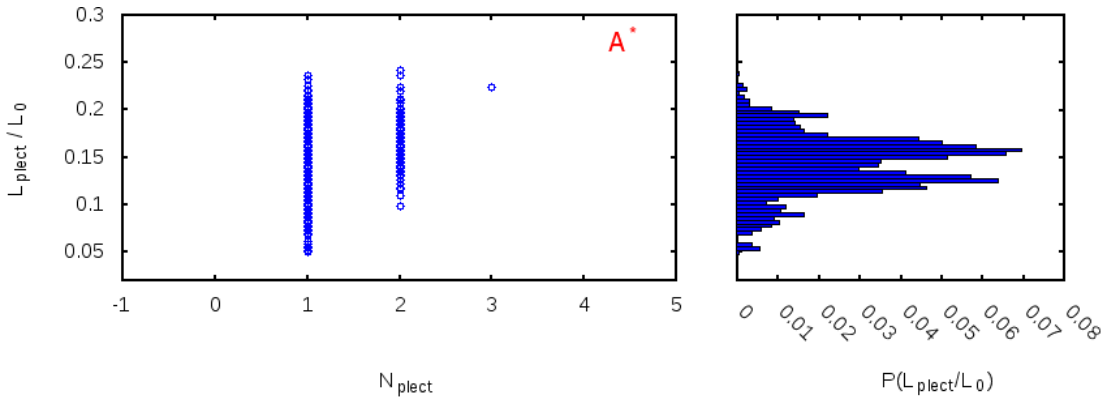

Figure 6.20: L_{plect}/L_0 over N_{plect} (left panel) and its histogram (right panel) for point A^* ($F = 10.0$ pN and $Ca = 31$).

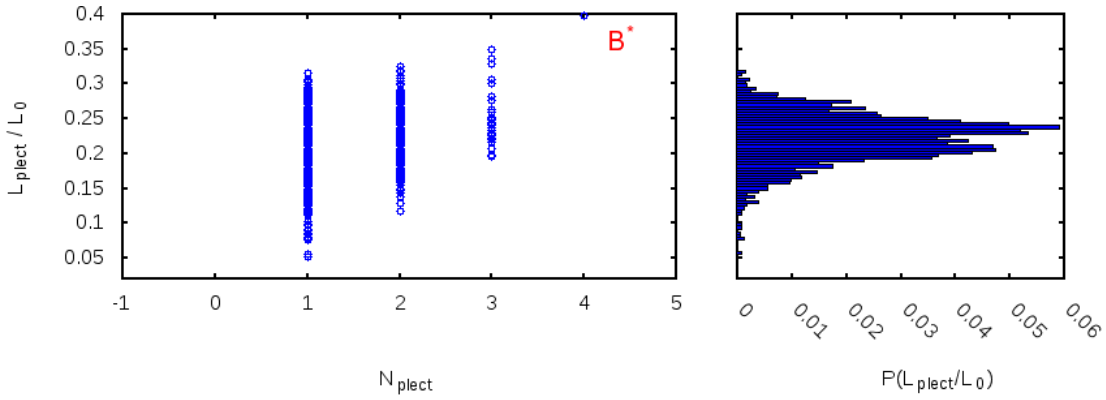

Figure 6.21: L_{plect} versus N_{plect} (left panel) and the corresponding histogram (right panel) for point B^* ($F = 10.0$ pN and $Ca = 32$).

(Ca, F)	N^o of plectonemes	N^o of data	$\widehat{L_{plect}}$
$A = (31, 11.6)$	1	1044	0.0693 ± 0.0005
	2	3	0.1087 ± 0.0059
$B = (32, 13.3)$	1	690	0.0634 ± 0.0004
	2	4	0.1135 ± 0.0080
$A^* = (31, 10.0)$	1	3036	0.1411 ± 0.0005
	2	159	0.1625 ± 0.0021
	3	1	0.2240
$B^* = (32, 10.0)$	1	2091	0.2182 ± 0.0008
	2	860	0.2255 ± 0.0011
	3	35	0.2517 ± 0.0064
	4	1	0.3980

Table 6.2: Values of the average of the normalized total plectonemic length depending on (Ca, F) and on the number of plectonemes.

Dealing only with cases with a better statistics (points A^* and B^*) we note that $\widehat{L}_{plect}^{(A^*,2)} - \widehat{L}_{plect}^{(A^*,1)} \simeq 0.02$ and for point B^* one has $\widehat{L}_{plect}^{(B^*,2)} - \widehat{L}_{plect}^{(B^*,1)} \simeq 0.007$ that is of the same order of magnitude of the errors reported in Table 6.2.
We remind that the smallest plectoneme contains 13 beads, so it's reasonable to think that the growth of the second domain would provoke an increase in $\widehat{L}_{plect}$ equal to 0.05 ($13 \cdot 0.004 \simeq 0.05$) at least: nevertheless both above values are lower than it. This confirms the idea that, in our setup, the size of a plectoneme can grow and so, even if an end-loop splits into two domains, the length of the total plectonemic phase stays almost constant. Therefore the nucleation of new domains is not necessarily related to an evident increase of the total plectonemic length.

6.2.3 Statistics of a single plectonemic domain

In this subsection we introduce the study of a single plectonemic domain.
We have always focused on the total plectonemic length so far, while now the normalized length of a single plectoneme L_{sp}/L_0 will be considered: the statistics will be obtained from the same runs used in the previous analysis, so we report results concerning the four points A, B, A^*, B^* of the phase diagram 6.1.
The average normalized length of a single plectoneme is indicated with $\widehat{L}_{sp}$ and, if we are referring to a particular configuration (point P and $N_{plect} = N$), we use $\widehat{L}_{sp}^{(P,N)}$.
Figs. 6.22, 6.23, 6.24 and 6.25 show the length of a plectoneme as a function of N_{plec}; on the right one finds the related normalized histograms.

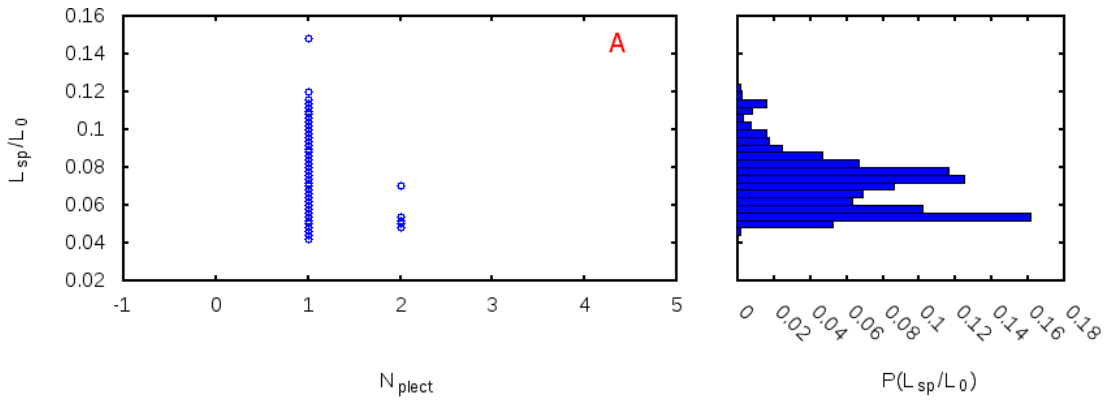

Figure 6.22: Length of a single plectoneme over N_{plect} for $F = 11.6$ pN and $Ca = 31$ (on the left) and the corresponding histogram (on the right).

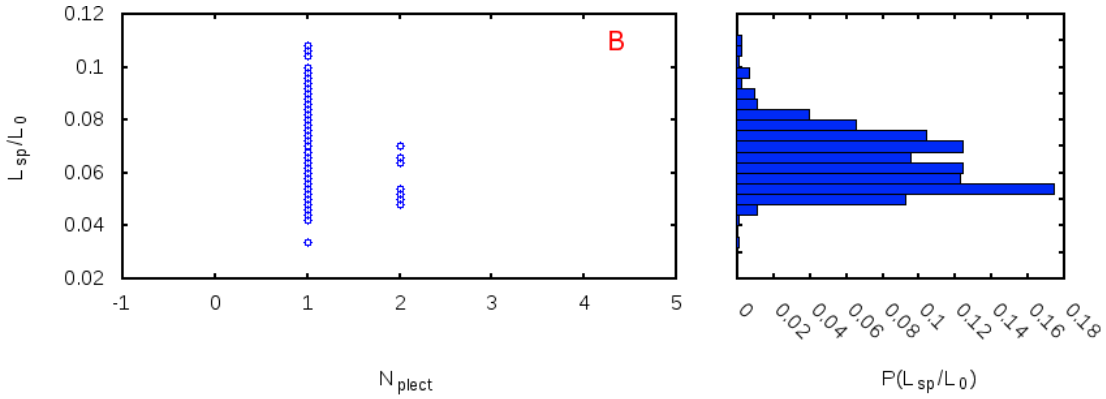

Figure 6.23: Length of a single plectoneme over N_{plect} for $F = 13.3$ pN and $Ca = 32$ (on the left) and the corresponding histogram (on the right).

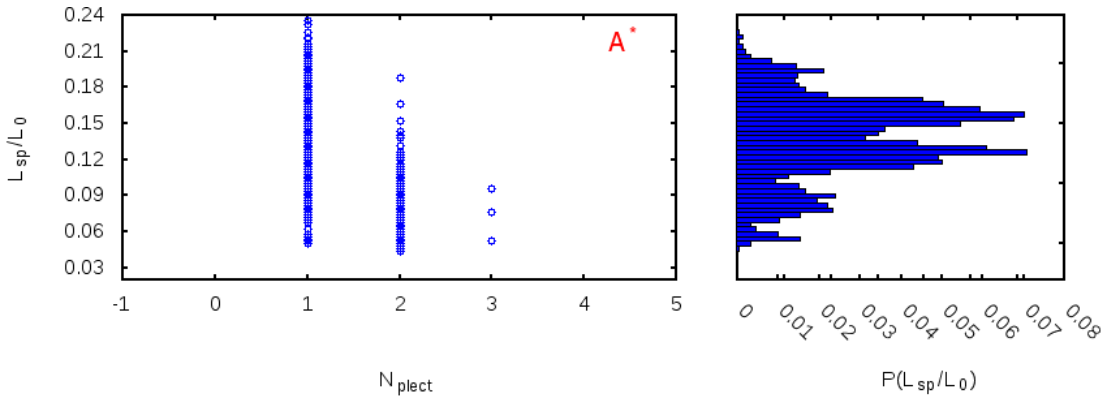

Figure 6.24: Length of a single plectoneme versus N_{plect} for point $A^* = (31, 10.0)$. Its histrogram is reported on the right.

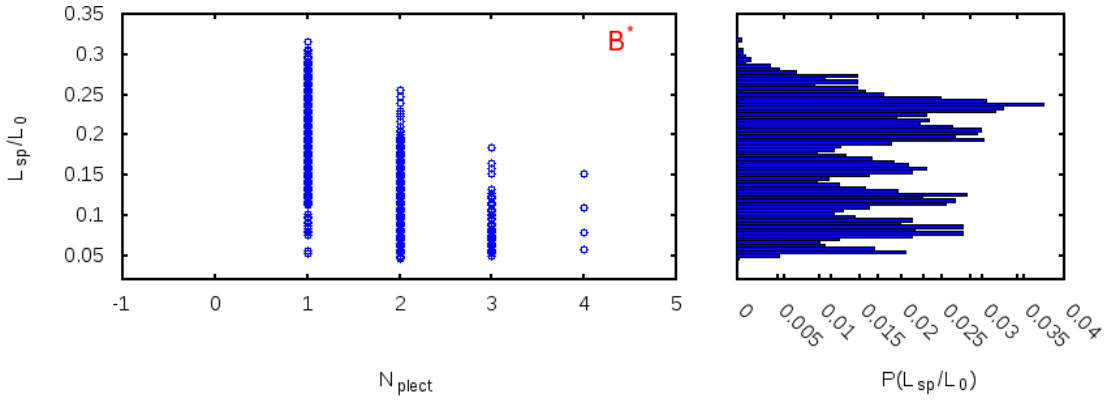

Figure 6.25: Length of a single plectoneme versus N_{plect} (and its histogram) for point $B^* = (32, 10.0)$.

Table 6.3 sums up the data of the previous graphics.

(Ca, F)	N^o of plectonemes	N^o of data	$\widehat{L_{sp}}$
$A = (31, 11.6)$	1	1044	0.0693 ± 0.0005
	2	6	0.0543 ± 0.0032
$B = (32, 13.3)$	1	690	0.0634 ± 0.0004
	2	8	0.0567 ± 0.0030
$A^* = (31, 10.0)$	1	3036	0.1411 ± 0.0005
	2	318	0.0812 ± 0.0012
	3	3	0.0747 ± 0.0127
$B^* = (32, 10.0)$	1	2091	0.2182 ± 0.0008
	2	1720	0.1128 ± 0.0009
	3	105	0.0839 ± 0.0026
	4	4	0.0995 ± 0.0205

Table 6.3: Values of the average normalized length of a single plectoneme depending on (Ca, F) and on N_{plec}.

Looking at the cases with a more reliable statistics (points A^* and B^*), evidently the length of a single domain decreases as the number of plectonemes rises. By comparing Tables 6.2 and 6.3 we can see that, if a configuration contains two domains, the total plectonemic length is equally divided between them: in fact $\widehat{L}_{plect}^{(A^*,2)} \simeq 2\widehat{L}_{sp}^{(A^*,2)}$ and $\widehat{L}_{plect}^{(B^*,2)} \simeq 2\widehat{L}_{sp}^{(B^*,2)}$.
The same thing can be said for configurations with three domains: even if the statistics isn't very acceptable, we note that $\widehat{L}_{plect}^{(B^*,3)} \simeq 3\widehat{L}_{sp}^{(B^*,3)}$.

6.2.4 Distribution of the plectonemic center of mass

Finally we look at the distribution of the center of mass of a plectoneme. We remind that the position of the center of mass is $N_{cm} = \frac{N_i+N_f}{2}$ where N_i and N_f are the positions of the initial and the final beads of a domain respectively (for example the yellow and the green beads of Fig. 6.2). In Figs. 6.26 and 6.27 we show the histograms for the normalized N_{cm} (i.e. N_{cm} divided by the total number of beads composing a chain $N_0 = 250$): the plectonemes for which we calculate N_{cm} are the same of the ones studied in Subsection 6.2.3.
All the below histograms present two spatial limits $N_{cm}/N_0 \simeq 0.1$ and $N_{cm}/N_0 \simeq 0.9$, which are the average relative positions of the upper and lower fork of the braid (reported as vertical green lines), so a plectoneme cannot form beyond these points. Figs. 6.26 and 6.27 show different behaviors: for points near the transition (A and B) plectonemes don't have favorite sites of nucleation, while when we are in the deep buckling phase (A^* and B^*) we mostly find domains near the upper fork (low values of N_{cm}/N_0).

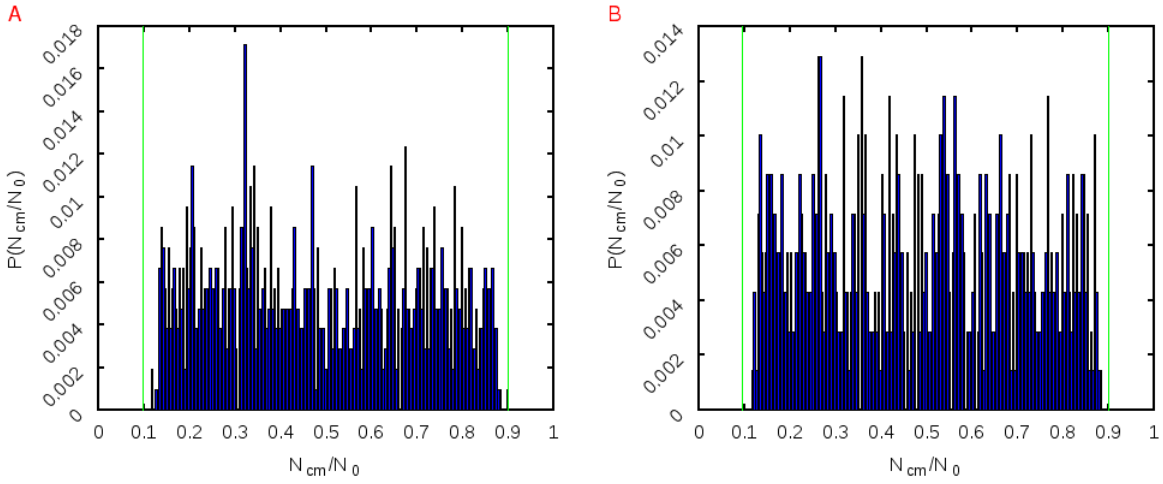

Figure 6.26: Positions of the plectonemic center of mass for points $A = (31, 11.6)$ and $B = (32, 13.3)$. On the abscissa one finds the normalized position, namely N_{cm} divided by the number of beads forming a strand $N_0 = 250$.

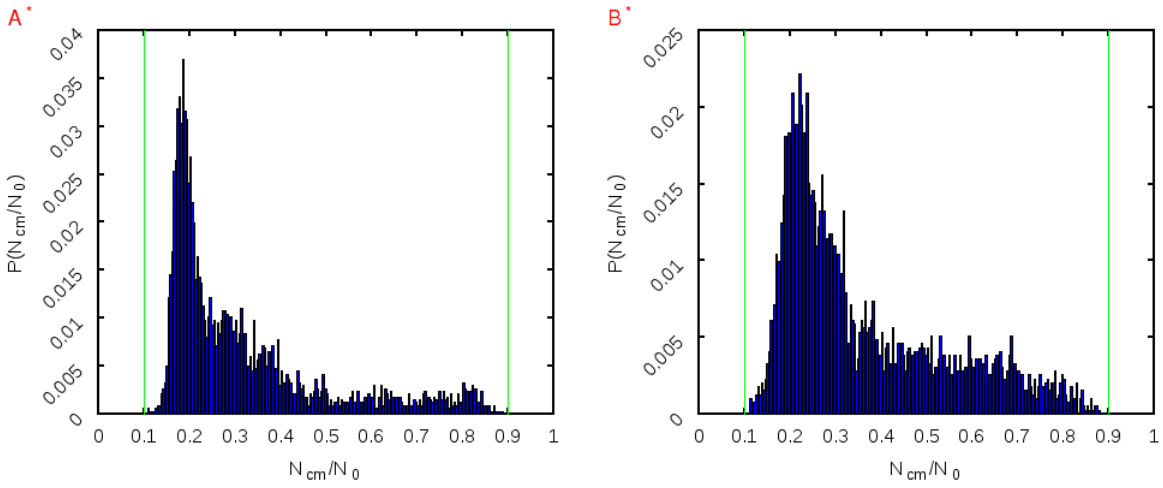

Figure 6.27: Normalized positions of the plectonemic center of mass for points $A^* = (31, 10.0)$ and $B^* = (32, 10.0)$.

Chapter 7

Introduction of local defects: the buckling transition on filaments with heterogeneous rigidity

In natural conditions, the bending rigidity of a double-stranded DNA chain can vary often: it is influenced by the surrounding environment (i.e. the salt concentration of the buffer in which it is immersed), but one can also find local stiffness changes due to the base sequences [1] or to the presence of binding proteins [28, 29].
It is therefore reasonable to study how the buckling transition varies by including sharp variations (local kinks) along the contour length of the strands. In order to introduce kinks as regions of high flexibility, we set $K = 0$ in 4.3.
The only case we'll focus on is the one with an intermediate intertether distance, i.e. $d = 0.168\, L_0$. From Chapter 5 one knows that in these conditions, if $Ca = 42$ (which is the maximum catenation for $F = 11.6, 13.3, 14.9, 16.6$ pN), the larger value of N_{plect} is $N_{plect} \simeq 3$: we decide to place six kinks (three in each strand), with the aim to observe a transition with different characteristics (for example one could expect to find an higher number of plectonemes, because maybe the lack of stiffness favorites the nucleation). Each kink involves three atoms: this means that we set $K = 0$ for six *angles* reported in the LAMMPS *Input File* (see Appendix A) [2]. The relative position of the central bead of every kink N/N_0 is reported in Table 7.1: N is the same variable seen in Section 6.1, namely the ID number of the LAMMPS *Input File* for the blue chain, while it corresponds to the ID number minus 250 for the red one.
In the following sections we're going to analyze the statics of the buckling transition (as in Chapter 5), the equilibrium dynamics of plectonemes and their statistics (with the same tools used in Chapter 6) in presence of these stiffness inhomogeneities.

[1] The regions of the chain with adenine-thymine base pairs are more flexible than the ones rich of guanine-cytosine.

[2] Every strand contains three kinks each of which includes three beads: so the region with null stiffness accounts for 0.036% of the total contour length $L_0 = 250\sigma$.

Strand	Kink relative position		
Blue	0.38	0.55	0.69
Red	0.48	0.61	0.80

Table 7.1: Relative position N/N_0 of the kinks in the blue and in the red strand. N_0 is the total number of beads in each chain, i.e. $N_0 = 250$.

7.1 Statics of the buckling transition in the presence of kinks

For $F = 10.0, 11.6, 13.3, 14.9, 16.6$ and 18.3 pN we will report results concerning the statics of the buckling transition. The procedure is the same of the one illustrated in Chapter 5: once fixed the pulling force F and the catenation Ca, we allow the system to relax and then we extract the mean physical quantities (end-to-end distance Ext, number of plectonemes N_{plect} and total plectonemic length L_{plect}) by considering uncorrelated configurations of the extension plateaux. The behavior of plectonemes, i.e. their number and length, is derived by contact maps, where we set the same conditions of Section 5.1. Below, in Fig. 7.1 , we show the setup used for this study: the green beads indicate the positions of kinks.

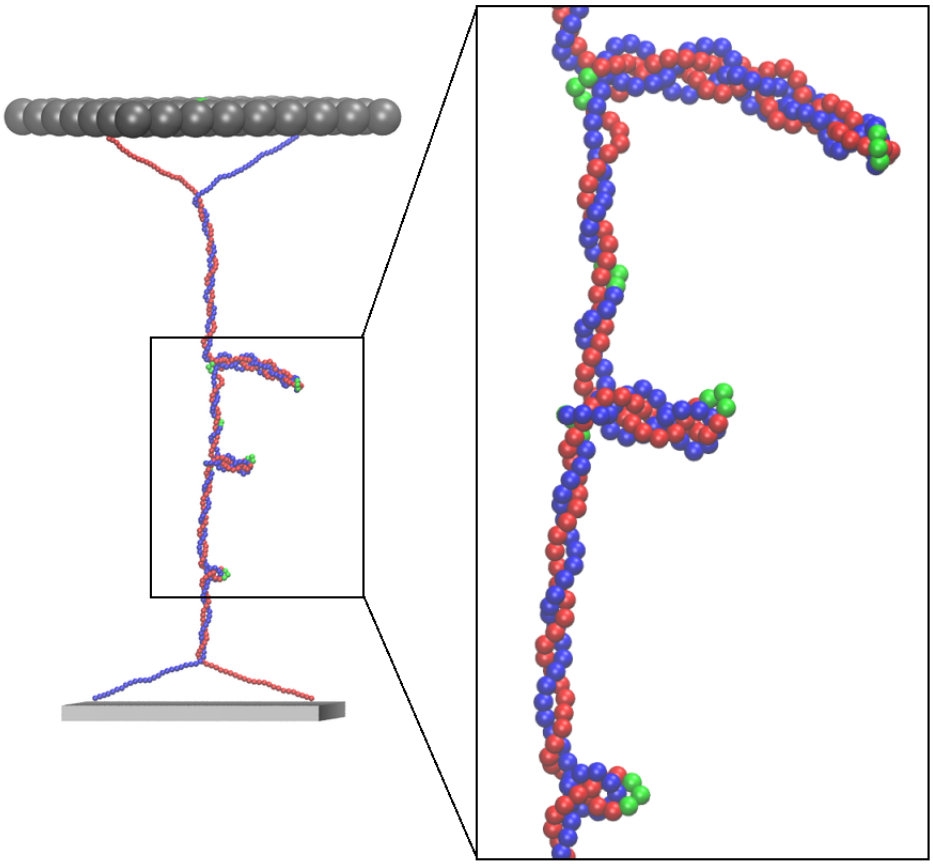

Figure 7.1: Setup of our simulation model with kinks (green beads) for $Ca = 35$ and $F = 10.0$ pN.

In Figs. 7.2, 7.3, 7.4, 7.5, 7.6, 7.7 we report the main results for the different forces: for each one, we compare Ext/L_0, N_{plect} and L_{plect}/L_0 with the case without defects.

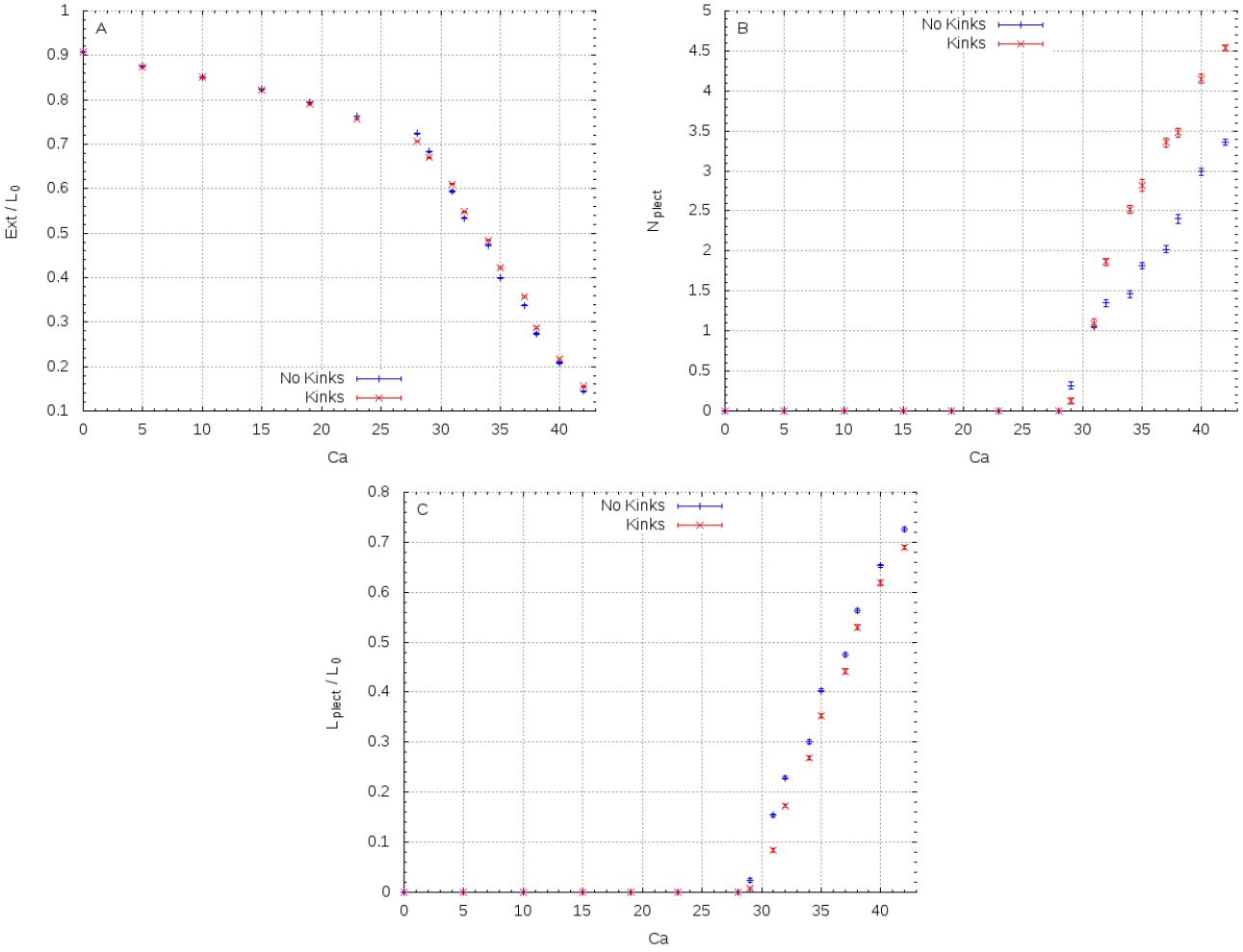

Figure 7.2: Analysis of the statics of the buckling transition with kinks. The figure is referred to the case in which the pulling force is $F = 10.0$ pN. (A): end-to-end distance versus catenation both for the case with and without kinks. (B): number of plectonemes over catenation for both the cases (with and without defects). (C): normalized total length of the plectonemic phase. Again we compare the two setups.

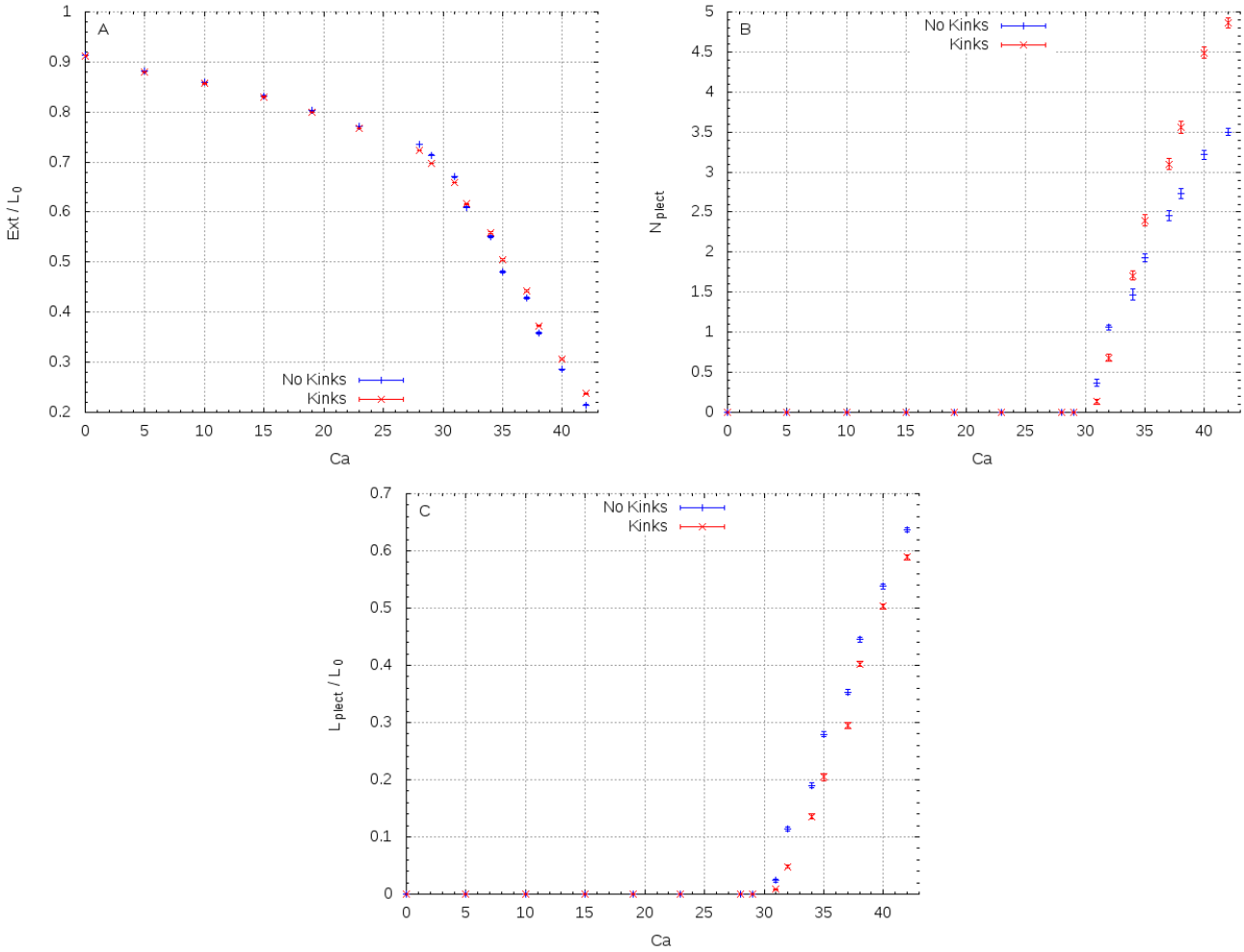

Figure 7.3: Statics of the buckling transition for the tension $F = 11.6$ pN. In the three panels we show both the setups (with and without kinks). (A): normalized extension versus catenation. (B): number of plectonemes versus catenation. (C): normalized total length of plectonemes over Ca.

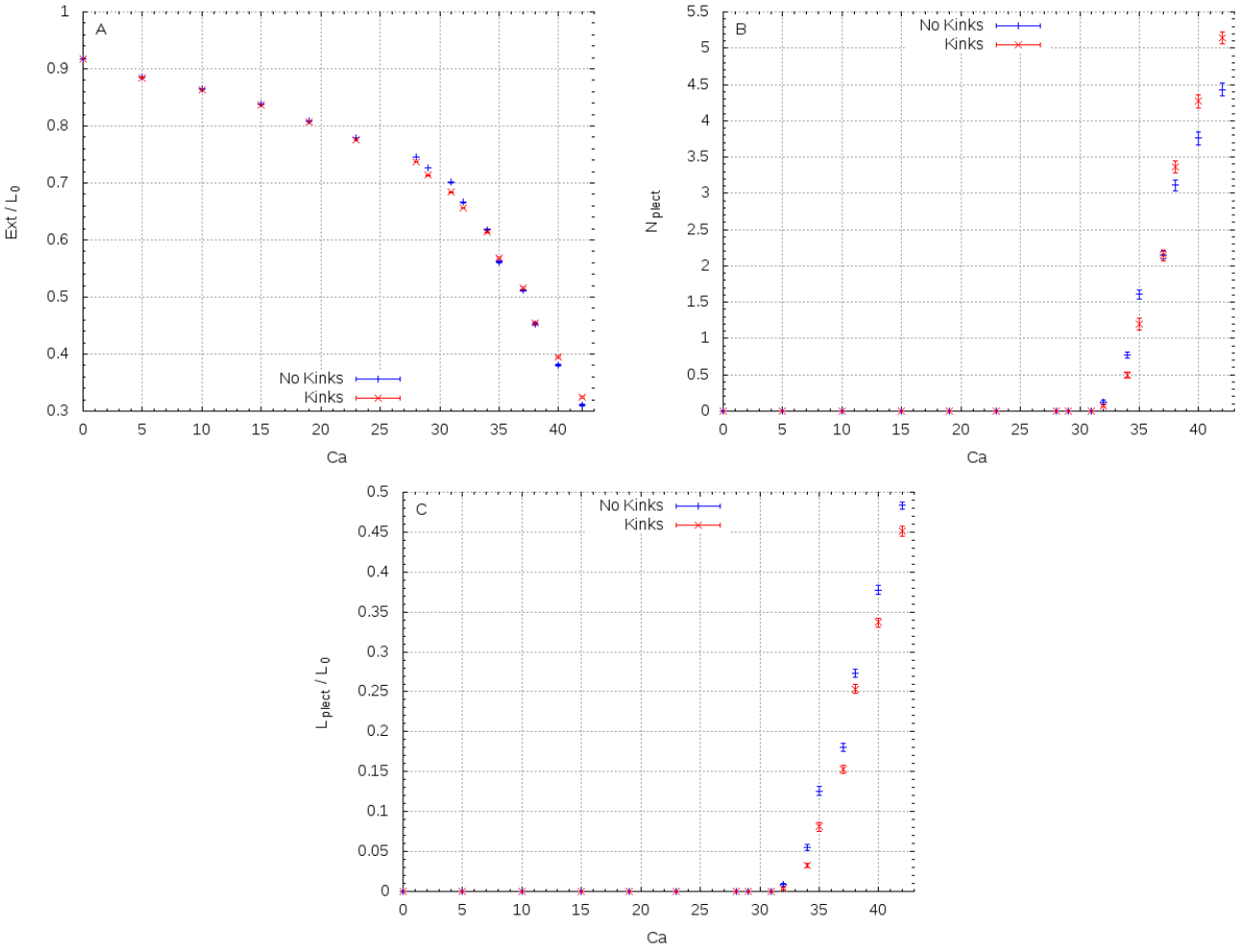

Figure 7.4: Statics of the buckling transition for $F = 13.3$ pN (A): end-to-end distance versus catenation. (B): number of plectonemes over catenation. (C): normalized total length of the plectonemic phase over Ca.

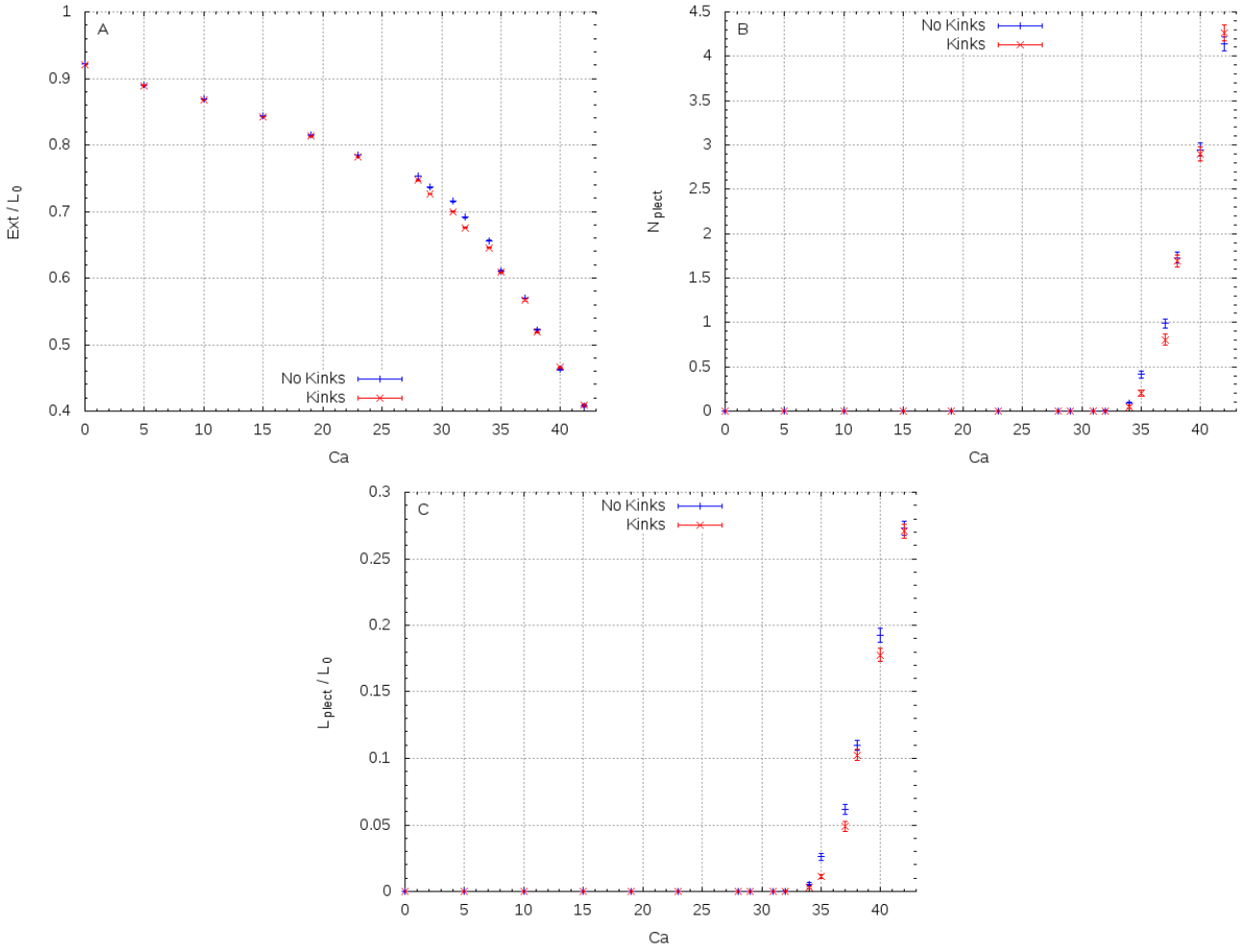

Figure 7.5: Buckling transition (both with and without kinks) for $F = 14.9$ pN. (A): normalized Ext over Ca. (B): number of plectonemes versus catenation . (C): normalized total length of the plectonemic phase as a function of Ca.

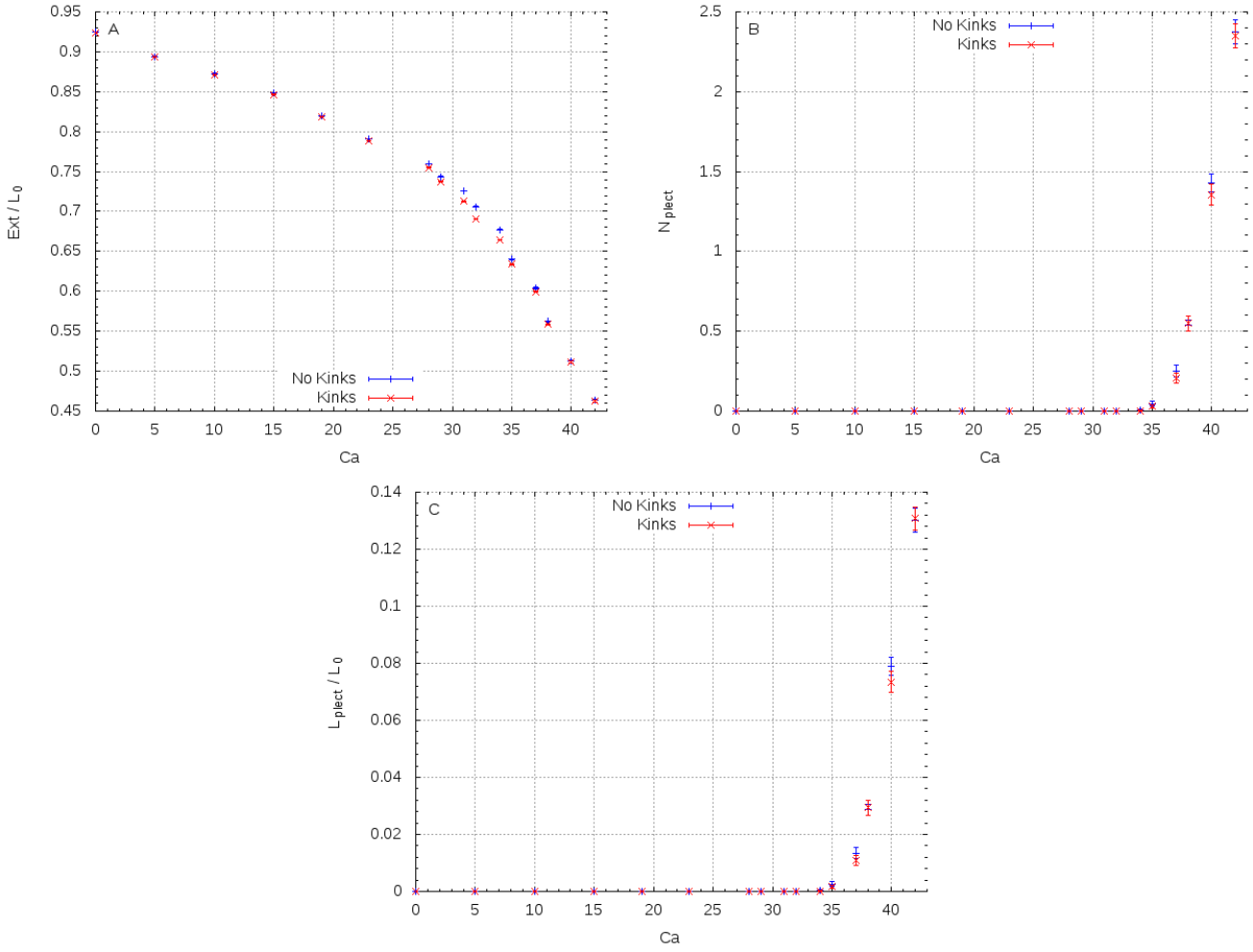

Figure 7.6: Statics of the buckling transition for $F = 16.6$ pN. (A): end-to-end distance versus catenation.(B): number of plectonemes over catenation. (C): normalized total length of the plectonemic phase over catenation.

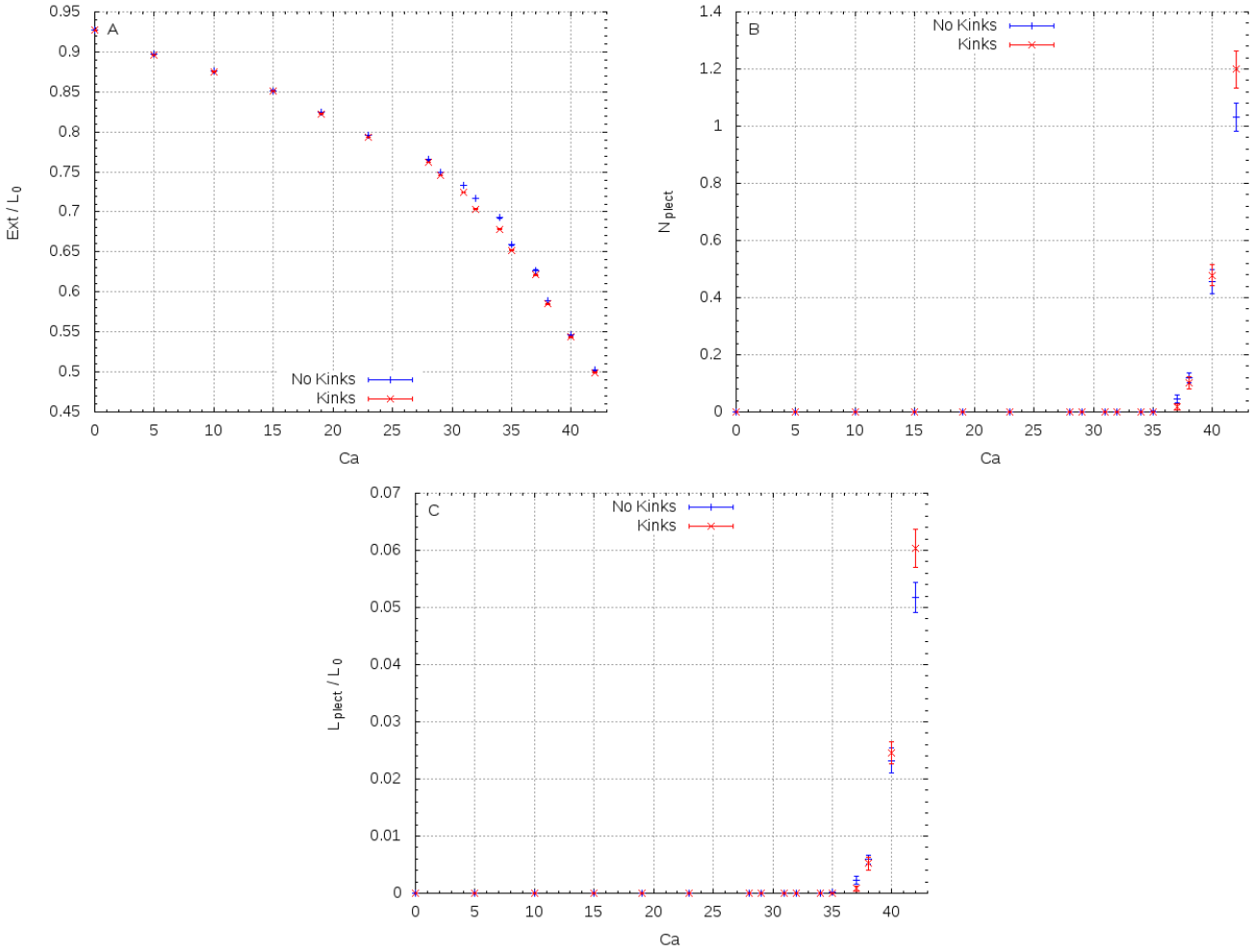

Figure 7.7: Buckling transition for $F = 18.3$ pN. (A): normalized Ext over Ca. (B): number of plectonemes versus catenation. (C): normalized total length of the plectonemic phase versus catenation.

In the previous figures one notes that the critical catenation (i.e. the catenation of the $(Ca, Ext/L_0)$ graphic where the curve slope changes) is practically unaffected by the presence of defects. Therefore the phase diagram (Ca_c, F) remains the same seen in Section 5.2. However, there are apparent differences in the number of plectonemes and in the total plectonemic length, which are more visible for lower forces ($F = 10.0, 11.6, 13.3$ pN).
Let us indicate the number of plectonemes N^k_{plect} for the setup with local defects and N^{nk}_{plect} for the one without kinks. We observe that for weak forces there is an initial region (after the buckling) where $N^{nk}_{plect} > N^k_{plect}$, but for higher values of Ca we find an abrupt increase of N^k_{plect}. So the presence of kinks favors the nucleation of numerous domains when F is low and the catenation is large enough.

The total plectonemic length is weakly influenced by the introduction of kinks, even if its value is almost always slightly higher in the case with no defects (only for $F = 18.3$ pN we find that L^k_{plect} exceeds L^{nk}_{plect}).
The differences between the two cases (homogeneous and inhomogeneous braid) are reduced by increasing the pulling force, e.g. for $F = 16.6$ pN and $Ca \simeq 40$ we observe $N^{nk}_{plect} \simeq N^k_{plect}$, while for $F = 10.0$ pN and $Ca \simeq 40$ the discrepancy between these two values is apparent.
It's reasonable to think that kinks could form the end-loops of plectonemes, since their persistence length is null and so they would reduct the bending energy cost for the nucleation of a domain.

7.2 Equilibrium dynamics of plectonemes with kinks

In this section we'll study kymographs representing the movements at equilibrium of plectonemes in presence of local defects. In order to compare these results with the ones of Section 6.1, we focus on the four points $A = (31, 11.6)$, $B = (32, 13.3)$, $A^* = (31, 10.0)$ and $B^* = (32, 10.0)$ of the phase diagram (Ca_c, F) 6.1. As in Chapter 6, the yellow bars indicate beads belonging to a plectoneme, whose extremities are highlighted by red points, while the positions of kinks are showed through green horizontal solid lines.

7.2.1 Dynamics just past the transition

As in the previous chapter, we begin with points $A = (31, 11.6)$ and $B = (32, 13.3)$ of the phase diagram 6.1. In Fig. 7.8 we show two trajectories for point A [3] and in the same graphics we plot also the normalized end-to-end distance of the chains, which is referred to the right y axis.
As in Subsection 6.1.1, one notes the growth of a *gas* of small plectonemes: however we can underline some important differences between Figs. 6.3, 6.4 and 7.8.
First of all, in Fig. 7.8 we observe that the defects influence the positions of plectonemic domains: while in absence of kinks plectonemes form in every position within the two forks of the braid, here it's apparent that domains prefer to nucleate near the local defects.
Often the kinks are placed in the center of the yellow bars, therefore they coincide with the end-loops of plectonemes: we can expect that the distribution of the plectonemic centers of mass will be influenced throughly by the introduction of kinks.
Another difference between the cases with and without kinks is observed on the survival time of plectonemic domains. Even if we haven't yet performed an extensive statistical analysis about it, in Fig. 7.8 the plectonemes appear qualitatively more unstable than in Figs. 6.3 and 6.4, suggesting that local defects make the domains lifetime shorter.

[3] Time is expressed in Lennard-Jones units τ. The τ to seconds conversion is explained in Appendix B.

Finally, sometimes the Ext suffers from the nucleation of end-loops (such as at time $t \simeq 80000\,\tau$ in the upper panel of Fig. 7.8), but one cannot see deep differences in comparison to the case with no defects.

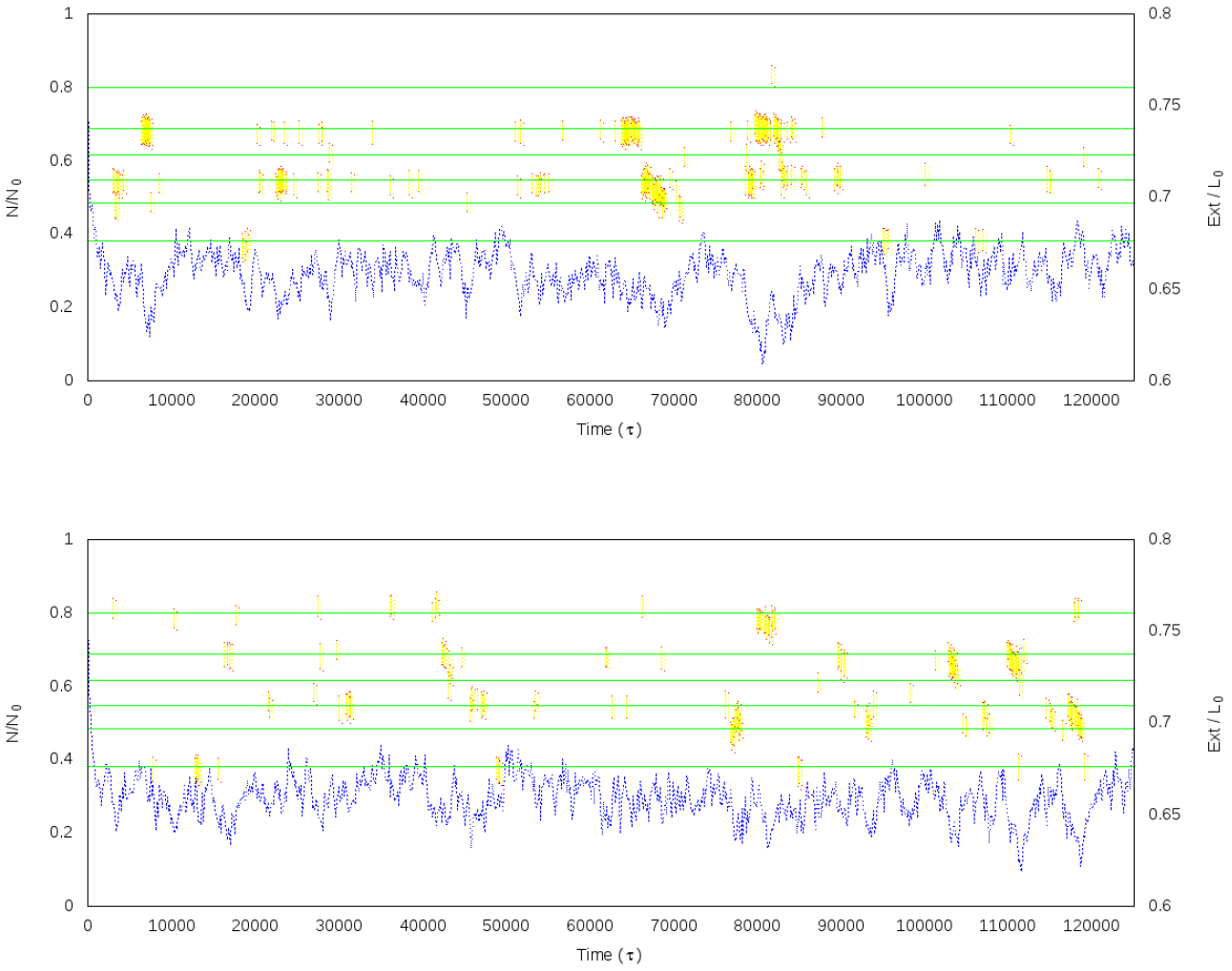

Figure 7.8: Kymographs for $F = 11.6$ pN and $Ca = 31$ in the presence of kinks. On the left axis there is the relative (or normalized) position of plectonemes; on the right one we find the values of the normalized end-to-end distance (dotted blue lines).

Fig. 7.9 reports two kymographs for point B ($F = 13.3$ pN and $Ca = 32$).

Figure 7.9: Two trajectories for $F = 13.3$ pN and $Ca = 32$ obtained from the setup with local defects.

Considerations are similar to the ones made for point A. Comparing Fig. 7.9 with Figs. 6.5 and 6.6, we conclude that, in the setup with kinks, plectonemes with a smaller survival time nucleate and they are mostly located in proximity of the defects, which often form their end-loops. In Fig. 7.9 the number of domains is lower than in Fig. 7.8, since point B is closer to the transition line than point A.

7.2.2 Dynamics inside the buckling phase

In this Subsection we monitor the time evolution of plectonemes for the two points of the phase diagram 6.1 $A^* = (31, 10.0)$ and $B^* = (32, 10.0)$. One can predict some changes in the dynamics, since in Section 7.1 we have seen that for $F = 10.0$ pN and $Ca = 32$ the quantity N_{plect} exhibits a noticeable gap between the cases with and without kinks.

In Fig. 7.10 we report two kymographs for point A^*, i.e. for $Ca = 31$ and $F = 10.0$ pN. The blue solid line shows the normalized end-to-end distance whose values can be found in the right y axis.

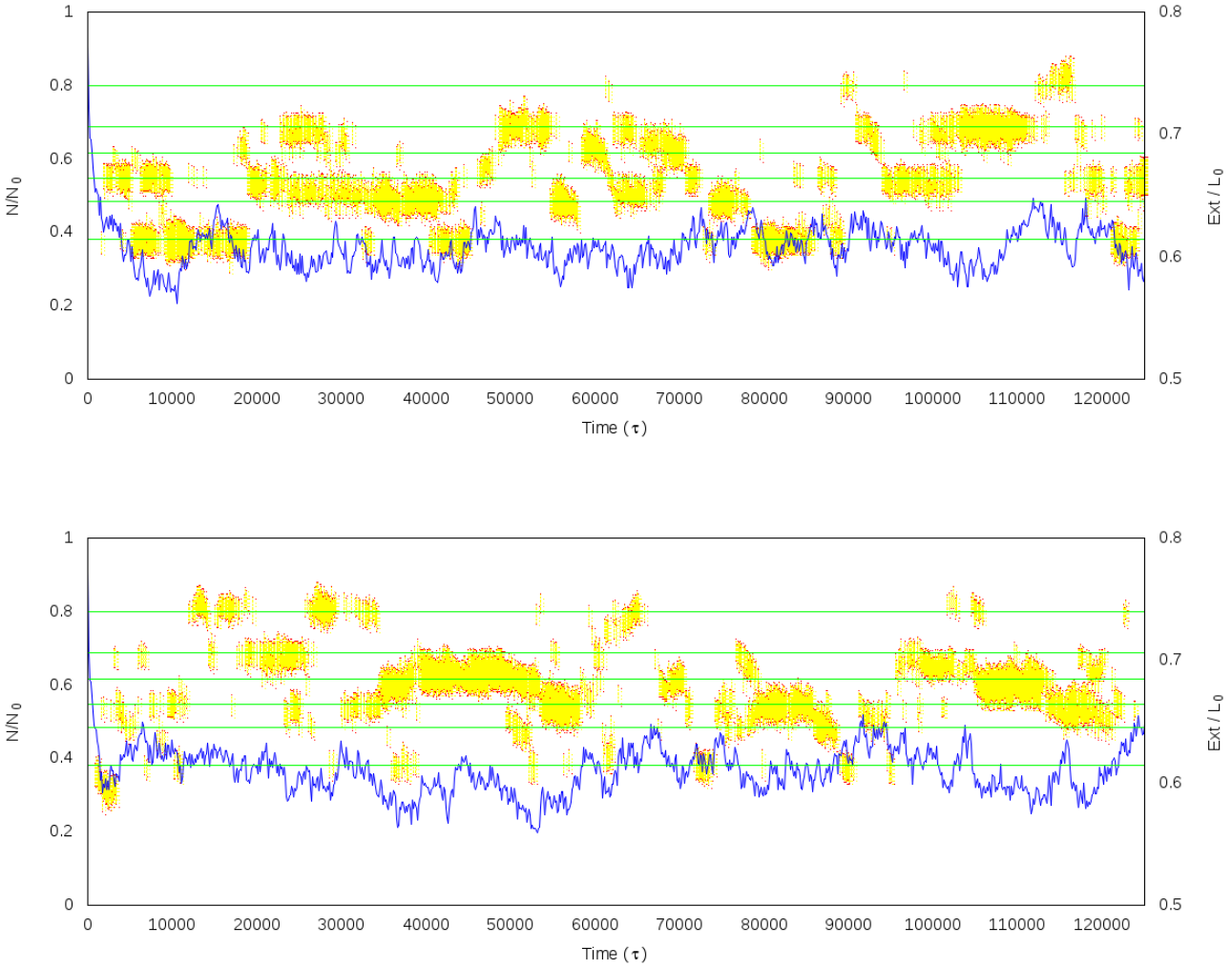

Figure 7.10: Kymographs for $F = 10.0$ pN and $Ca = 31$ in strands with local defects.

By looking at Figs. 6.7, 6.9 and 7.10, one observes a rather different dynamics when kinks are present.
In Figs. 6.7 and 6.9 we found a long-lived plectoneme which sometimes splits into two domains: specifically, we observed particular events, such as the merge of two domains and the *hopping* mechanism.
The introduction of local defects changes this behavior in an appreciable way. First of all note that kinks reduct the lifetime of plectonemes: in Fig. 7.10 we don't observe a single domain dominating the dynamics, but there is a continuous nucleation and destruction in proximity of the kinks. As for the cases close to the buckling transition (points A and B), the kinks prefer to form the end-loops, so they are located in the middle of the yellow bars.
This *fragmented* dynamics doesn't allow to recognize apparent merging events between two plectonemes as the ones seen in Fig. 6.7: almost each kink is located in the plectonemes end-loops where the required bending energy cost would be higher.
Finally we focus on point $B^* = (32, 10.0)$ shown in Fig. 7.11. Again the defects have the effect of pinning the plectonemic domains, which tend to be apart, without giving rise to the formation of a single large domain (as in Figs. 6.10 and 6.11).
Thereby we can conclude that the local changes of the bending stiffness greatly affects the dynamics of plectonemes: two domains have less probability to merge because the nucleation is favored in the proximity of a kink and this results in the formation of numerous and smaller plectonemes.
We can also expect that the statistics will exhibit substantial differences (mostly the distribution of the plectonemic centers of mass): these aspects will be discussed in the next section.

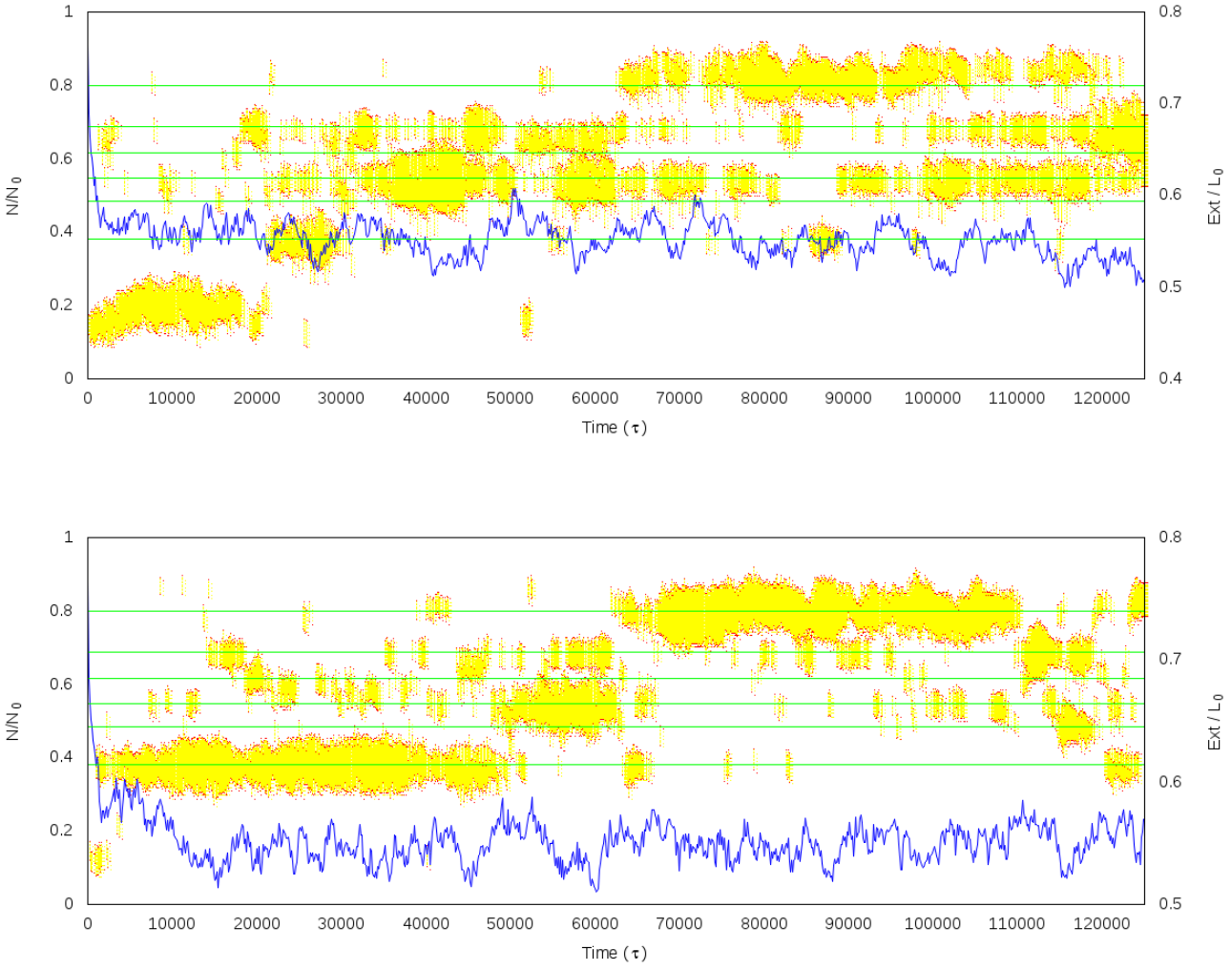

Figure 7.11: Trajectories for $F = 10.0$ pN and $Ca = 32$ in strands with local defects.

7.3 Plectonemic statistics in chains with varying stiffness

The last aspect worth to be examined is the statistics of plectonemes, i.e. the distribution of the end-to-end distance Ext, of the total plectonemic length L_{plect} and of the size of the single plectoneme L_{sp}. The notation which we'll use is the same introduced in Section 6.2: every quantity will be studied in relation to the number of plectonemes and to the point of the phase diagram 6.1, therefore for $N_{plect} = N$ and for a configuration P [4] the average normalized extension Ext/L_0 is indicated by $\widehat{Ext}^{(P,N)}$ (a similar notation will be used for L_{plect} and L_{sp}).
All the following results have been obtained by averaging over 200 runs and considering only uncorrelated configurations.

7.3.1 Distribution of the end-to-end distance

Let us start with the study of the braid extension. In Figs. 7.12, 7.13, 7.14 and 7.15 we show the normalized Ext as a function of the number of domains and in the right panels it is possible to observe the related histograms [5]. On the right panels we overlay also the corresponding probability for points A, B, A^* and B^* in absence of kinks (i.e. the same histograms seen in Chapter 6): these are indicated through boxes with red borders.

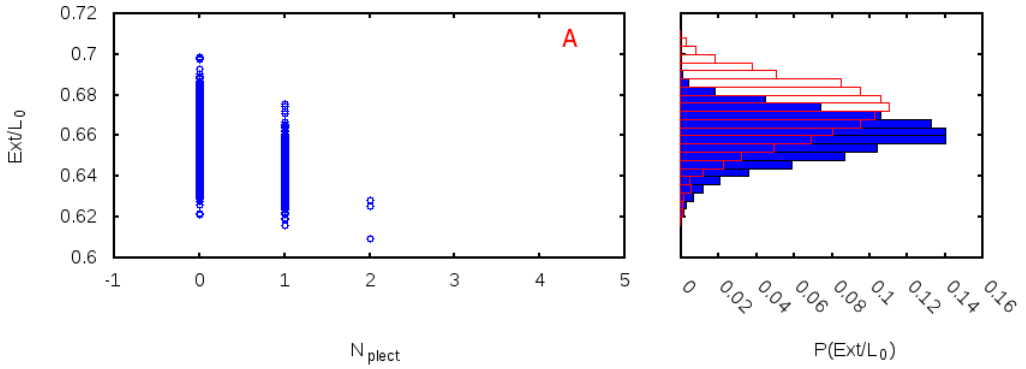

Figure 7.12: Ext/L_0 over N_{plect} and its histogram (on the right) for $A = (31, 11.6)$. Boxes with red borders show the histogram for point A when there are no kinks (the same histogram of Fig. 6.14).

[4] We remind that P could be $A = (31, 11.6)$, $B = (32, 13.3)$, $A^* = (31, 10.0)$ or $B^* = (32, 10.0)$.

[5] In the following histograms, the bin size is set equal to 0.004, which is the normalized diameter of a bead composing the strands (i.e. $\frac{\sigma}{L_0} = \frac{\sigma}{250\sigma} = 0.004$).

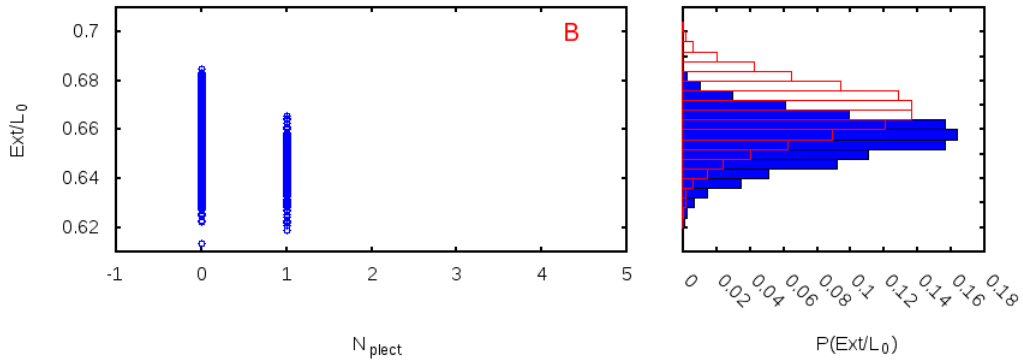

Figure 7.13: Ext/L_0 over N_{plect} and its histogram (on the right) for $B = (32, 13.3)$.

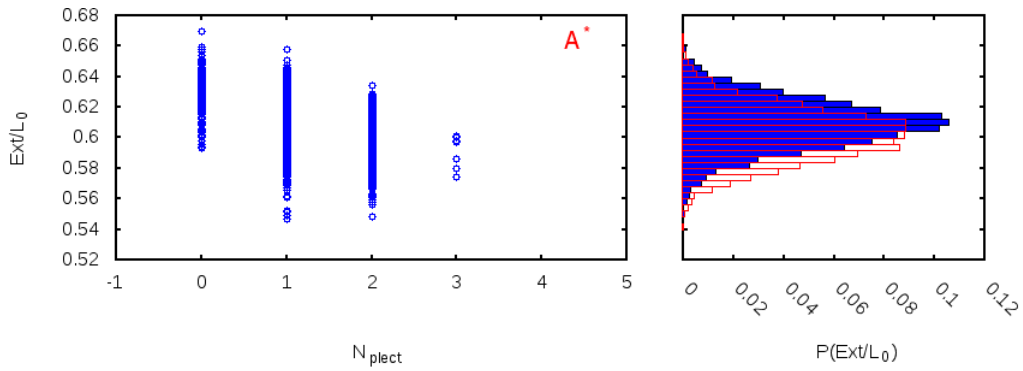

Figure 7.14: Ext/L_0 over N_{plect} and its histogram for $A^* = (31, 10.0)$

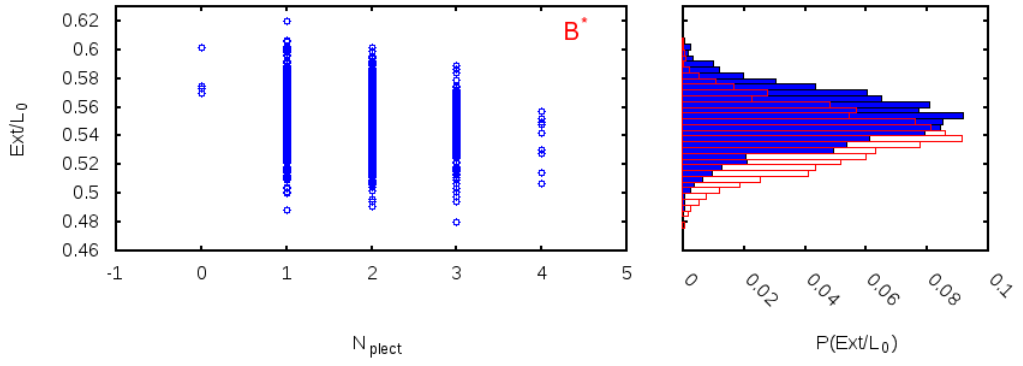

Figure 7.15: Ext/L_0 over N_{plect} and its histogram for $B^* = (32, 10.0)$.

Table 7.2 contains the mean values of the data reported in the above figures. Compared to the case without kinks (Subsection 6.2.1), the shapes of the frequency histograms don't undergo evident changes and the peaks are located approximately in the same positions; however great differences can be observed in the left panels. By the study of the statics we know that, for points $A = (31, 11.6)$ and $B = (32, 13.3)$, the number of plectonemes is higher for an homogeneous braid: this fact is reflected in Tables 6.1 and 7.2. In fact by considering point A one notes that in Table 6.1 the number of data for $N_{plect} = 0$ is 2258, while in Table 7.2 it is equal to 3567; on the other hand there is a remarkable decrease of the number of data for $N_{plect} = 1$ when we are dealing with strands characterized by an heterogeneous rigidity. The same features are observed for the case $Ca = 32$ and $F = 13.3$ pN , i.e. for point B.
A separate discussion has to be made for points belonging to the deep buckling phase ($A^* = (31, 10.0)$ and $B^* = (32, 10.0)$).
Looking at panel B of Fig. 7.2 we note that the mean number of domains for the two setups (with and without kinks) is similar when $Ca = 31$, while it is quite larger when $Ca = 32$ for configurations with local defects. Again this behavior is found in Tables 6.1, 7.2 and in Figs. 6.16, 6.17, 7.14, 7.15. In Fig. 7.14 one sees that the number of data for $N_{plect} = 0$ considerably increases if compared to Fig. 6.16 , but at the same time also the one related to $N_{plect} = 2$ increases, suggesting that the mean number of plectonemes stays almost constant. Moreover, in Fig. 7.15 we find more data for $N_{plect} = 2, 3$ than in Fig. 6.17, which provokes a rise of the mean number of plectonemes for the configurations with kinks when $Ca = 32$ and $F = 10.0$ pN.

(Ca, F)	N^o of plectonemes	N^o of data	$\widehat{Ext}$
$A = (31, 11.6)$	0	3567	0.6618 ± 0.0002
	1	426	0.6462 ± 0.0005
	2	3	0.6212 ± 0.0058
$B = (32, 13.3)$	0	4437	0.6568 ± 0.0001
	1	239	0.6429 ± 0.0006
$A^* = (31, 10.0)$	0	266	0.6282 ± 0.0008
	1	1940	0.6092 ± 0.0003
	2	609	0.5987 ± 0.0006
	3	7	0.5909 ± 0.0041
$B^* = (32, 10.0)$	0	4	0.5796 ± 0.0074
	1	804	0.5564 ± 0.0007
	2	1379	0.5510 ± 0.0004
	3	307	0.5447 ± 0.0009
	4	9	0.5365 ± 0.0058

Table 7.2: Values of the mean normalized extension depending on (Ca, F) and on the number of plectonemes.

7.3.2 Total plectonemic length

We now give informations about the distribution of the normalized total plectonemic length. In Figs. 7.16, 7.17, 7.18, 7.19 and in Table 7.3 results obtained from 200 simulative runs are summarized. In the right panels of the following figures, boxes with red borders depict frequency histograms for the case without kinks.

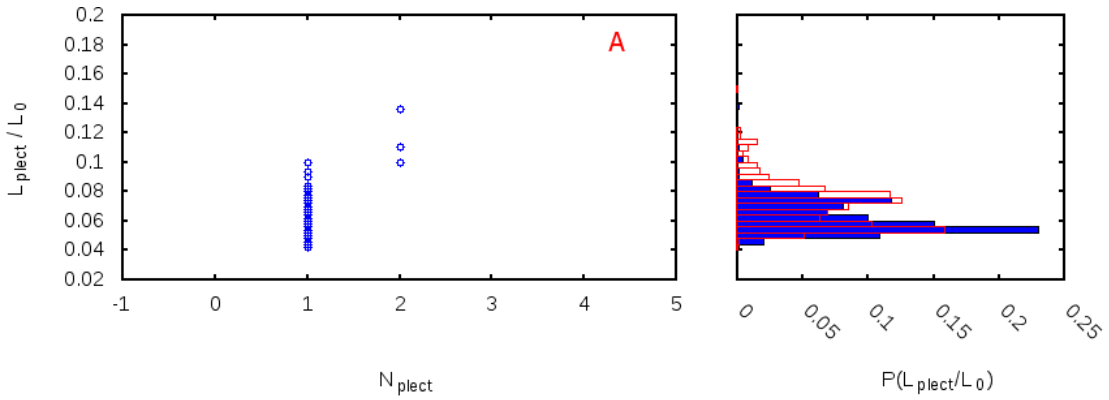

Figure 7.16: Normalized total length of the plectonemic phase versus the number of plectonemes and its histogram (on the right) for $A = (31, 11.6)$.

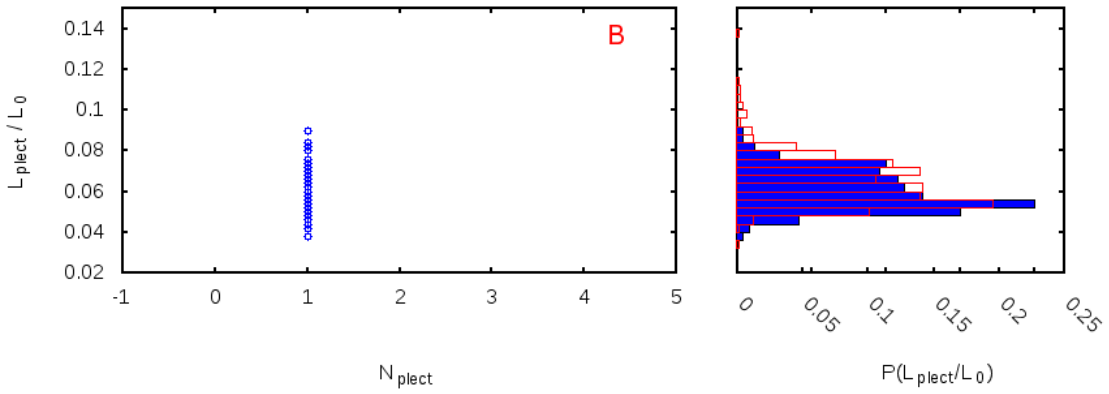

Figure 7.17: Normalized total plectonemic length over the number of domains for $B = (32, 13.3)$. The related frequency histogram is shown on the right.

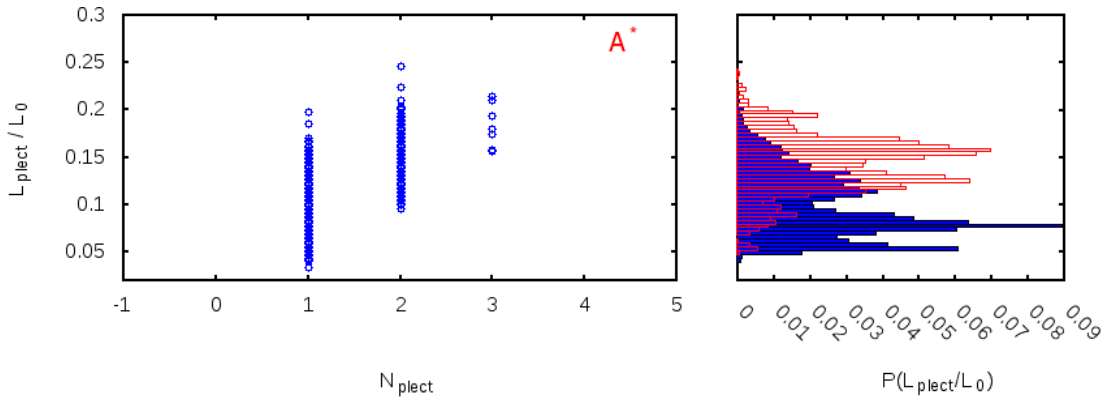

Figure 7.18: Normalized total plectonemic length (and its histrogram) over N_{plect} for $A^* = (31, 10.0)$.

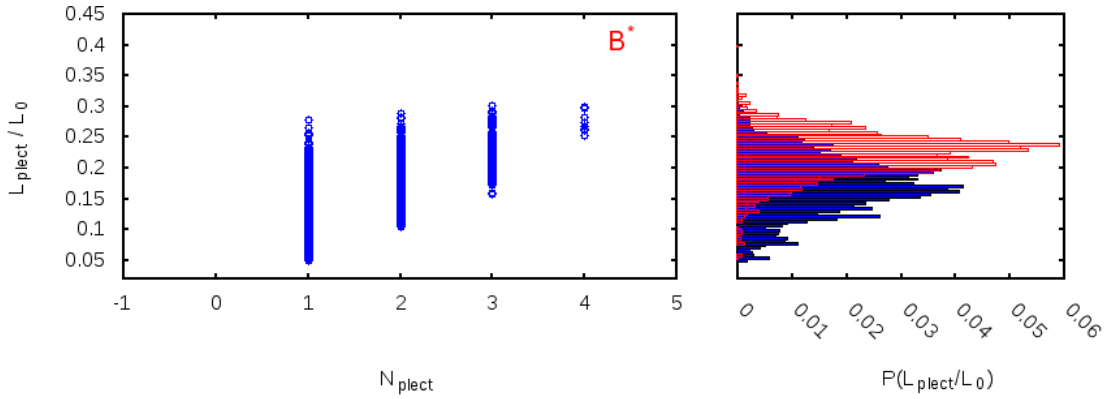

Figure 7.19: Normalized total length of the plectonemic phase as a function of N_{plect} for $B^* = (32, 10.0)$. The corresponding frequency histogram is reported on the right.

(Ca, F)	N^o of plectonemes	N^o of data	$\widehat{L_{plect}}$
$A = (31, 11.6)$	1	426	0.0612 ± 0.0005
	2	3	0.1153 ± 0.0107
$B = (32, 13.3)$	1	239	0.0592 ± 0.0006
$A^* = (31, 10.0)$	1	1940	0.0839 ± 0.0005
	2	609	0.1398 ± 0.0009
	3	7	0.1837 ± 0.0088
$B^* = (32, 10.0)$	1	804	0.1327 ± 0.0015
	2	1379	0.1798 ± 0.0009
	3	307	0.2239 ± 0.0015
	4	9	0.2740 ± 0.0054

Table 7.3: Values of the mean normalized total plectonemic length depending on (Ca, F) and on the number of plectonemes.

Kinks influence the length of plectonemic domains throughly: even if the shape of histograms doesn't exhibit great differences compared to to the ones shown in Figs. 6.18, 6.15, 6.16 and 6.17 (except for the case $Ca = 31$ and $F = 10.0$ pN where the peak is evidently shifted toward the smallest values), generally in Table 7.3 one can notice that the presence of defects reduces $\widehat{L}_{plect}^{(P,N)}$ for every blue point P of the phase diagram 6.1 and for every $N = N_{plect} = \{0, 1, 2, 3, 4\}$.
This behavior could already be extrapolated from Figs. 7.2, 7.3 and 7.4 concerning the statics, where the total length of plectonemes appeared to be smaller in the setup with kinks.
However, the most visible variation is related to the change of L_{plect} when there is the nucleation of multiple domains. In Fig. 6.20, the emergence of a second end-loop implies a growth of $\sim 15\%$ in $\widehat{L}_{plect}$ [6], while in presence of defects this growth is equal to $\sim 67\%$. A similar result affects the point $B^* = (32, 10.0)$: without kinks the rise of the second plectoneme provokes an increase of $\sim 3\%$, while with kinks of $\sim 35\%$.
One can explain the origin of this behavior by looking at the dynamics of plectonemes. Without kinks (Figs. 6.7, 6.9, 6.10, 6.11), a plectoneme can grows in size, implying that, even if a single domain splits into two end-loops, the total plectonemic length stays almost constant.
Instead the presence of small and fully flexible regions has the effect of preventing the merging between two (or more) plectonemes, as we can see in Figs. 7.10 and 7.11. Therefore the formation of a second domain increases the length of the plectonemic phase noticeably.

[6] We mean that $\frac{\widehat{L}_{plect}^{(A^*,2)} - \widehat{L}_{plect}^{(A^*,1)}}{\widehat{L}_{plect}^{(A^*,1)}} \cdot 100 \simeq 15\%$.

7.3.3 Statistics of the single plectoneme length

As in Section 6.2, we now give a description of what happens to the size of a single domain when we're considering the braiding between strands with heterogeneous stiffness. One can see the main results in Figs. 7.20, 7.21, 7.22, 7.23 and in Table 7.4 (figures contain also the histograms of the configuration with no kinks and they are represented by boxes with red edges).

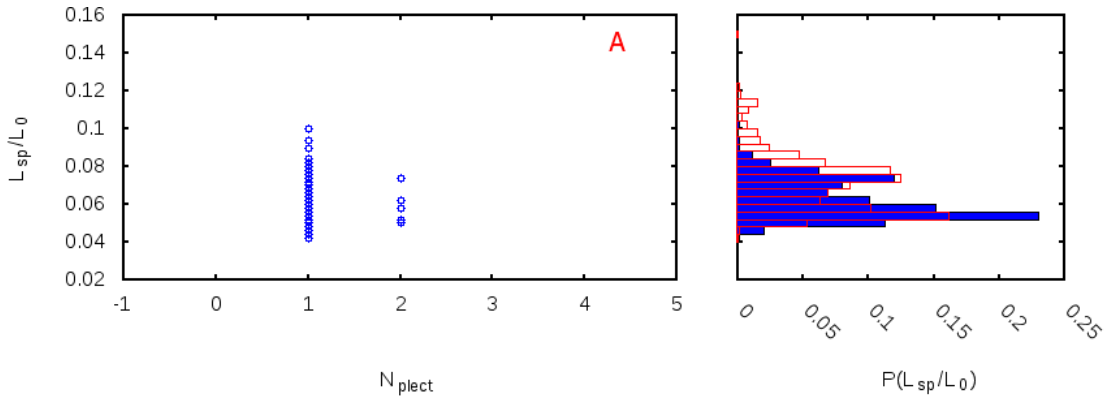

Figure 7.20: Normalized length of a single domain as a function of the number of plectonemes for $Ca = 31$ and $F = 11.6$ pN.

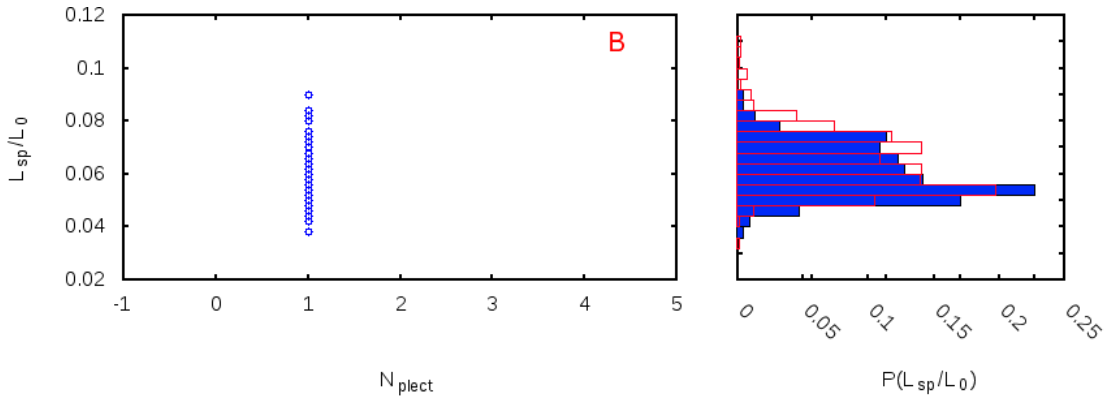

Figure 7.21: Normalized length of a single domain over number of plectonemes for $Ca = 32$ and $F = 13.3$ pN.

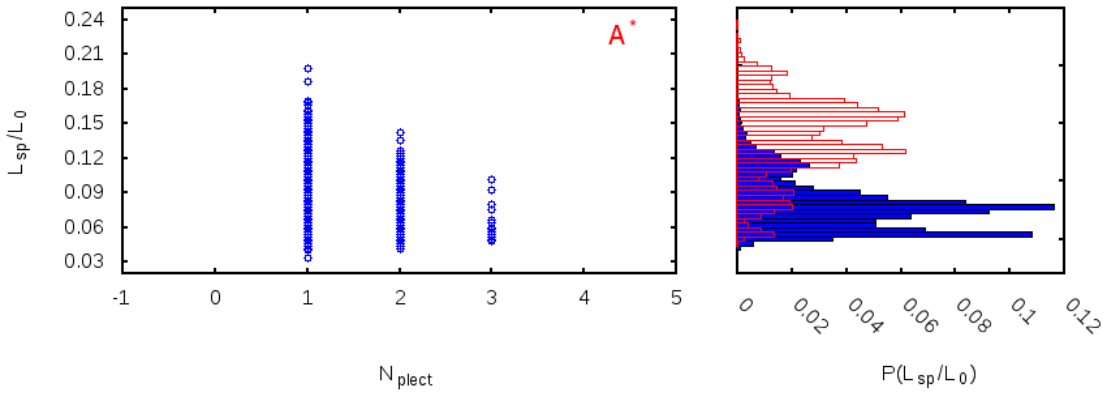

Figure 7.22: Normalized length of a single plectoneme versus N_{plect} for $Ca = 31$ and $F = 10.0$ pN.

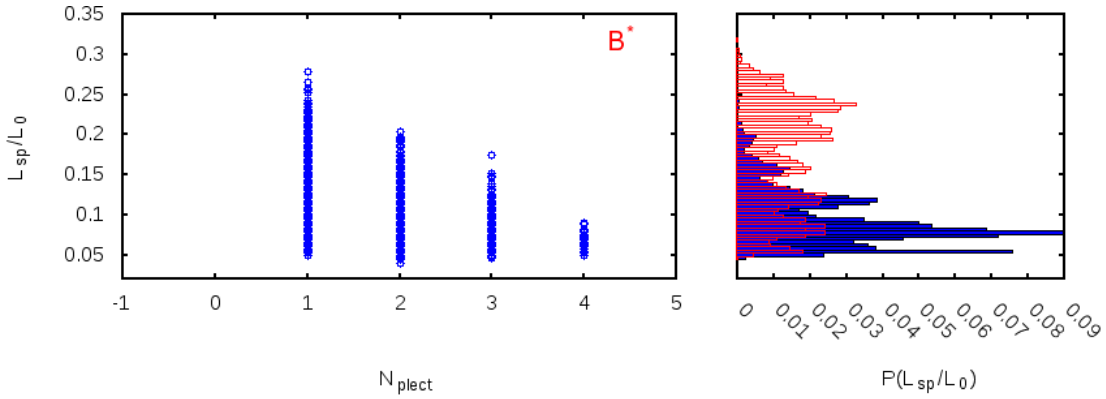

Figure 7.23: Normalized length of a single plectoneme over N_{plect} for $Ca = 32$ and $F = 10.0$ pN.

(Ca, F)	N^o of plectonemes	N^o of data	$\widehat{L_{sp}}$
$A = (31, 11.6)$	1	426	0.0612 ± 0.0005
	2	6	0.0577 ± 0.0038
$B = (32, 13.3)$	1	239	0.0592 ± 0.0006
$A^* = (31, 10.0)$	1	1940	0.0839 ± 0.0005
	2	1218	0.0699 ± 0.0005
	3	21	0.0612 ± 0.0032
$B^* = (32, 10.0)$	1	804	0.1327 ± 0.0015
	2	2758	0.0899 ± 0.0005
	3	921	0.0746 ± 0.0006
	4	36	0.0685 ± 0.0022

Table 7.4: Values of the mean normalized length of a single domain depending on (Ca, F) and on the number of plectonemes.

The situation is similar to the one presented in Subsection 6.2.3: the total size of the plectonemic phase prefers to divide equally between the different domains, i.e. $\widehat{L}_{plect}^{(A^*,2)} \simeq 2\widehat{L}_{sp}^{(A^*,2)}$, $\widehat{L}_{plect}^{(B^*,2)} \simeq 2\widehat{L}_{sp}^{(B^*,2)}$ and $\widehat{L}_{plect}^{(B^*,3)} \simeq 3\widehat{L}_{sp}^{(B^*,3)}$.
Furthermore it's interesting to observe how the mean size of a plectoneme changes for the two points A^* and B^* in the presence of defects (provoking evident variations in the shape of histograms). For example note that introducing fully flexible regions implies a decrease of 39% in $L_{sp}^{(B^*,1)}$ [7] and of 20% in $L_{sp}^{(B^*,2)}$. This confirms that, well inside the buckling phase, kinks enhance the nucleation of numerous and small domains.

7.3.4 Centers of mass of plectonemic domains

The last thing we investigate is the distribution of the centers of mass of plectonemes. In the previous chapter we saw that, for points close to the transition line (A and B), no favorite sites of nucleation are observed, while, well inside the buckling phase (A^* and B^*), end-loops prefer to form close to the upper fork of the braid.
In this setup, i.e. with kinks, we expect to mostly observe a growth of domains in proximity of the defects: the distribution of the centers of mass is shown in Fig. 7.24 where the positions of the central beads of kinks are represented as green solid lines. Actually one observes six peaks corresponding to the black lines: this confirms that kinks tend to be the nucleation points for the end-loops where bending is necessary greater.
We can also point out the presence of three higher peaks. These are localized in proximity of the position of the kinks belonging to the blue strand: this discrepancy between blue and red kinks is originated by our method of counting plectonemic domains. In fact we remind that if $N_b \leq N_r$, the domains are given by the blue strand (where N_b and N_r are the number of blue and red plectonemes respectively): the equal sign unbalances the counting of domains in favor of the blue strand, namely the plectonemes of the braid correspond more frequently to the blue ones than to the red ones.

[7] $\frac{\widehat{L}_{sp}^{(B^*,1),nk} - \widehat{L}_{sp}^{(B^*,1),k}}{\widehat{L}_{sp}^{(B^*,1),nk}} \cdot 100 \sim 39\%$ where the apexes k and nk indicate configurations with and without kinks respectively.

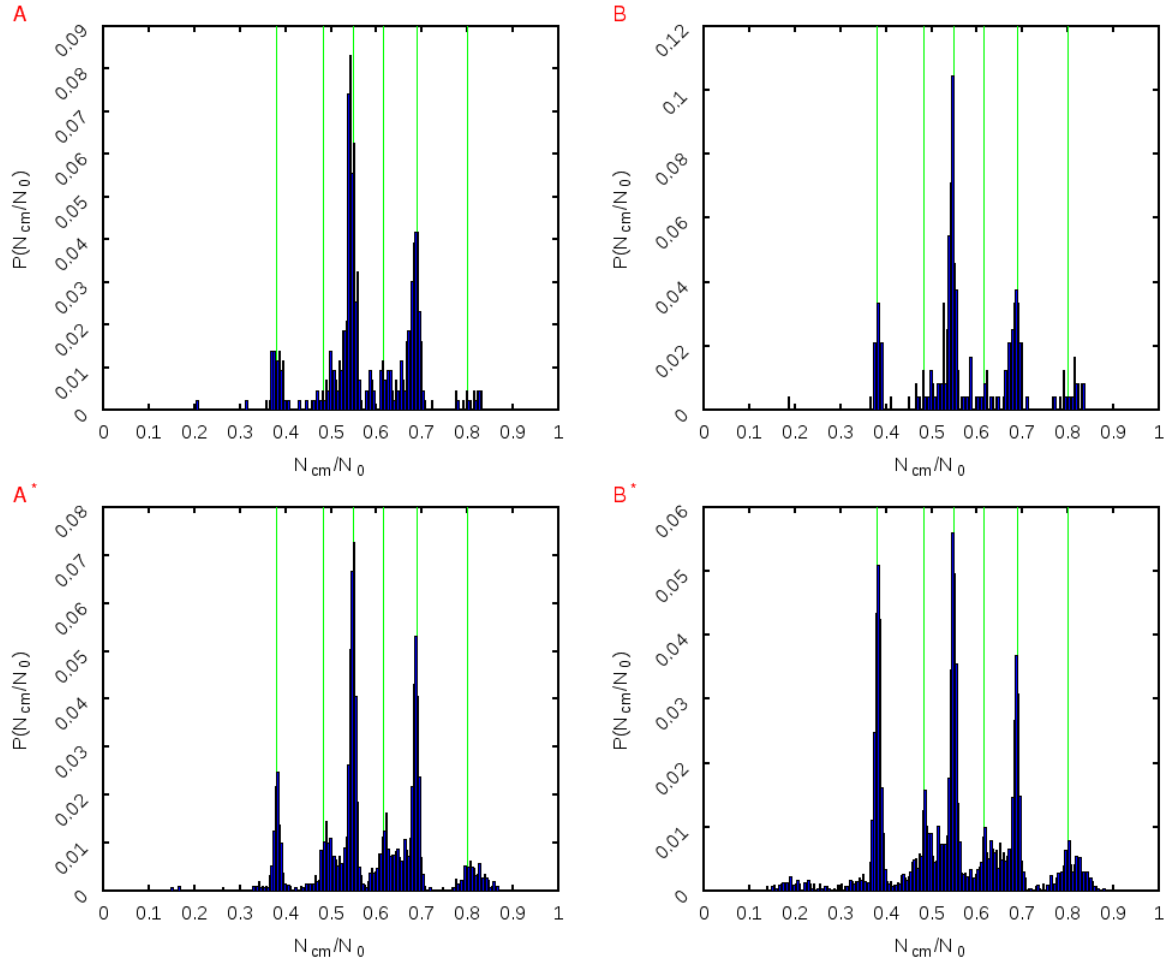

Figure 7.24: Normalized position of the centers of mass of plectonemic domains in the presence of kinks for points $A = (31, 11.6)$, $B = (32, 13.3)$, $A^* = (31, 10.0)$ and $B^* = (32, 10.0)$. The vertical green solid lines highlight the positions of the central beads of the defects.

Chapter 8

Conclusions

The aim of this thesis was to study the buckling transition of two strands subject to braiding and the possible formation of plectonemes.
Only few works have been published so far on this argument [6, 7, 20] and, as far as we know, this is the first study based on Brownian dynamics which comprehends a systematic analysis of the statics of the buckling transition combined with an introduction to the dynamics and statistics of plectonemes.
The state of the art of literature showed that, beyond a critical catenation, a two strands braid undergoes a phase transition with the formation of plectonemic domains. Experiments performed on nicked DNAs and a mechanical-statistical model highlighted how this transition depends on the intertether distance between the two strands d, on the pulling force F and on the ionic concentration of the buffer surrounding the chains.
Starting from these knowledges, we developed a coarse-grained model where two strands subject to Brownian motion could be twisted and pulled reproducing the action of the experimental magnetic tweezers setup.
We first focused on the statics of the buckling phase, being able to reproduce the typical (Ca, Ext) diagrams of braiding, whose *knees* indicate the critical catenation at which the transition occurs. Contact maps provided an efficient tool to localize plectonemic domains and allowed us to characterize the nature of the buckling transition, since we could count the number of end-loops and determine their length. In this way we confirmed previous results and we showed the importance played by d and F in this problem.
In addition we found other interesting results, such as:

- the presence of a solenoidal phase, which precedes the plectonemic one for high forces F and small intertether distances d;

- the formation of branched plectonemic domains at very high catenation values (where the end-to-end extension of the braid seems to reach a plateau).

In Chapter 6 we concentrated our efforts on the plectonemes equilibrium dynamics and on their statistics (i.e. the distribution of the end-to-end distance, of the total length of the plectonemic phase, etc.). Only the case $d = 0.168L_0$ was taken into

consideration and in particular we studied four points of the (Ca, F) phase diagram, two close to the transition line ($A = (31, 11.6)$ and $B = (32, 13.3)$) and other two well inside the buckling phase ($A^* = (31, 10.0)$ and $B^* = (32, 10.0)$).
Kymographs exhibit different behaviors: close to the transition we observe the formation of a gas of small plectonemic domains, while, well inside the plectonemic phase, one notices the presence of one or two more stable plectonemes which can split and merge changing the original position along the contour length. The mechanism of *hopping* was found for point A^*, and it is similar to the one observed by Loenhout et al. [27] experimentally in the diffusion of plectonemes in supercoiled DNAs.
The statistics of plectonemes indicates that the nucleation of the first domain greatly affects the end-to-end distance *Ext* and the total plectonemic length L_{plect}, while the formation of a second domain doesn't: this suggests that a plectoneme can grow in size and, if it splits into two end-loops, the length of the plectonemic phase stays almost constant. However, L_{plect} prefers to divide equally between the total number of plectonemes. Therefore, if there is only one domain, its length is L_{plect}, while if there are two end-loops each of them has a size equal to $L_{plect}/2$.
The analysis of the centers of mass of plectonemes distinguishes between points close to the transition (A and B) and the other two points deep in the buckling phase (A^* and B^*): the former don't have favorite sites along the braid where plectonemes form, the latter show an higher nucleation near the upper fork of the braid.
In Chapter 7 we introduced local defects in the strand rigidity, namely small fully flexible regions. We showed that the statics of the phase diagrams doesn't change, while the number of domains N_{plect} and their length L_{plect} present discrepancies compared to the case of homogeneously rigid strands: in fact normally N_{plect} increases in the presence of kinks, while L_{plect} is slightly smaller. These differences disappear by increasing the pulling force.
The introduction of kinks has also the effect of changing the plectonemes equilibrium dynamics dramatically, specially for points of the phase diagram inside the buckling phase. Domains now form in proximity of kinks which often coincide with their end-loops, where the bending energy would be larger.
The merging events are rarer since every defect tends to pin a plectoneme, preventing the fusion between two close domains. Also the plectonemic lifetime seems to be affected by the heterogeneous stiffness, in fact for points A^* and B^* we cannot still observe stable domains.
Finally the distribution of the plectonemic centers of mass confirms all the previous observations and it exhibits well defined peaks in correspondence of the kinks positions.

To conclude the study of the buckling phase in two-braids, one should perform a more systematic analysis of the plectonemes lifetime, in order to distinguish between different behaviors for points of the phase diagram near and far from the transition line. Another issue one could explore concerns the plectonemes dynamics upon a quench from one equilibrium phase to another: for example, starting from a point (Ca^*, F^*) in the buckling phase, one can suddenly increase the force keeping fixed the catenation and let the system relax toward the unbuckled phase. In such a

way we can monitor the dissolution of plectonemic domains. If we then decrease the force again passing through the transition line, we can study the re-nucleation dynamics of end-loops. For example it could be interesting to study where the domains re-nucleate: do they form in the same place of the original ones or their formation is independent from the initial configuration?
To extend this area of research, one can think to use the same simulative method to reproduce braids between three or more strands. The buckling transition is now more complex and we can assume that it should depend on the intertether distances between every pair of chains. These distances can be equal or not and in this last case the buckling point could be more influenced by an intertether distance than by the others. The reproduction of this setup could be also developed experimentally, by using *active colloids* as Goodrich and Brenner proposed [30].
Finally the simulation of topoisomerases' action should be worthy of attention. For example one can consider a setup where particles attached to the braid provoke a gate allowing the passage of a strand: therefore the catenation decreases and this decatenation process could depend on the intertether distance, on the pulling force, but also on the presence of local defects.

Appendix A

LAMMPS script

Below we show an example of the LAMMPS script used to obtain trajectories in which force can vary.

```
variable tname loop 1 10
variable tseed index 4332508 9592806 4224286 8664701 7861908 1622007 1519940
5823255 4327454 4695761

# Initialization
units lj
boundary p p p
atom_style angle
read_data Input_N250_Lk10
neighbor 10.3 bin
neigh_modify every 1 delay 1 check yes

# Define groups
group all type 1
group upperwall type 2
group upperatoms id 1 251
group downatoms id 250 500
group rotatingbeads union upperwall upperatoms
group pulledbead id 501
group others subtract all upperatoms

# Generating file for trajectory
dump 1 all custom 1000 Videos/Video_2s_N250_Lk10.${tname} id x y z
dump_modify 1 format line "%d %.4f %.4f %.4f"

# Potential information
pair_style lj/expand 1.1224615296218
pair_modify shift yes
pair_coeff 1 1 1.0 1.0 0.0
```

```
pair_coeff 1 2 1.0 1.0 3.3673845888654
pair_coeff 2 2 1.0 1.0 6.7347691777308

bond_style fene/expand
bond_coeff 1 30.0 1.5 1.0 1.0 0.0
special_bonds fene

angle_style cosine
angle_coeff 1 20.6

atom_modify sort 0 0.3
neigh_modify exclude molecule/intra rotatingbeads

reset_timestep 0
timestep 0.0025

region muro block -50.00 50.00 -1.0 0.0 -50.0 50.0 side out units box

label loopforce
variable force index 10.0 9.0 8.0 7.0
variable tempi_force index 5000000 5000000 5000000 5000000
variable tempi_dump index 50000 50000 50000 50000
dump_modify 1 every $tempi_dump

# Dynamics
fix 1 others nve
fix 2 others langevin 1. 1. 2. ${tseed}
fix 3 downatoms setforce 0.0 0.0 0.0
fix 4 others wall/region muro harmonic 200.0 1.0 1.0
fix 5 pulledbead smd cfor ${force} tether NULL 258.0 NULL 0.0
fix 6 rotatingbeads rigid group 1 rotatingbeads force 1 off on off torque 1 off off off run
${tempi_force}

next force
next tempi_force
next tempi_dump
jump SELF loopforce

clear
next tseed
next tname
jump SELF
```

This script generates 10 trajectories for every force, whose higher value is $10\frac{\epsilon}{\sigma}$ and the lower is $7\frac{\epsilon}{\sigma}$.
In *Initialization* units, boundary conditions and atom-style are set; then different groups are defined in order to create the rigid body forming the upper wall and to

identify its central bead on which we apply the pulling force. The group *rotatingbeads* has this name because in the *varying catenation setup* it includes all beads subject to torque.
As we have already said in Chapter 4, pair interactions are given by Lennard-Jones potentials that are used in their *expand* form allowing interactions between beads of different sizes.
Bonded beads interact via FENE potential, while three-body potentials are represented by the *cosine* style.
Finally, at the end of the script, we introduce dynamics: it incorporates Brownian motion, interactions between beads and the underlying wall and the force pulling the central bead of the rigid body.

Here we also show an example of an *Input File* used in LAMMPS scripts. *Atoms* with an identification number (ID number) [1] included between 1 and 250 form the first strand (the blue chain in Fig. 4.1), *atoms* with an ID number between 251 and 500 belong to the second strand (the red one in Fig. 4.1) and finally ID numbers grater than 500 are referred to beads forming the upper wall (*atom* 501 is the pulled bead).

```
LAMMPS data file from restart file: timestep = 0, procs = 1
563 atoms
498 bonds
496 angles

2 atom types
1 bond types
1 angle types

-60. 60. xlo xhi
-5. 260. ylo yhi
-60. 60. zlo zhi

Masses

1 1
2 0.001

Atoms

1. 1 1 -19.5770 226.1547 -7.5988 0 0 0
2. 1 1 -19.5635 225.1701 -7.9785 0 0 0
3. 1 1 -19.3286 224.1725 -8.0567 0 0 0
4. 1 1 -19.2718 223.1864 -8.2329 0 0 0
```

[1] The ID number is reported in the first column below the writing *Atoms*.

5. 1 1 -18.8601 222.2651 -8.3543 0 0 0
6. 1 1 -18.3027 221.4156 -8.2493 0 0 0
7. 1 1 -17.9154 220.5375 -8.2003 0 0 0
8. 1 1 -17.6613 219.5824 -8.2949 0 0 0
9. 1 1 -17.3716 218.6418 -8.2307 0 0 0
10. 1 1 -17.0035 217.7846 -8.2022 0 0 0
11. 1 1 -16.6481 216.8423 -7.9635 0 0 0
12. 1 1 -16.3411 216.0327 -7.4680 0 0 0
13. 1 1 -15.7337 215.3064 -7.3453 0 0 0
14. 1 1 -15.3912 214.3594 -7.2152 0 0 0
15. 1 1 -14.8552 213.4923 -7.0767 0 0 0
16. 1 1 -14.3487 212.7270 -7.0554 0 0 0
17. 1 1 -13.7572 211.8790 -7.0657 0 0 0
18. 1 1 -13.5348 210.9446 -7.0520 0 0 0
19. 1 1 -13.3034 209.9496 -7.1039 0 0 0
20. 1 1 -12.9145 209.0392 -7.1446 0 0 0

.
.
.
.
.
.
.
.

251. 2 1 19.5770 226.1547 7.5988 0 0 0
252. 2 1 19.3468 225.1503 7.4906 0 0 0
253. 2 1 19.1335 224.1370 7.4754 0 0 0
254. 2 1 18.8472 223.2222 7.5526 0 0 0
255. 2 1 18.5218 222.3152 7.4813 0 0 0
256. 2 1 18.1234 221.4447 7.3943 0 0 0
257. 2 1 17.6204 220.6553 7.4319 0 0 0
258. 2 1 17.4517 219.6842 7.4093 0 0 0
259. 2 1 17.3606 218.6648 7.6959 0 0 0
260. 2 1 17.2077 217.7078 7.8101 0 0 0
261. 2 1 16.8866 216.8031 7.7441 0 0 0
262. 2 1 16.4902 215.9295 7.7888 0 0 0
263. 2 1 16.3947 214.9921 7.7375 0 0 0
264. 2 1 16.0707 214.1131 7.8508 0 0 0
265. 2 1 15.9374 213.1202 7.8580 0 0 0
266. 2 1 15.6341 212.2307 7.6791 0 0 0
267. 2 1 15.2048 211.3645 7.6145 0 0 0
268. 2 1 14.8479 210.4599 7.5333 0 0 0
269. 2 1 14.5251 209.5134 7.3710 0 0 0
270. 2 1 14.1792 208.5982 7.4545 0 0 0
271. 2 1 13.8056 207.7051 7.4717 0 0 0

.
.

.
.
.
.
.
.

501. 3 2 0.0000 230.1547 0.0000 0 0 0
502. 3 2 -18.5038 230.1547 -29.7087 0 0 0
503. 3 2 -11.9782 230.1547 -27.1758 0 0 0
504. 3 2 -5.4525 230.1547 -24.6428 0 0 0
505. 3 2 1.0731 230.1547 -22.1099 0 0 0
506. 3 2 7.5988 230.1547 -19.5770 0 0 0
507. 3 2 14.1245 230.1547 -17.0440 0 0 0
508. 3 2 20.6501 230.1547 -14.5111 0 0 0
509. 3 2 27.1758 230.1547 -11.9782 0 0 0
510. 3 2 33.7014 230.1547 -9.4452 0 0 0
511. 3 2 -21.0368 230.1547 -23.1831 0 0 0
512. 3 2 -14.5111 230.1547 -20.6501 0 0 0
513. 3 2 -7.9855 230.1547 -18.1172 0 0 0
514. 3 2 -1.4598 230.1547 -15.5843 0 0 0
515. 3 2 5.0659 230.1547 -13.0513 0 0 0
516. 3 2 11.5915 230.1547 -10.5184 0 0 0
517. 3 2 18.1172 230.1547 -7.9855 0 0 0
518. 3 2 24.6428 230.1547 -5.4525 0 0 0
519. 3 2 31.1685 230.1547 -2.9196 0 0 0
520. 3 2 -23.5697 230.1547 -16.6574 0 0 0

.
.
.
.
.
.
.
.

Velocities

1 0 0 0
2 0 0 0
3 0 0 0
4 0 0 0
5 0 0 0
6 0 0 0
7 0 0 0
8 0 0 0
9 0 0 0
10 0 0 0

11 0 0 0
12 0 0 0
13 0 0 0
14 0 0 0
15 0 0 0
16 0 0 0
17 0 0 0
18 0 0 0
19 0 0 0
20 0 0 0
.
.
.
.
.
.
.
.

Bonds

1 1 1 2
2 1 2 3
3 1 3 4
4 1 4 5
5 1 5 6
6 1 6 7
7 1 7 8
8 1 8 9
9 1 9 10
10 1 10 11
11 1 11 12
12 1 12 13
13 1 13 14
14 1 14 15
15 1 15 16
16 1 16 17
17 1 17 18
18 1 18 19
19 1 19 20
20 1 20 21
.
.
.
.
.
.

.
.

Angles

1 1 1 2 3
2 1 2 3 4
3 1 3 4 5
4 1 4 5 6
5 1 5 6 7
6 1 6 7 8
7 1 7 8 9
8 1 8 9 10
9 1 9 10 11
10 1 10 11 12
11 1 11 12 13
12 1 12 13 14
13 1 13 14 15
14 1 14 15 16
15 1 15 16 17
16 1 16 17 18
17 1 17 18 19
18 1 18 19 20
19 1 19 20 21
20 1 20 21 22

.
.
.
.
.
.
.
.

Appendix B

Lennard-Jones units

In Appendix A we reported an example of LAMMPS script where we chose *units lj*. This means that in our simulations we work with *Lennard-Jones units* which employ the mass, ϵ and σ of a system in order to use dimensionless physical quantities. Labeling quantities expressed in *lj units* with an asterisk, the conversion between these reduced values and the real physical values is the following:

- distance: $x^* = \frac{x}{\sigma}$;
- energy: $E^* = \frac{E}{\epsilon}$;
- force: $F^* = F\frac{\sigma}{\epsilon}$;
- mass: m.

σ and ϵ are the values that appear in the Lennard-Jones potential 4.1 , so they depend on the system which is the object of the simulation. In our case σ is the size of a bead composing one of the two strands, so it corresponds to the diameter of a single double-helix DNA. Considering a DNA molecule under normal physiological conditions, its diameter is approximately 2.5 nm, so we decide to set $\sigma = 2.5$ nm.
ϵ is an energy and it can be expressed as $\epsilon = k_bT$ where k_b is the Boltzmann constant and T is the temperature of the system. By assuming that chains are immersed in a buffer at room temperature (T=300 K) we have $\epsilon = 4.14 \cdot 10^{-21}$ J.
m is the mass of what we are simulating: in our case, as reference mass, we choose the one of a bead belonging to a chain, so in the *Input File* every bead of this kind has $m = 1$.
The Lennard-Jones time unit is indicated as τ. To convert τ to nanoseconds we use a typical time of the system, i.e. the time employed by a bead to cover a diffusion length of σ. Therefore one has:

$$\sigma^2 = 2D\tau$$

where D is the diffusion constant given by the Einstein's relation: $D = \frac{K_bT}{f\eta}$.

In the denominator η is the viscosity of the fluid where the chains are immersed in, while f provides a geometrical term which for a sphere $\frac{\sigma}{2}$ in radius is $f = 3\pi\sigma$. Finally we have:

$$\tau = \frac{3\pi}{2}\frac{\sigma^3\eta}{K_bT}$$

By using the room temperature $T = 300K$ and the corresponding water viscosity $\eta = 1\,cP$, the relation between τ and nanoseconds is the following:

$$\tau = 17.8\,ns.$$

Appendix C

DNA topology

In the cellular environment, DNA is usually topologically constrained [22, 23] and the result is the formation of supercoiled molecules.
Supercoiled DNA was first studied for circular DNA chains, but this theory can also be extended to the molecules whose ends aren't free to rotate: therefore magnetic tweezers simulate the formation of supercoils in linear DNAs, providing an experimental method for changing the DNA topology. The changes introduced by magnetic tweezers can be summarized by three quantities: linking number, writhe and twist, that we now analyze.
Considering a double-helix DNA, one observes that the rotation of the paramagnetic bead induces a strand to swivel about the other: the number of intertwining is called *linking number*, Lk, and for closed curves its value is always an integer. In this last case the procedure to calculate the linking number is the following: one chooses a travel direction along both the closed curves and projects them into a plane counting the number of crossings between the two two-dimensional strands. At each crossing is given a value +1 if it's a right-handed crossing and -1 if it's left-handed (see Fig. C.1). Therefore link is given by the following equation:

$$Lk = \frac{1}{2}\sum_i w_i \tag{C.1}$$

where w_i is the contribution of the i-th crossing (+1 or -1).
The linking number doesn't depend on the direction of view, but it changes if one of the two travel directions is inverted.

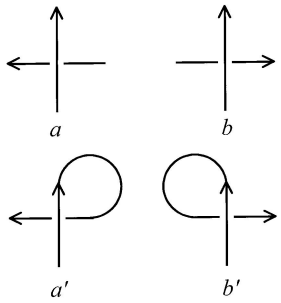

Figure C.1: Calculation of link. Panel **a** shows a right-handed crossing, that is a crossing which can be completed with a right-handed helix turn (panel **a'**). Panel **b** represents a left-handed crossing completed with a left-handed helix turn such as in panel **b'**. Figure from Klenin and Langowski [24].

So Lk is an invariant for closed curves and it can be seen as the sum of two quantities, writhe Wr and twist Tw:

$$Lk = Wr + Tw \tag{C.2}$$

Twist crossings are due to the rotations of a strand around the other, while the origin of the writhing number are the self-crossings of DNA axis (see Fig. C.2). Wr and Tw change depending on the direction of view, but their sum remains the same: for this reason, the writhe and the twist reported in the above equation are obtained averaging over all possible view directions.

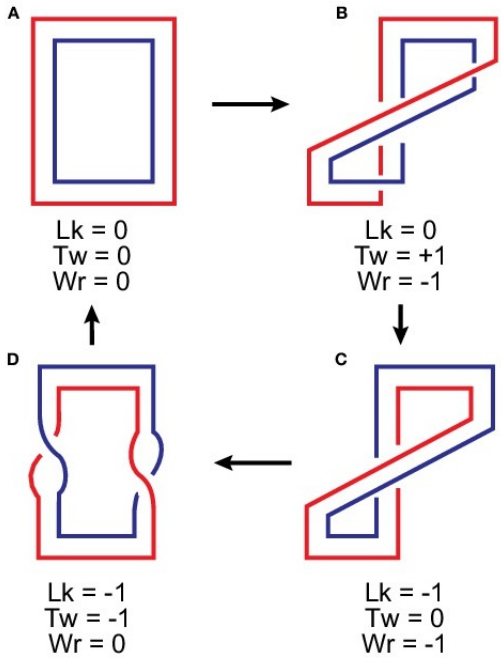

Figure C.2: Relation between link, writhe and twist. Here the circular DNA molecule is represented as a ribbon, whose edges are the sugar-phosphate backbones. Figure from Sarkar and Rybenkov [11].

The linking number between two curves C_1 and C_2 and the writhing number of a curve C can be found also through Gauss double integrals:

$$Lk = \frac{1}{4\pi} \int_{C_1} \int_{C_2} \frac{(d\vec{r}_2 \times d\vec{r}_1)\vec{r}_{12}}{r_{12}^3}$$

$$Wr = \frac{1}{4\pi} \int_{C} \int_{C} \frac{(d\vec{r}_2 \times d\vec{r}_1)\vec{r}_{12}}{r_{12}^3}$$

where $\vec{r}_1$ and $\vec{r}_2$ are two points of C_1 and C_2 or two different points of the same curve C, $\vec{r}_{12} = \vec{r}_2 - \vec{r}_1$ and $r_{12} =\mid \vec{r}_{12} \mid$. Finally twist is simply given by the difference between Lk and Wr.

In braiding we work with catenation Ca between two open strands. We define catenation as the linking number between the two chains looking along the direction orthogonal to the plane of the braid: Ca assumes both positive and negative values (according to the rules described for Lk) and it is an half-integer number. Four examples are reported in Fig. C.3 .
Considering our setup, one understands that catenation corresponds to half of the number of turns of the upper wall: by observing the system along the y-axis (see Fig. 4.1), a clockwise movement of the wall induces a positive Ca, while an anti-clockwise rotation introduces a negative one.

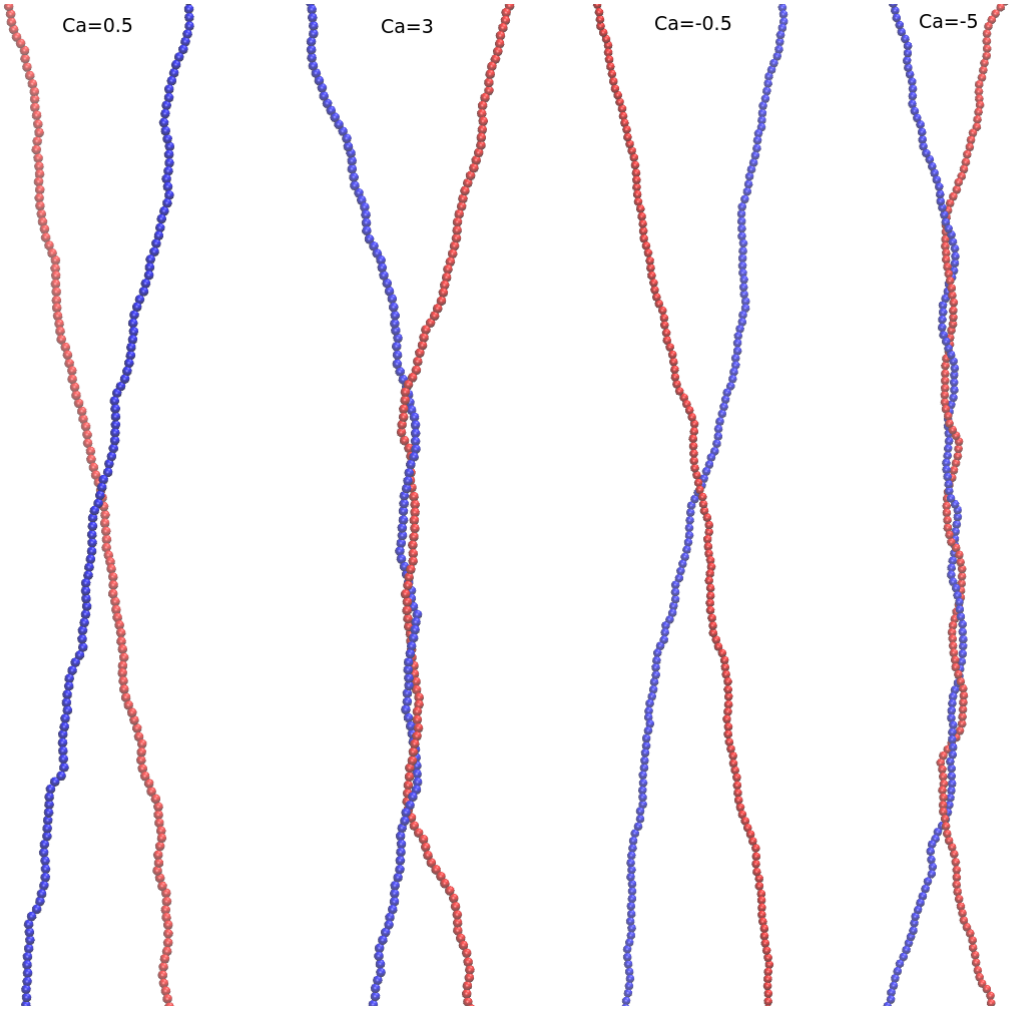

Figure C.3: Examples of strands with different catenation values. We choose a travel direction opposite to the y-axis, which is oriented as in Fig. 4.1 .

Bibliography

[1] J. Zlatanova and S.H. Leuba. *Magnetic tweezers: a sensitive tool to study DNA and chromatin at the single-molecule level.* Biochem. Cell Biol. **81**, 151 (2003).

[2] T.R. Strick, J.F. Allemand, D. Bensimon and V. Croquette. *Behavior of Supercoiled DNA.* Biophys. J. **74**, 2016 (1998).

[3] J.F. Marko and E.D. Siggia. *Statistical mechanics of supercoiled DNA.* Phys. Rev. E **52**, 2912 (1995).

[4] K.V. Klenin, A.V. Vologodskii, V.V. Anmshelevich, A.M. Dykhne and M.D. Frank-Kamenetskii. *Computer simulation of DNA supercoiling.* J. Mol. Biol. **217**, 413 (1991).

[5] B. Maier, D. Bensimon, V. Croquette. *Replication by a single DNA polymerase of a stretched single-stranded DNA.* Proc. Natl. Acad. Sci. U.S.A. **97**, 12002 (2000).

[6] G. Charvin, A. Vologodskii, D. Bensimon and V. Croquette. *Braiding DNA: Experiments, Simulations and Models.* Biophys. J. **88**, 4124 (2005).

[7] S. Brahmachari, K.H. Gunn, R.D. Giuntoli, A. Mondragon and J.F. Marko. *Nucleation of Multiple Buckled Structures in Intertwined DNA Double Helics.* Phys. Rev. Lett. **119**, 188103 (2017).

[8] A. Ashkin, J.M. Dziedzic, J.E. Bjorkholm and S. Chu. *Observation of a single-beam gradient force optical trap for dielectric particles.* Opt. Lett. **11**, 288 (1986).

[9] A. Ashkin and J.M Dziedzic. *Optical Trapping and Manipulation of Viruses and Bacteria.* Science **235**, 1517 (1987).

[10] T.R. Strick, J.F. Allemand, D. Bensimon, A. Bensimon and V. Croquette. *The elasticity of a single supercoiled DNA molecule.* Science **271**, 1835 (1996).

[11] R. Sarkar and V.V. Rybenkov. *A Guide to Magnetic Tweezers and Their Applications.* Front. Phys., **4** (2016).

[12] R. Janissen, B.A. Berghuis, D. Dulin, M. Wink, T.v. Laar and N.H. Dekker. *Invincible DNA tethers: covalent DNA anchoring for enhanced temporal and force stability on magnetic tweezers experiments.* Nucl. Ac. Res. **42** (2014).

[13] T.R. Strick, V. Croquette and D. Bensimon. *Homologous pairing in stretched supercoiled DNA.* Proc. Natl. Acad. Sci. U.S.A. **95**, 10579 (1998).

[14] J.F. Allemand, D. Bensimon, R. Lavery and V. Croquette. *Stretched and overwound DNA forms a Pauling-like structure with exposed bases.* Proc. Natl. Acad. Sci. U.S.A. **95**, 14152 (1998).

[15] J.C. Wang. *Cellular roles of DNA topoisomerases: a molecular perspective.* Nat. Rev. Mol. Cell Biol. **3**, 430 (2002).

[16] J.E. Deweese, M.A. Osheroff and N. Osheroff. *DNA Topology and Topoisomerases: teaching a "knotty" subject.* Bioch. and Molec. Biol. Edu., **37**, 2 (2009).

[17] C.D. Hardy, N.J. Crisona, M.D. Stone, N.R. Cozzarelli. *Disentangling DNA during replication: a tale of two strands.* Phil. Trans. R. Soc. Lond. B, **359**, 39 (2004).

[18] J. Marko. *Supercoiled and braided DNA under tension.* Phys. Rev. E **55**, 1758 (1997).

[19] J. Marko. *Coupling of intramolecular and intermolecular linkage complexity of two DNAs.* Phys. Rev. E **59**, 900 (1999).

[20] S. Brahmachari and J. Marko. *Torque and buckling in stretched intertwined double-helix DNAs.* Phys. Rev. E **95**, 052401 (2017).

[21] G. Charvin, V. Croquette and D. Bensimon. *Single molecule study of DNA unlinking by eukaryotic and prokaryotic type II topoisomerases.* Proc. Natl. Acad. U.S.A. **100**, 9820 (2003).

[22] A. Vologodskii. *DNA supercoiling helps to unlink sister duplexes after replication.* Bioessay, **32**, 9 (2010).

[23] A. Travers, G. Muskhelishvili. *DNA structure and function.* FEBS J., **282**, 2279 (2015).

[24] K. Klenin and J. Langowski. *Computation of Writhe in Modeling of Supercoiled DNA*. Biopolymers, **54**, 307 (2000).

[25] B.A. Krajina and A.J. Spakowitz. *Large-Scale Conformational Transitions in Supercoiled DNA revealed by Coarse-Grained Simulation.* Biophys. J., **111**, 1339 (2016).

[26] A. Ghatak, L. Mahadevan. *Solenoids and Plectonemes in Stretched and Twisted Elastomeric Filaments.* Phys. Rev. Lett., **95**, 057801 (2005).

[27] M.T.J. van Loenhout, M.V. de Grunt and C. Dekker. *Dynamics of DNA supercoils.* Science, **338**, 94 (2012).

[28] P.J. Hagerman. *Flexibility of DNA.* Ann. Rev. Biophys. Chem., **17**, 265 (1988).

[29] A.A. Travers. *The structural basis of DNA flexibility.* Phil. Trans. R. Soc. Lond. A, **362**, 1423 (2004).

[30] C.P. Goodrich and M.P. Brenner. *Using active colloids as machines to weave and braid on the micrometer scale.* Proc. Natl. Acad. Sci. U.S.A., **114**, 257 (2017).